Ultrasound and Photoacoustic Molecular Imaging

by

Alexander E. Forbrich

A thesis submitted in partial fulfillment of the requirements for the degree of

Doctor of Philosophy

In

Biomedical Engineering

Department of Electrical and Computer Engineering
University of Alberta

Abstract

Molecular imaging techniques are important for understanding fundamental biological processes and genetic functions in organisms. Non-invasive, high-resolution, deep imaging, as well as the ability to separate molecular species, are all critical to the success of a molecular imaging technique. Histology combined with optical imaging is often used as the gold standard; however, due to light scattering in tissues these techniques only provide high-resolution images in thin, transparent samples or superficially in tissues. Photoacoustic imaging combines the absorption-based contrast afforded by optical imaging techniques and the acoustic resolution afforded by the ultrasound detector. Since acoustic waves are scattered three orders of magnitude less than light in tissues, photoacoustic imaging allows high-resolution visualization in deep tissues. As complimentary imaging modalities, ultrasound and photoacoustic imaging can be combined to provide molecular information, as well as anatomical and structural information.

Although ultrasound and photoacoustic imaging have great potential for non-invasively profiling the molecular makeup of tissues *in vivo*, their utility for these applications is still in its infancy and requires refinement, as well as further investigation. The work presented in this dissertation approaches molecular imaging using ultrasound and photoacoustic imaging from several different directions to answer the question: “How much new molecular information can be extracted using combined ultrasound and photoacoustic imaging systems?”. This dissertation begins with an investigation of how ultrasound alone can help profile the molecular nature of tissues. The final chapters investigate how photoacoustic imaging, combined with ultrasound, can be used to non-invasively detect molecular species.

The concept of ultrasound inducing sonoporation and liberating biomarkers into the blood stream and surrounding media is explored. Using this technique, molecular profiles could be built

up from blood samples in organisms reducing the requirement of highly-invasive biopsies. We demonstrated, for the first time, that nucleic acid biomarkers could be released using this technique and that phase-changing ultrasound contrast agents, such as microbubbles, could be used to substantially increase the release of biomarkers into the surrounding media. To enable visualization of these phase-change events, novel image sequences were developed for high-speed differential ultrasound imaging. These techniques isolated the signals from microbubble destruction events and nanodroplet vaporization events from background signals. We believe that this will help assess the efficacy of biomarker liberation surrounding tissues of interest.

A novel photoacoustic screening technique is developed to evolve genetically-encoded reporter molecules optimized specifically for photoacoustic imaging. These new reporters were used in a number of protein constructs to increase the sensitivity of photoacoustic imaging. Additionally, proteins were developed to enable nonlinear photoacoustic imaging using the concept of Förster resonance energy transfer (FRET). With this screening technique, we were able to enhance the photoacoustic signal four-fold compared to the original gene and we were able to visualize, for the first time, the FRET effect using genetically-encodable proteins. Lifetime-weighted photoacoustic imaging, a novel nonlinear imaging technique, was investigated as another contrast mechanism for photoacoustic imaging. Using this technique, short-lifetime molecules, such as background signals from blood, could be nullified while the long-lifetime molecules could be highlighted. Finally, part of this work was conducted while developing ultrasound and photoacoustic imaging systems at FUJIFILM VisualSonics Inc. This work included implementing and advancing the molecular imaging capabilities of the commercial photoacoustic imaging system Vevo LAZR. Spectral demixing techniques, processing algorithms, and software developments were all done to enable new applications for photoacoustic molecular imaging. Imaging of lymphatic pumping is presented as an example of an application that became possible

with these enhancements. With photoacoustic imaging, we demonstrated multiple new contrast mechanisms and techniques to enable molecular photoacoustic imaging in new applications.

The work presented in this dissertation contributes to the field of molecular imaging using ultrasound and photoacoustic imaging and will help further the understanding of fundamental biological processes and genetic pathways.

Preface

Chapter 3-6 discusses the research into ultrasound-aided biomarker liberation and is primarily composed of the publications from (1) “Microbubble-enhanced ultrasound liberation of mRNA biomarkers in vitro” and (2) “Comparing efficiency of micro-RNA and mRNA biomarker liberation with microbubble-enhanced ultrasound exposure” both published in *Ultrasound in Medicine and Biology*. As lead author, I was responsible for: preparing and cultivating the cells, creating and characterizing the lipid-stabilized microbubbles, purifying and processing the media for biomarkers, and analyzing the results. This work led to several additional studies including an examination of the effect phase-change nanodroplets have on biomarker release published in *Ultrasound in Medicine and Biology* in the article “RNA biomarker release with ultrasound and phase-change nanodroplets”. As second author, I contributed by performing and planning some of the experiments and helping create and characterize the nanoparticles.

Chapter 7 describes a novel pulse-sequence that was developed for imaging phase-change events. This imaging scheme enabled, for the first time, the visualization of the phase transition from the liquid perfluorocarbon nanodroplets to gas microbubbles in real-time. This technique was also capable of imaging the destruction events of microbubbles under a high-pressure acoustic field. My primary contributions for this work were published in *IEEE International Ultrasonics Symposium* in the article “Realtime flash-difference ultrasound imaging of phase-change perfluorocarbon nanodroplet activation”. For this work, I was responsible for: creating the phantoms and perfluorocarbon nanodroplets, writing the MATLAB scripts to generate the appropriate pulse-sequences for a programmable ultrasound system, and processing the data in MATLAB to do the beamforming and reconstruct the phase-change events. This work also led to the article “Porphyrin nanodroplets: Sub-micrometer ultrasound and photoacoustic contrast imaging agents” published in *Small* for which I helped perform some of the photoacoustic imaging and helped examine the phase-change events using laser pulses.

Chapter 8 describes the screening techniques that I developed and used for the evolution of proteins that are optimized for photoacoustic imaging. This chapter also discusses a nonlinear imaging technique that can be used with these newly optimized proteins. This work was an interdisciplinary collaboration led by R. Zemp (Department of Electrical and Computer Engineering) and R. Campbell (Department of Chemistry) at the University of Alberta. Biological

and chemical preparation and analysis, as well as the initial primary absorption screening, was performed by Yan Li. This chapter presents the pioneering work on using directed evolution for optimizing genes for photoacoustic imaging and, for the first time, demonstrates photoacoustic imaging of the FRET effect with chromoproteins. This work has been presented at several conferences and published in *Scientific Reports* in the article "Engineering dark chromoprotein reporters for photoacoustic microscopy and FRET imaging". As equally-contributing first author, the photoacoustic system design and imaging, as well as the quantification of the generated signal, was my responsibility. To that end, unique C++ programs and MATLAB scripts had to be generated to capture and assess the data.

Chapter 9 explores another nonlinear imaging technique using a pump-probe experiment to provide unique contrast for photoacoustic imaging. This chapter presents the first reports to create lifetime-weighted photoacoustic images using a novel sequence of laser pulses and image the ground-state recovery of methylene blue. The publication "Lifetime-weighted photoacoustic imaging" in *Journal of Optics* will be presented in this chapter. As first author of this publication, I developed the imaging system, collected and processed all the data.

Chapter 10 presents the work that I spearheaded with FUJFILM VisualSonics Inc. For that work, I was in charge of much of the photoacoustic system development in terms of the software, the hardware, and some of the applications. On the software side, I was in charge of (1) developing algorithms for spectrally demixing components within an image, (2) developing the control software and algorithms to allow imaging using a rotating arm, (3) performing image characterization and (4) enhancing the reproduciblity of measurements. The chapter is devoted to discussing an application of this work for lymphatic pumping using the spectral demixing algorithms, the measurement techniques, and custom software to control a laser and enable fast-switching. The work has been accepted for publication in the *Journal of Biomedical Optics*.

In vivo experiments involving animals described in chapters 4, 5, and 8 in this dissertation followed the laboratory animal protocol approved by the University of Alberta Animal Committee. The animal experiments described in chapter 10 were conducted in accordance with the Animal Committee at FUJIFILM VisualSonics Inc.

Acknowledgements

A huge thank you to Dr. Roger Zemp for his support throughout my graduate work and his endless patience as I worked through the final years of study while working full time at FUJIFILM VisualSonics Inc. His vast knowledge spanning many disciplines and his ability to balance personal and academic life are truly awe-inspiring and inspirational. Thank you for your guidance throughout my research and encouraging me to continue my studies. It has been a great pleasure to work with you over the last few years and to grow as a scientist and researcher as your graduate student.

Furthermore, thank you to my supervisory committee members Dr. Mary Hitt and Dr. Robert Campbell. Your insights were truly helpful, allowed this research to proceed smoothly, and enabled the publication of several key journal articles. Thank you for being a part of my journey through my graduate studies.

I am sincerely thankful to all my colleagues that I have worked with at the University of Alberta. Special acknowledgements to Parsin Haji Reza, Yan Li, Robert Paproski, Peng Shao, and Wei Shi with whom I often worked closely on many different projects. The many scientific debates we had truly stimulated my interest in research and encouraged me to delve into the mysteries of biomarkers, ultrasound, and photoacoustic imaging. Thank you all for being amazing friends and colleagues.

Additionally, I appreciate the help and support from the Department of Electrical and Computer Engineering at the University of Alberta, especially Pinder Bains, Herbert Dexel, Kathleen Forbes, and Rick McGregor. I am also grateful to Dr. Carol Cass, Dr. Ron Moore, and members of their labs at the University of Alberta who helped me learn wet lab techniques for my research.

To FUJIFILM VisualSonics Inc., thank you for taking me into your family and teaching me how to apply my graduate research to commercial products. Special thanks to Andrew Heinmiller, Desmond Hirson, and Stanley Poon who have encouraged me to continue my research. This opportunity has been truly spectacular.

Finally, I am profoundly indebted to my entire family who have supported me throughout my studies and encouraged me through the difficult times. Your love and support have driven me to do my very best in everything that I do. Thank you!

Funding for this research has been provided by a number of generous sources including the Natural Sciences and Engineering Research Council of Canada (NSERC, Alexander Graham Bell CGS D), Alberta Innovates Technology Futures, Queen Elizabeth II, as well as funding through Dr. Roger Zemp and Dr. Robert Campbell including: Canadian Cancer Society Innovation Grant (702032), NSERC (RGPIN 288338-2010, RGPIN 355544-2008, CHRPJ 462510, STPGP 396444), Canadian Institutes of Health Research (MOP-123514, CPG 134739), Terry Fox Foundation (TFF 019237, TFF 019240), and the Canadian Cancer Society (CCS 2011-700718), the Alberta Cancer Research Institute (ACB 23728), the Canada Foundation for Innovation, Leaders Opportunity Fund (18472), Alberta Advanced Education and Technology, Small Equipment Grants Program (URSI09007SEG), and Prostate Cancer Canada (MVBRDG D2013-40, D2015-04).

Table of Contents

List of Figures

List of Tables

List of Symbols

α_{th}	thermal diffusivity
β	thermal coefficient of the volume expansion
ε	extinction coefficient
Γ	Grüneisen parameter
κ^2	relative orientation between the transition dipoles of the donor and acceptor
λ	wavelength
μ_a	absorption coefficient
Φ	fluence
Φ_{FRET}	overall efficiency of FRET
ω	angular frequency
σ_A	absorption cross-section of the acceptor
$\sigma_{A_{pump}}$	absorption cross-section at the wavelength of the pump
τ_D	fluorescent lifetime of the donor
τ_{GSR}	ground-state recovery lifetime
τ_L	excited-state lifetime
τ_s	stress relaxation time
τ_{th}	thermal relaxation time
ν_{pump}	frequency of the pump pulse
ν_s	speed of sound
c	speed of light
C	concentration
C_p	specific heat capacity
d_c	characteristic dimension
f_D	normalized emission spectrum of the donor
h	Planck's constant
I	intensity
I_{sat}	saturation intensity
k_T	rate of conversion for FRET
n	refractive index
N_0	number of molecules

p_0	initial photoacoustic pressure
Q_D	fluorescent quantum yield of the donor
r	distance
R_0	Förster radius
t	time

List of Abbreviations

µB	microbubble
aeCP597	chromoprotein from *Actinia equine*
ANOVA	analysis of variance
ANSI	American National Standards Institute
asCP	chromoprotein from *Anemonia sulcate*
A-Scan	one-dimensional ultrasound scan (depth)
B-Scan	two-dimensional ultrasound scan
BMF	blood-mimicking fluid
C-Scan	three-dimensional ultrasound scan
CA-125	cancer antigen 125
cDNA	complementary DNA
CEA	carcinoembryonic antigen
cjBlue	chromoprotein from *Cindopus japonicas*
CT	computed tomography
DAQ	data acquisition card
DIO	digital input-output card
DNA	deoxyribonucleic acid
DOT	diffuse optical tomography
DsRed	fluorescent protein from *Discosoma* sp.
E. coli	*Escherichia coli*
ELISA	enzyme-linked immunosorbent assays
EPR	enhanced permeability and retention effect
ESL	excited-state lifetime
EYFP	enhanced yellow fluorescent protein
FBS	fetal bovine serum
FDA	Food and Drug Administration
FRET	Förster resonance energy transfer
GFP	green fluorescent protein
GSR	ground-state recovery
HER2	human epidermal growth factor receptor 2

HIFU	high-intensity focused ultrasound
HSD	honest significant difference
ICG	indocyanine green
iRFP	infrared fluorescent proteins
LASER	light amplification by stimulated emitted radiation
M	mirror
M-mode	one-dimensional imaging over time
MB	methylene blue
MC	motor controller
MI	mechanical index
miR-21	22-nucleotide miRNA molecule
miRNA	small (< 25 nucleotide) non-encoding RNA molecules
MOPS	buffer solution, 3-(N-morpholino)propanesulfonic acid
MRI	magnetic resonance imaging
mRNA	messenger RNA
nD	nanodroplets
OL	objective lens
OPO	optical parametric oscillator
PA	photoacoustic
PBS	phosphate-buffered saline
PCR	polymerase chain reaction
PD	photodiode
PEG	polyethylene glycol
PET	positron emission tomography
pO_2	partial pressure of oxygen
PR	pulsar-receiver
PSA	prostate-specific antigen
qPCR	quantitative PCR
QY	quantum yield
REACh	resonance energy-accepting chromoprotein
RPMI	Roswell Park Memorial Institute medium
RNA	ribonucleic acid

SPECT	single-photon emission computed tomography
SNR	signal-to-noise ratio
Tris	buffer solution, tris(hydroxymethyl)aminomethane
TX	transducer
UCA	ultrasound contrast agent
US	ultrasound
UST	ultrasound transducer
VEGFR2	vascular endothelial growth factor receptor 2
YFP	yellow fluorescent protein

Chapter 1 Introduction

1.1 Molecular Imaging

Our ever-increasing scientific understanding of biological processes and genetic functions has become an essential part of research in many disciplines and has influenced medicine greatly. With this knowledge, scientists have been able to find many techniques to aid in the diagnosis, prognosis, and treatment of various diseases, including cancer. Many of these techniques rely on detecting anatomical abnormalities in tissues; however, this approach requires high-resolution imaging systems and often small anomalies are still difficult to detect. Since the characteristics of each patient and disease are unique, the detection of physical abnormality is not necessarily enough to suggest the best course of treatment. Hence, these techniques do not lend themselves well to personalized medicine where a treatment regiment is tailored to the patient and the unique characteristics of their illness. Rather than examining the gross anatomical nature of tissues and diseases, it would be preferable to directly, or indirectly, visualize and quantify their molecular 'fingerprint' and classify their precise phenotype. Molecular imaging techniques are highly desirable for personalized medicine as they enable the visualization and classification of biochemical events and disease characteristics at the cellular or molecule level within living cells, tissues, and organisms.

1.1.1 What is Molecular Imaging?

Molecular imaging techniques attempt to examine the biological processes at the molecular or cellular level and understand the biochemistry in living subjects. These imaging techniques can examine many unique features to gain insights into the genetic structure of tissues and diseases, as well as allowing their constituent components to be characterized and quantified. These biological features or biomarkers can be found in many forms, including membrane-bound surface receptors, that aid in diagnostic and prognostic assessment for patients [1–4]. For example, molecular imaging can assess the concentration of estrogen receptor, progesterone receptor, and human epidermal growth factor receptors 2 (HER2) present on the tumor in breast cancer patients. The relative concentration of these receptors can impact the prognosis of the patient dramatically [5, 6]. Often however, to gain access to these biomarkers, invasive

procedures such as solid biopsies are necessary. Although solid biopsies are associated with risks and can cause undue stress on the patient, they are considered the gold standard for many aspects of diagnostics, prognostics, and therapeutic planning for many diseases.

Another technique to access the biomarkers within a living subject is to perform liquid biopsies. Liquid biopsies, such as blood or urine tests, can contain a multitude of biomarkers. Prostate-specific antigen (PSA), found in liquid biopsies, have been widely used to diagnose prostate cancers [4, 7]. PSA, however, is not specific to aggressive tumors and consequently, benign prostate cancers are often over-diagnosed [8]. Circulating tumor cells have also been found in some blood samples from patients with metastatic cancer but low concentrations typically prevent reliable diagnosis and prognosis for most diseases [9]. Low concentration, no baseline, and the inability to determine the origin of the biomarkers found in liquid biopsies have severely limited its utility in preclinical and clinical research.

Rather than performing a biopsy, non-invasive (or minimally-invasive) molecular imaging techniques have been developed to visualize some of the biomarkers in tissues and diseases either directly or indirectly. Molecular imaging has been investigated with many imaging modalities including magnetic resonance imaging, x-ray computed tomography, positron emission tomography, single photon emission computed tomography, ultrasound imaging, optical imaging, and photoacoustic imaging [10]. For example, assessing the metabolic status of tissues is possible by visualizing radio-labeled glucose uptake in cells using positron emission tomography [11] or by visualizing the oxygen concentration in blood using blood-oxygen level dependent magnetic resonance imaging [12, 13]. Since most biomarkers are difficult to detect, molecular imaging techniques are often paired with exogenous contrast agents that can bind or react to specific biomarkers and provide additional contrast for the imaging modality. For instance, VEGFR2-targeted microbubbles have been used as ultrasound contrast agents that can attach to newly-formed, angiogenic blood vessels, often found surrounding tumors [14]. Often multiple modalities are used to investigate biological processes and pathways as each imaging modality and their associated contrast agents have advantages and disadvantages for molecular imaging in the research and clinical environments and each can provide complementary information [10].

1.1.2 Optical Molecular Imaging

Of the many imaging modalities utilized for molecular imaging applications, optical imaging techniques are the most prevalent. Optical imaging provides high-resolution imaging of biomarkers through either tissue staining or genetically-encoded proteins [15]. Histological staining is often applied to tissue samples taken from solid biopsies to highlight tissue structure or biomarkers of interest. Optical imaging of genetically-encoded proteins has revolutionized our understanding of biological processes and pathways. By tagging genes of interest with sequences encoding proteins such as the green fluorescent protein (GFP), scientists are able to visualize the expression of genes [16, 17]. Furthermore, by using multiple, spectrally distinct types of fluorescent proteins, they can examine the interaction of several proteins simultaneously, *in vivo* [16, 17]. Despite the power of optical imaging techniques, intense scattering of light in tissues limits high-resolution imaging to only a few hundred micrometers or to nearly transparent organisms. Several optical imaging techniques, such as diffuse optical tomography, can allow for deep imaging, but have low spatial resolution of millimeters to centimeters [18]. Therefore, high-resolution deep molecular imaging techniques are imperative to further enhance our understanding of biochemistry and biological processes.

1.1.3 Ultrasound Molecular Imaging

As acoustic pressure waves scatter three orders of magnitude less than light in tissues [19], ultrasound imaging is a potential molecular imaging tool that is capable of real-time, relatively high-resolution imaging in deep tissue. Although not typically thought of as a molecular imaging technique, contrast micro-ultrasound can be used to probe several biomarkers deep in tissue. With over 3 million clinical injections in over 50 countries [20] and since microbubbles can give strong ultrasound contrast with single-bubble sensitivity [21], targeted microbubbles have been proposed as molecular imaging contrast agents for ultrasound imaging [14]. Furthermore, as high-intensity ultrasound can destroy microbubbles, they have been investigated for assisting the localized delivery of therapeutic drugs [22]. The combination of targeted microbubbles and drug delivery gives ultrasound great potential as a diagnostic and therapeutic tool for scientists and clinicians.

1.1.4 Photoacoustic Molecular Imaging

Photoacoustic imaging is an emerging molecular imaging modality that can achieve ultrasound resolution while providing optical absorption-based contrast. Discovered in the late 1800s by

Alexander Graham Bell [23], the photoacoustic effect involves the conversion of light to heat and the subsequent thermo-elastic expansion leads to the generation of acoustic pressure waves. As a complementary imaging modality to ultrasound requiring similar equipment, photoacoustic imaging can easily be integrated into ultrasound systems and co-registered as a single image with anatomical information afforded by the ultrasound while optically-absorbing structures are detected by the photoacoustic signal. Since the lateral and axial resolution is determined by the ultrasound detector, relatively high-resolution images can be generated in deep tissues. As hemoglobin in blood strongly absorbs light, photoacoustic imaging is often used to visualize vascular structures without the aid of exogenous agents. Moreover, when bound to oxygen, the absorption spectrum of hemoglobin changes allowing for multiwavelength imaging and spectral demixing to estimate the concentrations of oxygenated and deoxygenated hemoglobin *in vivo* [24, 25]. Hence, local oxygen saturation measurements can be made non-invasively and label-free. Exogenous contrast agents and genetically-encodable optically-absorbing proteins have also been investigated as contrast agents for photoacoustic imaging to extend its molecular imaging capabilities [24, 26, 27].

1.2 Problem Statement

Although dual-modality ultrasound and photoacoustic imaging systems have great potential as molecular imaging tools, their introduction into many biological and clinical applications has been slow, in part due to the limited capabilities of genetic profiling available with these techniques and the limited selection of contrast mechanisms in comparison to optical imaging techniques. Moreover, as a nascent imaging modality, the capabilities of photoacoustics as a molecular imaging tool have not been fully investigated. Finally, few commercial products have been developed using photoacoustic imaging and turnkey approaches to collect highly-reproducible data are only starting to emerge. All these factors have limited the introduction of these imaging technique as a general-purpose molecular imaging tool and must be overcome to have widespread acceptance of this dual-modality imaging platform.

Overall, our long-term vision is to pioneer novel multi-modality imaging strategies to enable the characterization and classification of diseases with minimally invasive techniques. In particular, we are interested in addressing the question:

> *How much new molecular information can be extracted using combined ultrasound and photoacoustic imaging systems?*

Since ultrasound and photoacoustic imaging can non-invasively image relatively deeply with high-resolution, we believe that these modalities will be essential to further our understanding of the biochemistry in cells and tissues and may lead to advancements in diagnostics, prognostics, and therapeutic treatments for many diseases. By gathering new molecular information and extending the imaging techniques with ultrasound and photoacoustic imaging systems, many new applications may be possible. To direct our investigation and address this question, we investigate two key related questions:

1. Since ultrasound has been known to enhance cellular permeability for drug and gene delivery, can a similar effect be used to release biomarkers from cells into body fluids for liquid biopsies?

2. Can we use exogenous contrast agents, dyes, or genetically-encoded reporters for multimodality molecular imaging with new contrast mechanisms?

By addressing these two questions, we believe that dual-modality ultrasound and photoacoustic imaging systems have the potential to help classify and characterize diseases and may lead to a better understanding of biological processes, pathways, and disease mechanisms.

1.3 Goals and Motivation

Since we want to pioneer novel multimodality imaging strategies, it is imperative to be able to non-invasively image endogenous and exogenous reporter molecules deep within tissues to visualize gene expression and help assess their function *in vivo*. Although many imaging modalities could be investigated as tools for molecular imaging and biomarker characterization, ultrasound and photoacoustic imaging were used as they are relatively inexpensive, safe, fast, and have good spatial resolution and imaging depth. This research focused on several related but distinct aspects of these imaging modalities to address the issues and key questions described above and enhance their capabilities for molecular imaging.

1. Ultrasound Liberation of Biomarkers: Ultrasound was used to liberate biomarkers from cells for potential diagnosis and classification of diseases with liquid biopsy strategies. This work builds on the work conducted by D'Souza *et al.* [28] who first showed that ultrasound can be used to liberate proteins from cancers cells. For the first time, we extended this technique to other type of nucleic acid biomarkers including messenger RNA and micro-RNA. Also for the first time, we demonstrated that ultrasound contrast

agents, such as lipid-stabilized microbubbles, can enhance this effect. This work has been published in Forbrich *et al.* "Microbubble-enhanced ultrasound liberation of mRNA biomarkers in vitro" [29] and Forbrich *et al.* "Comparing efficiency of micro-RNA and mRNA biomarker liberation with microbubble-enhanced ultrasound exposure" [30]. With our team, additional contributions have shown that phase-change nanodroplets have a similar effect in releasing biomarkers [31]. Moreover, many biomarkers were found to be encapsulated in extracellular vesicles [32]. This is highly promising as such vesicles are orders of magnitude more abundant than circulating tumor cells, which are important for prognosis, but difficult to isolate from blood samples due to their low concentration. My colleague R. Paproski has continued this investigation and has shown that large amounts of genetic information are available in such vesicles and has identified tumor-specific mutations indicative of aggressive phenotypes [32]. My contributions have pioneered these continuing studies.

2. Ultrasound Imaging of Phase-Change Events: The contrast agents used in the liberation of biomarkers also enhance the contrast in ultrasound imaging. An investigation into another form of ultrasonic contrast agents, known as phase-change nanodroplets was conducted. Phase-change nanodroplets are sub-micron particles that can be made to react to ultrasound or light and expand to become visible on ultrasound images. These nanodroplets can extravasate from leaky vasculature found around some types of tumors, offering passive targeting strategies for molecular imaging of cancer [33, 34]. While other approaches have been used to phase-change nanodroplets and image the resulting microbubble forms of these agents, few approaches have shown the potential for imaging the phase-change events. We introduce an ultrafast phase-change imaging scheme which has been published in Forbrich *et al.* "Realtime flash-difference ultrasound imaging of phase-change perfluorocarbon nanodroplet activation" [35]. Furthermore, this approach was also shown to enable imaging of microbubble destruction events, which are important for ultrasound-aided drug delivery dosimetry. Imaging microbubble destruction and nanodroplet vaporization events could also be impactful for the biomarker liberation studies where it may be helpful to map cavitation events and provide a means of dosimetry for this novel approach. The imaging scheme has been adopted by other groups for nanodroplet imaging [36]. Other groups have studied active targeting approaches with both microbubbles and nanodroplets [37, 38]. The proposed

ultrafast imaging scheme has potential for these targeted imaging applications as well. We have also extended the nanodroplet work to include multimodality imaging with ultrasound and photoacoustics by loading the shells of the nanodroplets with porphyrin lipids, which absorb light and can induce a phase-change event [39]. This may be important for visualizing the nanodroplets in the liquid form as, in this form, they are undetectable by ultrasound.

3. Directed Evolution and Photoacoustic Imaging of Proteins: Significant advances have been made using fluorescent proteins to understand genetic pathways *in vitro*; however, optical studies are limited by light scattering and can only be used superficially *in vivo*. Photoacoustic imaging has significant potential for multiplexed imaging of gene expression in deep tissues as it is capable of imaging to significant depths with optical contrast and has been shown to be useful for studying or localizing various diseases. Many endogenous and exogenous contrasts agents have been investigated with promising results; however, photoacoustic imaging of genetically-encoded proteins has been met with limited success due to inefficient photothermal efficiency and few spectrally distinct photoacoustic-compatible proteins. Part of this dissertation is dedicated to the investigation of fluorescent proteins and chromoproteins for photoacoustic imaging of gene expression. Specifically, proteins were evolved for optimal photoacoustic characteristics using a novel screening technique. This new paradigm may enable modification of fluorescent reporters to provide optimal contrast for photoacoustic imaging. This work was done in collaboration with Y. Li and Dr. Robert Campbell and has been published in Li *et al.* [40]. This work is being continued by other members of the team to optimize chromoproteins in the near-infrared window, potentially allowing for deeper imaging, and developing photo-switchable proteins, similar to Yao *et al.* [41] and Dortay *et al.* [42].

4. Lifetime-Weighted Photoacoustic Imaging: Much of the research in photoacoustic imaging involves imaging of static chromophores; however, additional contrast mechanisms are possible using similar lifetime-based techniques described in the optical imaging literature [16, 43, 44]. Part of this dissertation is dedicated to photoacoustic imaging of molecular transient absorption states to separate different molecular species based on the ground-state or excited state lifetime and monitor the molecular

environment. Previously, multiwavelength photoacoustic methods have been used to spectrally demix molecular species; however, this approach is prone to estimation bias due to unknown depth-dependent fluence. We introduce a novel lifetime-weighted photoacoustic imaging technique and, for the first time, demonstrate ground-state recovery of molecules. This work has been published in Forbrich *et al.* "Lifetime-weighted photoacoustic imaging" [45] and extends the existing work to porphyrin-based molecules and the ground-state recovery lifetime of molecules. This approach is currently most useful for imaging molecules with a long triplet-excited state lifetime such as methylene blue, porphyrins, and some photo-sensitizers for photodynamic therapy. Moreover, this technique could provide a powerful way for assessing dissolved oxygen, estimating pH, and providing dosimetry for photodynamic therapy. It could also be used for imaging porphyrin nanodroplets and their use for molecular imaging and biomarker release. This work in conjunction with the gene expression could also be used for studying photo-switchable chromoproteins (which often have long lifetimes) that change the absorption spectra with selected pump wavelengths [41, 42].

5. Photoacoustic Imaging of Lymphatic Pumping: Sometimes termed the "forgotten circulation" [46], lymphatic pumping is responsible for many critical biological functions in organisms including regulation of fluid homeostasis and immune cell trafficking [46, 47]. Despite its vital role, there are few suitable *in vivo* imaging techniques available to image the lymphatic system [47, 48]. Photoacoustic imaging, in combination with exogenous contrast agents, may offer the ability to image the vasculature with high-resolution deep in tissues. With the development of fast wavelength switching, spectral demixing algorithms, and high sensitivity equipment at FUJIFILM VisualSonics Inc., we have demonstrated, for the first time, photoacoustic imaging of lymphatic pumping in mouse models. This work is in accepted for publication in the *Journal of Biomedical Optics* (accepted August 15, 2017). Additionally, since methylene blue can stain lymph nodes and has a long lifetime, the aforementioned lifetime-weighted imaging technique may be useful to enhance the contrast between the lymphatic vessels and the background signals [49]. This may have profound impacts in understanding the lymphatic system and lymphatic diseases.

Each of these proposed molecular imaging techniques can build on our current understanding of biological processes and may be useful for researchers performing non-invasive molecular imaging of live specimens.

1.4 Vision

Each of these research directions focuses on different aspects of how to use ultrasound and photoacoustic imaging systems as a molecular imaging tool. With the techniques that are described within this dissertation, we believe that many new or previously inaccessible avenues of research may open up. Moreover, we believe that these imaging techniques will contribute to the following idealized vision of how preclinical or clinical research may be performed (Figure 1.1). In the clinic, we believe that when a suspicious lesion is identified (Figure 1.1A):

1. Prior to the imaging session, blood samples could be drawn as a diagnostic baseline for biomarkers found in liquid biopsies biomarker (Figure 1.1B).

2. The suspicious lesion could be located, imaged, and morphologically characterized with ultrasound imaging (Figure 1.1C). Photoacoustic imaging could be used to visualize the vascular nature and oxygenation of the lesion (Figure 1.1C).

3. Ultrasound and/or photoacoustic contrast agents could be injected for clinical studies or genetically-encoded for preclinical or translation research (Figure 1.1D). Ultrasound and/or photoacoustic molecular imaging can identify target tissues by passive or active accumulation of the agents (Figure 1.1E). Novel imaging schemes will enable the imaging of these agents with high sensitivity and low background noise.

4. Ultrasound could be applied to induce local sonoporation, increasing the permeability of cells within the tissue of interest and releasing biomarker contents or biomarker-filled micro-vesicles into the surround fluid (Figure 1.1F).

5. Finally, a post-ultrasound blood sample could be drawn and, using traditional protein and RNA analysis techniques such as ELISA or PCR kits, the biomarkers can be compared with the pre-ultrasound blood sample for diagnostic purposes (Figure 1.1G).

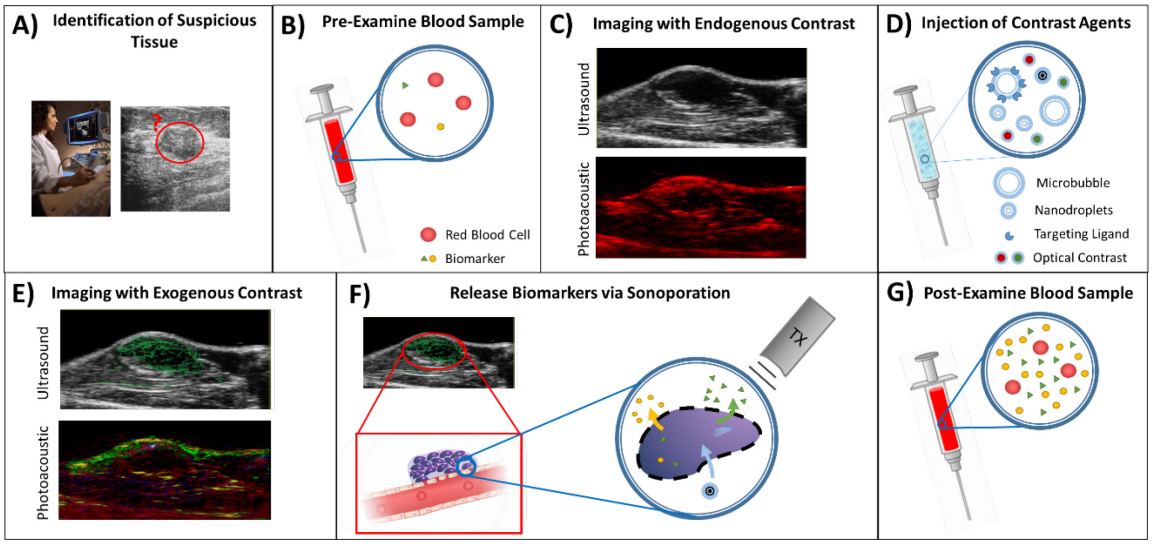

Figure 1.1 Vision for molecular imaging with ultrasound and photoacoustics. (A) A physician locates a suspicious lesion during an exam. (B) A blood sample is drawn providing baseline biomarker levels in the patient. (C) Ultrasound and/or photoacoustic is used to assess morphological characteristics, as well as vascularity within the tissue of interest. (D) Nontargeted or targeted contrast agents are injected into the patient to provide additional contrast and (E) probe the molecular characteristics of the tissue of interest. (F) Focused ultrasound is used to induce transient pores into the cell membrane of the cells and release biomarkers into the surround media and blood stream. Additionally, the focused ultrasound can be used to activate contrast agents for image contrast (or during therapeutic sessions for drug delivery). (G) After the imaging session, a blood sample is drawn and the levels of biomarkers can be analysed (using traditional biomarker analysis techniques) and can be compared to the biomarkers in the baseline blood sample to further characterize the tissue.

The combined molecular imaging and amplified biomarkers in the post-ultrasound blood sample may enable new opportunities for diagnostic and prognostic assessments and the ability to optimize treatment strategies for personalized medicine.

Follow up imaging sessions may incorporate contrast agents that are designed to transport therapeutic agents. Additionally, these contrast agents may be designed to be activated by high-intensity ultrasound and release the therapeutic drugs to nearby target tissues. The ultrasound-induced sonoporation would aid in delivery of the drug.

1.5 Overview and Structure of Dissertation

Chapter 2 provides a general discussion and background information for key topics in molecular imaging, ultrasound imaging, photoacoustic imaging, and contrast agents. Chapters 3-6 focuses

on the research into the liberation of biomarkers using ultrasound and ultrasound contrast agents. Chapter 7 discusses ultrasound and photoacoustic imaging of phase-change events. Chapter 8 presents the engineering aspects of the work done on optimized genetically-encoded proteins for photoacoustic imaging. Additional details regarding the biochemistry that was involved can be found in Y. Li's thesis [50]. Chapter 9 examines photoacoustic lifetime imaging and discusses the novel imaging sequence to create lifetime-weighted images. Lymphatic pumping is presented in Chapter 10. Finally, a summary and future directions is discussed in Chapter 11.

The contributions described in this dissertation can be divided into major contributions, for many of which I am first author and performed much of the research, and the minor contributions, for many of which other members and I have collaborated to extend the results of my initial publications.

1.5.1 Major Contributions (Molecular Imaging)

1. **A. Forbrich**, T. Harrison, R. Paproski, and R. Zemp, "Realtime flash-difference ultrasound imaging of phase-change perfluorocarbon nanodroplet activation," *IEEE International Ultrasonics Symposium*, pp. 687–690, 2012.

2. **A. Forbrich**, R. Paproski, M. Hitt, and R. Zemp, "Microbubble-enhanced ultrasound liberation of mRNA biomarkers in vitro," *Ultrasound in Medicine and Biology*, 39(6), pp. 1087–1093, 2013.

3. **A. Forbrich**, R. Paproski, M. Hitt, and R. Zemp, "Comparing efficiency of micro-RNA and mRNA biomarker liberation with microbubble-enhanced ultrasound exposure," *Ultrasound in Medicine and Biology*, 40(9), pp. 2207–2216, 2014.

4. Y. Li*, **A. Forbrich***, J. Wu, P. Shao, R. Campbell, and R. Zemp, "Engineering dark chromoprotein reporters for photoacoustic microscopy and FRET imaging," *Scientific Reports*, 6, p. 22129, 2016.

   * equal contributing authors

5. **A. Forbrich**, P. Shao, W. Shi, and R. Zemp, "Lifetime-weighted photoacoustic imaging," *Journal of Opt*ics, 18(12), p. 124001, 2016.

6. **A. Forbrich**, A. Heinmiller. “Photoacoustic imaging of lymphatic pumping *in vivo*.” (submitted to the *Journal of Biomedical Optics* on May 7, 2017)

1.5.2 Minor Contributions (Molecular Imaging)

1. R. Paproski, **A. Forbrich**, J. Ranasinghesagara, Y. Jiang, M. Hitt, and R. Zemp, “Photoacoustic imaging of gene expression using tyrosinase as a reporter gene,” *Proceedings SPIE 7899, Photons Plus Ultrasound: Imaging and Sensing 2011*, p. 78991H, 2011.

2. R. Paproski*, **A. Forbrich***, K. Wachowicz, M. Hitt, and R. Zemp, “Tyrosinase as a dual reporter gene for both photoacoustic and magnetic resonance imaging,” *Biomedical Optics Express*, 2(4), pp. 771-780, 2011.

   * equal contributing authors

3. **A. Forbrich**, R. Paproski, M. Hitt, and R. Zemp, “Microbubble-assisted blood biomarker amplification using ultrasound,” *2011 World Molecular Imaging Congress,* 2011. (Talk)

4. Y. Jiang, **A. Forbrich**, T. Harrison, and R. Zemp, “Blood oxygen flux estimation with a combined photoacoustic and high-frequency ultrasound microscopy system: a phantom study,” *Journal of Biomedical Optics*, 17(3), pp. 036012-1 - 036012-8, 2012.

5. **A. Forbrich**, Y. Li, W. Jiahui, R. Campbell, and R. Zemp, “Genetically-encoded chromoproteins for photoacoustic imaging,” *2013 World Molecular Imaging Congress*, 2013. (Poster)

6. P. Hajireza, **A. Forbrich**, and R. Zemp, “*In vivo* functional optical-resolution photoacoustic microscopy with stimulated Raman scattering fiber-laser source,” *Biomedical Optics Express*, 5(2), pp. 539-546, 2014.

7. R. Paproski, **A. Forbrich**, M. Hitt, and R. Zemp, “RNA biomarker release with ultrasound and phase-change nanodroplets,” *Ultrasound in Medicine and Biology*, 40(8), pp. 1847–1856, 2014.

8. R. Paproski, **A. Forbrich**, E. Huynh, J. Chen, J. Lewis, G. Zheng, and R. Zemp, “Porphyrin nanodroplets: Sub-micrometer ultrasound and photoacoustic contrast imaging agents,” *Small*, vol. 12, no. 3, pp. 371–380, 2016.

Chapter 2 Background Information

2.1 Molecular Imaging

This dissertation introduces novel approaches to biomedical molecular imaging using ultrasound and photoacoustics. Here we briefly introduce the concept of molecular imaging and frame how this research fits into the larger body of literature.

2.2 Imaging Modalities

There are many imaging modalities for studying the anatomical structure and physiological function of cells, tissues, and systems. Each modality has its own advantages and disadvantages in the research and clinical environments [10]. Large scale, whole-body imaging techniques can give a broad understanding of the interactions between tissues and the gross anatomical origins of biological processes. However, these techniques often lack the spatial resolution to resolve local cellular responses or they lack the functional imaging contrast mechanisms necessary for examining biological processes. These whole-body imaging techniques include x-ray computed tomography (CT), magnetic resonance imaging (MRI), positron emission tomography (PET), and single-photon emission computed tomography (SPECT). Smaller-scale, localized imaging techniques can provide highly detailed functional information at the cellular or tissue level; however, they often sacrifice field-of-view and imaging depth to achieve these high-resolution images. In both acoustic and optical imaging techniques, the spatial resolution decreases as the imaging depth increases. These local imaging techniques include ultrasound (US), optical imaging (such as diffuse optical tomography (DOT), confocal microscopy, etc.), and photoacoustic (PA) imaging (sometimes known as optoacoustic imaging).

Table 2.1 Comparison of various imaging modalities (modified from [18])

	Soft-tissue contrast	**Spatial resolution**	**Imaging depth**	**Imaging speed**	**Ionizing radiation**	**Cost**
X-ray CT	Poor	Excellent	Excellent	Fast	Yes	Low
PET and SPECT	Poor	Poor	Excellent	Slow	Yes	High
MRI	Excellent	Good	Excellent	Slow	No	High
US	Good	Good	Good	Fast	No	Low
Optical Imaging	Excellent	Mixed	Good	Fast	No	Low
PA	Excellent	Excellent and scalable	Good	Fast	No	Low

2.2.2 Whole-Body Imaging Modalities

2.2.2.1 X-Ray Computed Tomography

X-ray CT provides excellent whole-body, anatomical images with micron-scale resolution. However, poor soft-tissue contrast, ionizing radiation, and the absence of functional information prevents x-ray CT from examining many biological processes. To overcome the lack of functional contrast mechanisms, there has been much research into using injectable, targeted contrast agents such as iodinated nanoparticles [51] or gold nanoparticles [52]. Although more investigation should be conducted on using x-ray CT for molecular imaging, it has been combined with other imaging modalities, such as PET and SPECT, to provide a highly-detailed anatomical frame of reference while the complementary imaging modality provides molecular information.

2.2.2.2 Positron Emission Tomography and Single-Photon Emission Computed Tomography

PET and SPECT use radioactive isotopes as contrast agents to perform molecular imaging [53, 54]. As the isotopes decay, they emit radiation which can be detected and the origin of the emitted radiation can be determined. When the radioactive isotopes are tagged to biologically important molecules (such as glucose), these techniques provide a wealth of functional information including information about cellular uptake and cellular metabolism. For instance, the radio-isotope ^{18}F can be tagged to glucose to form ^{18}F-FDG (2-fluoro-2-deoxy-d-glucose) which can be used to detect metabolically active tissues, such as cancer [55, 56]. PET and SPECT, however, are currently limited in to millimeter spatial resolution and give limited information about the anatomical nature of a sample or patient. Multimodality imaging systems have been developed to overcome the limited anatomical information by combining PET and SPECT into x-ray CT or MRI systems.

2.2.2.3 Magnetic Resonance Imaging

Another whole-body imaging modality that uses non-ionizing radiation is MRI. With its high versatility in pulse sequences, MRI has excellent soft-tissue contrast, reasonable spatial resolution at the sub-millimeter to millimeter scale, and allows imaging through a patient at any cross-sectional plane without altering the position of the patient. Furthermore, MRI can also provide excellent physiological and functional information such as oxygen saturation of hemoglobin [12, 57] and the flow velocity of blood [58, 59]. Targeted-MRI contrast agents which change the relaxivity of the tissue of interest, such as gadolinium-based or super-paramagnetic iron oxide

nanoparticles, have been developed to perform molecular imaging [10, 60, 61]. Although MRI is an excellent imaging modality, the high cost of installation, equipment, and maintenance makes it unrealistic for many studies. Furthermore, long image acquisition and sub-millimeter to millimeter spatial resolution limits its use for understanding many biological processes.

2.2.3 Local Imaging Modalities

2.2.3.1 Ultrasound

Based on the transmission and subsequent detection of reflected acoustic waves, ultrasound provides a real-time imaging platform that enables the investigation of the mechanical properties within tissues. Ultrasound imaging has scalable spatial resolution based on the frequency of the transducer with the caveat that imaging penetration decreases as frequency increases; hence, there is a trade-off between imaging depth and spatial resolution. Ultrasound has been used as a diagnostic tool by non-invasively detecting morphological anomalies and visualize blood flow [62]. It has also been used as a therapeutic tool where high-intensity focused ultrasound (HIFU) is used to ablate or thermally induce necrosis in tissues. This has been used for treatments of kidney stones [63] and tumors [64]. Additionally, MRI-guided HIFU techniques have been developed where MRI provides thermal guidance over the target tissue making tissue ablation more precise [64, 65]. For molecular imaging, ultrasound often requires targeted contrast agents such as lipid-stabilized microbubbles to differentiate regions of interest [21, 66]. Additionally, the interaction between acoustic waves, microbubble contrast agents, and cells can increase the permeability of the cell membranes. This potentially allows contrast agents or therapeutic molecules to enter the cell or allows biomarkers to exit the cell making them more easily detectable [28, 66, 67].

2.2.3.2 Optical Imaging

Optical imaging techniques allow for high-resolution detection of biomarkers through either tissue staining or genetically-encoded proteins. Due to the high scattering of light in tissues, high-resolution optical imaging is severely limited in imaging depth to only several hundred micrometers thick slices of tissue. Several optical imaging techniques, such as diffuse optical tomography (DOT), allow for high imaging depth but have low spatial resolution of millimeters to centimeters [18]. Fluorescent proteins have revolutionized optical imaging of biological samples and dramatically increased the capabilities of molecular imaging in optical imaging modalities. When tagged to genes of interest, fluorescent proteins are capable of tracking gene expression at a cellular or subcellular level and allow optically imaging to investigate biological pathways and

processes in real-time. Since the fluorescent signal can be influenced by many environmental factors including the polarity, the pH, the viscosity, the presence of other analytes (O_2, Ca^{2+}, Cl^-, etc.), and the concentration or aggregation of the fluorescent molecule, fluorescence imaging techniques, such as fluorescent lifetime imaging, can examine the molecular environment surrounding the fluorescent molecule [16, 17]. Despite the power of optical imaging techniques and fluorescence imaging, the shallow imaging depth greatly limits the number of compatible *in vivo* applications.

Bioluminescence imaging is another powerful optical imaging technique. Although low resolution, this technique enables imaging several centimeters into the tissue of live animals non-invasively and allows the longitudinal monitoring of diseases and some biological processes [68]. Luciferase is a class of oxidative enzymes that can produce bioluminescence – the most common being found in the firefly. Luciferase has been incorporated in bacteria, virus, cancer cells, and transgenic mice to track tumor cells, bacterial infection, gene expression, and treatment response [69–71].

2.2.3.3 Photoacoustic Imaging

Photoacoustic imaging is an emerging molecular imaging modality that combines the depth penetration advantage of ultrasound imaging with the absorption-based contrast mechanisms. Unlike optical imaging techniques that rely on two-way propagation of light to form the images, photoacoustic imaging relies on the one-way propagation of light, absorption of light and subsequent conversion of light to an acoustic pressure wave, and the one-way propagation of sound to a detector. Since acoustic propagation is orders of magnitude less susceptible to scattering in tissues, morphological structures can be differentiated with acoustic resolution and hence imaging depths can increase dramatically compared to traditional optical imaging techniques [18]. Since many molecules have a unique absorption spectrum, photoacoustic imaging is capable of distinguishing different molecules based on the signal generated at different wavelengths. Photoacoustic imaging has been used for molecular imaging by examining endogenous contrast agents (such as oxyhemoglobin, deoxyhemoglobin, melanin, or lipids) [72], targeting optically absorbing contrast agents to biomarkers of interest [49, 73], and by genetically-encoding optically-absorbing proteins into cells [74, 75].

2.2.4 Preclinical and Clinical Molecular Imaging

Many of the molecular imaging strategies discussed above are designed with clinical applications in mind. However, preclinical imaging in animal models is extremely important for a number of reasons. For example, preclinical imaging may help evaluate efficacy of therapeutic drugs in xenograft tumors. Furthermore, imaging gene expression networks *in vivo* may help our basic understanding of biological processes.

2.2.5 Biomarkers

Cells and tissues contain a wealth of information in the form of biomarkers that allow the classification and characterization of the cells and tissue. As the targets of many molecular imaging techniques, biomarkers provide information on the biological functions, gene pathways, and metabolic state of tissues and cells. Biomarkers have great potential for aiding in diagnostics and assessing prognostic outlooks; however, it is sometimes difficult to access these biomarkers and often requires invasive procedures such as solid biopsies.

2.2.5.1 Solid Biopsies

Histology is often the gold standard for assessing diseases. To obtain tissue samples, biopsies are often required. This typically involves highly invasive procedures such as large needle punctures or surgical procedures, which can be risky. Biopsies should not be done too often and are associated with risks of infection and may even increase metastatic potential [76, 77]. Biopsies also are unpleasant to patients and lead many to avoid interventions because they do not want the procedure done. Less invasive means of assessing tissue biomarker status is highly desirable. Molecular imaging offers the promise of minimally invasive biomarker profiling using the imaging modalities described above. An alternate paradigm for obtaining biomarkers is from blood or urine samples often referred to as liquid biopsies. This dissertation discusses both novel imaging strategies as well as image-guided approaches for enhancing liquid biopsies.

2.2.5.2 Liquid Biopsies

A potential holy grail of diagnostic and prognostic personalized medicine is the readout of disease biomarkers from blood or urine tests. Such simple strategies would have widespread applicability to screening whereas many molecular imaging approaches, such as PET or MRI, are too costly and throughput is too limited to be used as general-purpose screening methods. Some examples of biomarkers found in liquid biopsies that are presently used include carcinoembryonic antigen

(CEA) for colorectal cancer [78], CA-125 for ovarian cancer [79], and prostate-specific antigen (PSA) for prostate cancer [4, 8]; however, there are currently issues in the specificity of these biomarkers. For example, elevated PSA levels are not necessarily correlated to aggressive prostate cancer and consequently benign prostate cancers are over-diagnosed [4, 8]. Additionally, liquid biopsies cannot be used to indicate the origin of the biomarkers within the body. This makes locating anomalous or diseased tissues difficult without additional imaging techniques. Currently, there are worldwide efforts to search for biomarkers that improve specificity for multiple diseases.

Free-circulating DNA and RNA, including micro-RNA (miRNA), are promising candidates as biomarkers for diagnosing various diseases [80–84]; however, they are often found in low concentrations making detection difficult.

2.3 Ultrasound-Aided Biomarker Release

In 2009, D'Souza *et al.* demonstrated that ultrasound can be used to liberate the cytoplasmic protein biomarkers within cells with minimal cell death [28]. Not only could this technique enhance the concentration of the biomarkers in liquid biopsies, any change in the biomarker concentration could be attributed to the region exposed to ultrasound making the origin of the biomarkers known. Using only 6 minutes of 2 W/cm^2 (50% duty cycle), they were able to significantly increase the concentration of the protein CEA in the surrounding media. This has great potential in many areas of research as this can help overcome the low concentration issue with blood-borne biomarkers, as well as localize the biomarkers to specific tissues *in vivo*.

One explanation for the increase in biomarker concentration is that the cell membranes formed transient pores increasing the permeability and allowing the biomarkers to escape. This process is known as sonoporation. Sonoporation is an effect where the ultrasound pressure waves interact with cell membranes and increase the cell membrane permeability [85]. Sonoporation has been widely studied as a means to deliver various molecules into cells. For instance, sonoporation is being researched as a method to enhance gene transfection [86, 87], as well as delivering drugs to tissues [37, 88]. Sonoporation has been used to disrupt the blood-brain barrier and allow the transport of therapeutic drugs into the brain [88–90].

Chapters 3-6 of this dissertation build on the D'Souza contribution to demonstrate biomarker amplification of circulating RNA. This work also investigated the role that microbubble and nanodroplet ultrasound contrast agents play on the amplification of these biomarkers.

2.4 Microbubbles and Nanodroplet Ultrasound Contrast Agents

We investigate the use of microbubbles and nanodroplet ultrasound contrast agents for both biomarker liberation as well as multimodality imaging. Because these topics will be discussed throughout this dissertation, we will give a literature review of some key contributions.

2.4.1 Ultrasound Contrast Agents – Lipid-stabilized Microbubbles

With over a total of three million diagnostic injections in over 50 countries [20], ultrasound contrast agents have become commonplace in diagnostic medicine, enhancing contrast within the vasculature and aiding in diagnostics. Microbubbles have several unique properties that make them ideal ultrasound contrast agents. Microbubbles are gas-filled bubbles that are typically less than 5 μm allowing them to travel through the bloodstream. Since the gas has a high acoustic impedance compared to surrounding tissues, the microbubbles reflect the ultrasound energy which appears as an intense signal on an ultrasound image. Due to the strong reflection, it is possible to detect a single microbubble with ultrasound indicating a picogram sensitivity to these contrast agents [21]. Microbubbles also have nonlinear properties that allows imaging of higher order harmonics which can nullify background signals and enhance the contrast of the microbubbles. Typically, pulse inversion imaging schemes are used to image these nonlinear properties [91]. Although microbubbles have many advantages, the gas inside microbubbles diffuses out of the bubble making them unstable.

Lipid-stabilized microbubbles have been created to mitigate the diffusion of the gas. These microbubbles tend to use a low-solubility gas with high molecular weights and low diffusivity, such as perfluorocarbons, as well as a thick impermeable lipid membrane [37]. Lipid-stabilized microbubbles also have the advantage of being capable of surface modification allowing them to be targeted with antibodies to surface receptors on cells and PEGylated (a polyethylene glycol coating that can shield molecules or macrostructures from the immune cells) to improve longevity *in vivo* [14]. Moreover, the microbubbles can be designed to aid drug delivery or transport therapeutics to target tissue [37, 88, 92]. Several mechanisms for this have been explored including: (1) co-administration of therapeutics and microbubbles relying on the increased cell

permeability due to sonoporation, (2) attachment of drugs or drug-containing vesicles onto the shell of the microbubble, (3) the therapeutic may be directly incorporated into the microbubble's shell, and (4) the therapeutic may be contained within the microbubble [37]. Acoustic radiation forces can be used to direct microbubbles towards target areas [93] and high-intensity ultrasound can be used to destroy the microbubbles and release the therapeutic [37, 88]. Imaging of the destruction of microbubbles may be important for assessing the efficacy of drug delivery.

Much research has shown that ultrasound contrast agents, such as microbubbles, can enhance the effect of sonoporation [37, 88]. The exact mechanism of this enhancement is not fully understood; however, evidence suggests it may be caused by acoustic microstreaming, shock waves from the microbubble collapsing, and microjet cavitation due to microbubble collapse [94]. Images of cells that have been exposed to the microbubble-enhanced sonoporation show pores ranging in size from hundreds of nanometers to a micron in diameter [67, 85, 95]. This has had implications for drug delivery, gene transfection, and disruption of the blood brain barrier.

2.4.2 Phase-Change Nanodroplets

The relatively large size of microbubbles restricts them to the vascular network allowing imaging of perfusion [20]. For some applications, their large size is detrimental as it is difficult to get microbubbles near diseased tissues preventing targeting to those tissues or efficient delivery of therapeutics. The vasculature surrounding many tumors is 'leaky' potentially allowing molecules to passively accumulate around the tumor through the enhanced permeability and retention effect [33, 96, 97]. Hence, it is important to find methods to reduce the size of microbubbles.

Sheeran *et al.* developed phase-change nanodroplets by pressurizing lipid-based perfluorocarbon microbubbles reducing the microbubble size by up to seven-fold [34]. The pressure causes the perfluorocarbon to phase-change into a liquid. Due to high Laplacian forces on the nanodroplets, they are very stable at biologically relevant temperatures. Under intense ultrasound pressures, these nanodroplets can be phase-changed from the liquid nanodroplets to gaseous lipid-stabilized microbubbles. Unfortunately, these nanodroplets are not detectable by ultrasound until they are phase-changed and previously no imaging scheme had been proposed to visualize the phase-change events. A section of this dissertation is dedicated to discussing how to detect phase-change events of these nanodroplets.

2.4.3 Multimodality Contrast Agents for Ultrasound and Photoacoustic Imaging

Microbubbles have been made that are compatible with multiple imaging modalities including fluorescence and photoacoustic imaging [98–101]. For fluorescence and photoacoustic imaging, this has been accomplished by either constructing the lipid-shell with an optically-absorbing molecule, such as rhodamine for fluorescence [39] or porphyrins for photoacoustic [99, 100], or loading the microbubble with dyes [98]. In 2012, porphyrin-shell microbubbles were developed that provided good contrast in both ultrasound and photoacoustic imaging [99]. In 2014, Jeon *et al.* demonstrated a methylene blue-filled microbubble for contrast in both ultrasound and photoacoustic imaging [98]. With these new, multi-modality contrast agents it may be possible to distinguish co-administered contrast agents enabling higher throughput and providing better specificity.

Similarly, visualizing nanodroplets in the liquid form with photoacoustic imaging has been possible by creating the lipid-shell with porphyrins [39, 102] and loading the nanodroplets with optically-absorbing molecules such as indocyanine green [103]. Moreover, it has been shown that the absorption of light can provide another means to induce phase-change events in porphyrin-shelled nanodroplets. I contributed collaboratively to this project. Although these formations enable the visualization of nanodroplets, there is still a need to visualize the phase-change events. I developed an ultrafast imaging method for this purpose which will be described in this dissertation. This has implications for drug delivery where it is important to know how many contrast agents have phase-changed near the target tissue.

2.5 Photoacoustic Imaging

2.5.1 The Photoacoustic Effect

Although the photoacoustic effect, which photoacoustic imaging is based on, was first investigated by Alexander Graham Bell in 1880 [23], it was not until recently, with the advent of the laser, that this phenomenon gained wide-spread interest for application in preclinical and clinical imaging [18, 26, 104–106]. The photoacoustic effect involves the conversion of optical energy to acoustic energy. When molecules absorb electromagnetic radiation, such as light, there is a localized heating and rapid thermoelastic expansion subsequently producing broadband acoustic pressure waves that are detectable by ultrasound transducers [104] (Figure 2.1). Since the amplitude of the photoacoustic wave is directly related to the absorption of light (Eq. 1) and

the scattering of acoustic pressure waves are three orders of magnitude less than light in tissues [104], photoacoustic imaging is capable of imaging deep in tissues while maintaining high-resolution and optical contrast. Moreover, photoacoustic imaging can easily be interlaced and combined with ultrasound imaging techniques, such as Doppler imaging, to provide images with additional structural and functional details.

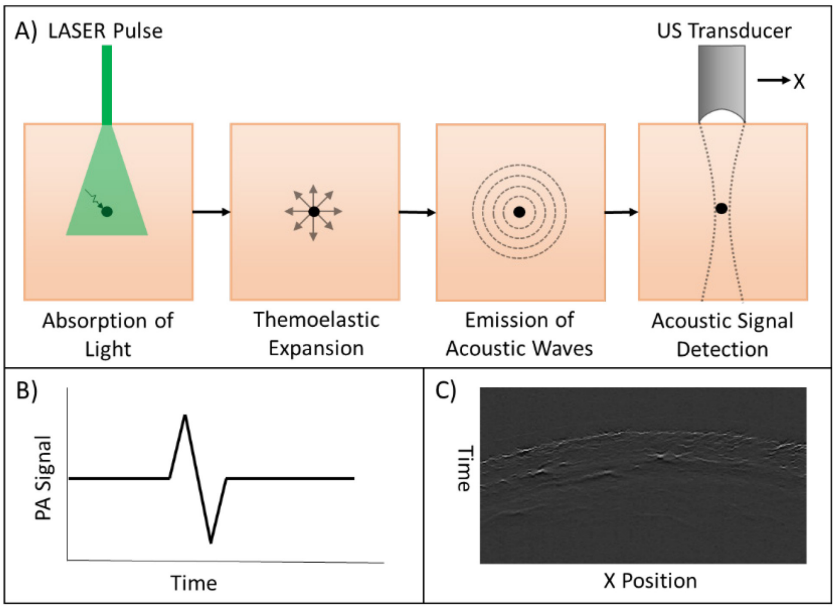

Figure 2.1 Principles of photoacoustic imaging. (A) When a molecule absorbs pulsed light, it can heat up and undergo thermo-elastic expansion. The sudden expansion generates acoustic pressure waves that can be detected by an ultrasound transducer. (B) For spherical absorbers, photoacoustic signals are typically N-shaped due to inward and outward pressure waves emanating from the surface [107]. The width of the N-shape is proportional to the size of the absorber. By scanning the ultrasound transducer or by having an array of ultrasound detectors, two-dimensional B-scans (C) or three-dimensional C-scans can be formed.

For the effective generation of photoacoustic waves, the optical pulse width must be less than both the thermal and stress confinement times [26]. Thermal confinement requires the pulse width to be less than the thermal diffusion time of the absorbed energy, which is given by the thermal relaxation time, $\tau_{th} = d_c^2/\alpha_{th}$ where d_c is the characteristic dimension and α_{th} is the thermal diffusivity of the molecules. Typically, the more restrictive criteria is stress confinement which requires volumetric expansion of the molecule to be negligible compared to the duration of the optical pulse. The expansion time can be given by the stress relaxation time, $\tau_s = d_c/v_s$ where v_s is the speed of sound. To satisfy both criteria, the pulse width of the light is often only

nanoseconds in duration. If both thermal and stress confinement are satisfied, the initial photoacoustic pressure generated within the sample can be given by the fluence, Φ, the absorption coefficient, μ_a, the thermal coefficient of the volume expansion, β, the speed of sound, v_s, and the specific heat capacity, C_p, as shown in Eq. 1.

$$p_0 = \Phi\mu_a\left(\frac{\beta v_s^2}{C_p}\right) = \Phi\mu_a\Gamma \quad (1)$$

The term Γ in Eq. 1 is commonly known as the Grüneisen parameter, which represents the effect that volume or temperature has on the vibrational properties of the sample.

2.5.2 Photoacoustic Imaging Configurations

There are many different configurations that enable imaging of the photoacoustic effect. Broadly, photoacoustic imaging can be divided into two main categories: photoacoustic computed tomography and photoacoustic microscopy. Photoacoustic microscopy can be further divided into acoustic-resolution and optical-resolution photoacoustic microscopy. Although the work presented in this dissertation primarily focuses on using acoustic-resolution photoacoustic microscopy to detect photoacoustic signals and reconstruct images, all these imaging configurations will briefly be discussed here.

2.5.2.1 Photoacoustic Computed Tomography

Photoacoustic tomography uses mechanically-scanned transducers or electronically-scanned multi-element transducer arrays to reconstruct images. Each detector has a large acceptance angle for photoacoustic signals so that a meaningful image can only be presented by combining the data from all the detectors. By scanning the multi-element transducer arrays in one direction a three-dimensional reconstruction is achievable. Many reconstruction techniques have been developed including the delay-and-sum beamforming, universal back-projection and time-reversal techniques, as well as other iterative methods [19, 108–110]. Although high frame rate cross-sectional imaging is achievable [111], the imaging resolution of photoacoustic tomography is usually limited to several hundreds of micrometers [112].

2.5.2.2 Photoacoustic Microscopy

Acoustic-resolution photoacoustic microscopy uses a focused ultrasound transducer and loosely focused light to detect photoacoustic signals. Since the ultrasound detector is focused, the received signal is essentially beamformed representing a one-dimensional depth-resolved image,

typically known as an A-scan line. By scanning the ultrasound transducer laterally, photoacoustic microscopy can be extended to represent a two-dimensional image (known as a B-scan) or a three-dimensional image (known as a C-scan). The axial and lateral resolution of these system is based on the acoustic characteristics of the ultrasound transducer, which allows high-resolution imaging beyond the optical transport mean free path at high-frequencies. For example, a 50 MHz high-frequency transducer was able to achieve 3 mm depth with 15 μm lateral resolution and 45 μm of axial resolution [113]. Although higher resolution is achievable with higher frequency transducers, difficulties in manufacturing such transducers has limited acoustic-resolution photoacoustic microscopy for micron or sub-micron imaging.

Optical-resolution photoacoustic microscopy offers micron or sub-micron resolution imaging [114]. This is accomplished by focusing the light to a micron or sub-micron spot size. Since the photoacoustic signal is generated only within the optically-focused laser spot, this technique enables photoacoustic imaging with diffraction-limited resolution. Since only one-way light propagation is required, optical-resolution photoacoustic microscopy can provide high-resolution imaging deeper than most optical imaging techniques.

2.5.3 Applications of Photoacoustic Molecular Imaging

Over the past decade, photoacoustic imaging as a preclinical and clinical imaging modality has grown rapidly for many different biomedical disciplines including oncology [115–118], cardiology [119–123], neurology [124–127], ophthalmology [128, 129], dermatology [26, 130–132], and gastroenterology [26, 133]. Due to the availability of endogenous optically absorbing molecules, many of these applications have been possible through non-invasive imaging mechanisms. For instance, as one of the predominant optically-absorbing molecules in tissues, hemoglobin has been used to non-invasively study the vascular structure of tissues [19, 134–137]. Exogenous optically-absorbing contrast agents, such as dyes and metallic nanoparticles, have further enhanced the potential utility of photoacoustic imaging for many different applications [24, 104]. Finally, like optical imaging, genetically-encoded molecules have great potential for photoacoustic imaging in preclinical and translation research. These reporter molecules can enhance our understanding of biological processes and may allow non-invasively monitoring of therapeutic efficacies.

2.5.3.1 Endogenous contrast agents for Photoacoustic Imaging

Due to their high optical absorption coefficients, hemoglobin, melanin, and lipids have been widely investigated as endogenous contrast agents for photoacoustic imaging of tissues. As the predominant optical absorber in tissues, hemoglobin has been used to visualize and study vascular networks non-invasively and label-free using photoacoustic imaging. Imaging of the vascularity in tissues is important for many different applications, most notably in cancer research [115, 138, 139]. Cancer is often accompanied by angiogenesis, the growth of new blood vessels, that enables tumors to thrive. Anti-angiogenesis drugs have been used as potential therapeutics for many cancers; however, it is often difficult to non-invasively assess their efficacy [139, 140]. By using photoacoustic imaging, the blood vessels surrounding cancers can be non-invasively mapped over a longitudinal study to understand how a treatment is affecting a tumor [138, 141]. Using photoacoustic imaging to reveal this in the clinic may have great importance when determining if the current treatment is working or a new form of treatment should be pursued.

Hemoglobin has another interesting property that allows photoacoustic imaging to obtain additional functional information in tissues without the aid of additional contrast agents. The absorption spectrum of hemoglobin changes when the molecule is bound to oxygen [24, 142]. Since the photoacoustic signal is directly related to the optical absorption of a molecule, this property of hemoglobin allows multiwavelength photoacoustic imaging of hemoglobin to determine the relative concentrations of oxygenated and deoxygenated hemoglobin. With two wavelengths, λ, Eq. 1 can be rewritten as matrix of equations as shown in Eq. 2, where the absorption coefficient has been substituted by the extinction coefficient, ε, multiplied by the concentration, C, *i.e.* $\mu_a = \varepsilon C$.

$$\begin{bmatrix} p_{0_{\lambda_1}} \\ p_{0_{\lambda_2}} \end{bmatrix} = \Gamma\Phi \begin{bmatrix} \varepsilon_{oxy_{\lambda_1}} & \varepsilon_{deoxy_{\lambda_1}} \\ \varepsilon_{oxy_{\lambda_2}} & \varepsilon_{deoxy_{\lambda_2}} \end{bmatrix} \begin{bmatrix} C_{oxy} \\ C_{deoxy} \end{bmatrix} \tag{2}$$

Since the extinction coefficient of hemoglobin is known [142, 143], the Grüneisen parameter is assumed to be constant, the fluence and the pressure detected can be measured, the concentrations of oxyhemoglobin, C_{oxy}, and deoxyhemoglobin, C_{deoxy}, can be determined and both oxygen saturation and total hemoglobin can be determined. Eq. 2 can be expanded to determine the relative concentration of additional molecules. Due to noise in the measurements, solving the inverse problem in Eq. 2 is not necessarily trivial and advanced demixing techniques may be needed to robustly determine the concentration of the constituent molecules in the

samples. Also note that Eq. 2 assumes that the fluence of each wavelength is the same at each depth, which is not necessarily true. Using these techniques, photoacoustic imaging has been used to visualize and study oxygen saturation and total hemoglobin [25, 72, 134, 144, 145].

As another strong optical absorber in tissues, melanin has also been investigated as an endogenous contrast agent for photoacoustic imaging. Photoacoustic imaging of melanoma can reveal the penetration depth of the tumor and can detect melanoma metastasis [132, 135, 136, 146, 147]. Additionally, circulating melanoma cells in blood have been detected using photoacoustic imaging [148, 149]. Similarly, photoacoustic imaging of lipids has been useful for detecting and examining atherosclerosis [19, 104, 137, 150]. Combining the multiwavelength approaches described above, photoacoustic imaging can visualize the oxygenation in the surrounding blood vessels while also distinguishing photoacoustic signals from melanin and lipids.

2.5.3.2 Exogenous contrast agents for Photoacoustic Imaging

Although endogenous reporter molecules have great utility in photoacoustic imaging, they can only be used to visualize a limited range of biological processes. Many exogenous reporter molecules have been investigated for photoacoustic imaging including dyes [24, 49, 98, 103, 151–155], porphysomes [39, 100, 102], perfluorocarbon nanodroplets [98, 103], gold nanoparticles [156, 157], carbon nanotubes [155, 158], and up-conversion nanoparticles [159].

Methylene blue dye can stain lymph nodes and has aided in locating sentinel lymph nodes for biopsies. In 2008, photoacoustic imaging was used in preclinical studies to aid in locating sentinel lymph nodes [49]. In 2015, a pilot clinical study was conducted using methylene blue to detect lymph nodes [160]. With demixing techniques, photoacoustic imaging can visualize the lymph nodes with high contrast. Methylene blue has also been added to microbubbles to provide dual-modality ultrasound and photoacoustic contrast agents [98]. Due to its triplet-excited state, methylene blue also has a long lifetime which enables another form of contrast. Lifetime photoacoustic imaging of methylene blue uses a pump laser pulse to make methylene blue enter a triplet-excited state. Since methylene blue returns to the ground state slowly, probe pulses at varying time intervals after the pump pulse will result in different photoacoustic signals. Differential imaging can then be used to nullify background signals from molecules that return to ground state quickly and highlight molecules that return to ground state slowly. In this dissertation, I investigate a novel photoacoustic pulse sequence to image the ground-state recovery and the excited-state lifetime of methylene blue and other molecules.

Another highly absorbing dye is the FDA-approved indocyanine green, which has been used to image lymphatic structure [152] and has been combined with other targeted agents to provide photoacoustic signal [153, 154]. Gold nanoparticles have been extensively studied for photoacoustic imaging due to their high-optical absorption and adaptability for surface modifications making them more biocompatible and giving them targeting capabilities [157].

Combined with some dyes, perfluorocarbon microbubbles and nanodroplets have also been used as exogenous contrasts agents [98, 103]. Recently there has been rising interest in porphyrins for photoacoustic applications. Lovell *et al.* showed that porphysomes – nanovesicles created from porphyrin bilayers – could accumulate around xenograft tumors in mice, enhancing the photoacoustic signal generated [102]. Moreover, the porphysomes could induce photothermal ablation of the tumor when exposed to light, suggesting that porphysomes have utility as a therapeutic. In 2014, Huyhn *et al.* demonstrated a porphyrin-based microbubble that could be used for ultrasound and photoacoustic imaging, as well as fluorescence imaging [100].

2.5.3.3 Genetically-Encoded Reporters

Although exogenous contrast agents have great utility, genetically-encoded reporters are better for understanding and investigating biological processes. One of the first report genes investigated for photoacoustic imaging was the *lacZ* gene which encodes the enzyme β-galactosidase [24, 74, 161]. β-galactosidase metabolizes the substrate X-gal into a strong optically-absorbing, indigo-like molecule. Unfortunately, this reporter molecule requires X-gal, which is not naturally produced and needs to be locally injected for the product to be generated. Furthermore, the product is not cleared well *in vivo*.

Since melanin is a strong naturally occurring molecule, genetically-encoded reporters have been made to generate melanin precursors molecules such as tyrosinase [75, 162–164]. In high concentrations, some melanin precursors are cytotoxic [165] so inducible systems have been developed [75]. Intrinsic signal amplification by these enzymes produces a very high concentration of these pigments in living cells.

Similar to optical imaging, fluorescent molecules can be used for photoacoustic imaging. In 2009, Razansky *et al.* demonstrated tissue-specific expression of fluorescent proteins (green fluorescent protein (GFP) and mCherry) several millimeters deep in tissues with higher spatial resolution than typical fluorescent imaging (38 μm vs. 1 mm, respectively) [166]. The most common type of

fluorescent protein is GFP – a 236-amino acid protein isolated from *Aequorea victoria* that has a β-barrel structure shielding an internal fluorophore from the surrounding molecular environment [15]. Aside from oxygen, GFP's internal fluorophore is formed without requiring additional cofactors, prosthetic groups or enzymes. Due to its blue-shifted absorption peak (395 and 475 nm), emission peak (509 nm) and the high intrinsic absorption of endogenous molecules in tissues, GFP can only be used superficially or in nearly-transparent organisms. As wavelength increases scattering lessens so near-infrared molecules are preferred. Phytochrome-based near-infrared fluorescent proteins provide a much better reporter molecule for both optical and photoacoustic imaging [127, 167]. In 2016, photoacoustic imaging of a calcium-sensitive fluorescent protein in zebrafish was reported [127]. Calcium-sensitive fluorescent proteins have been very important in optical imaging and allow the monitoring of action potentials in the nervous system [168]. An action potential typically causes a conformational change within these proteins that affects the absorption and/or emission spectra of the protein. Unfortunately, fluorescent proteins have been optimized to have high quantum yield which is detrimental to photoacoustic imaging as most of the input energy is converted to light rather than heat.

Recently, another class of proteins have been gaining interest for photoacoustic imaging. Chromoproteins have low quantum yield and high optical absorption. Ultramarine and cjBlue are chromoproteins that can absorb red light making them promising candidates for photoacoustic imaging [169, 170]. Laufer *et al.* [27] has compared the photoacoustic signal from various fluorescent proteins to the chromoprotein cjBlue and found that the chromoprotein gave much higher photoacoustic signal and was more robust to laser-induced bleaching after repetitive laser exposure. In this dissertation, I will discuss collaborative efforts to optimize chromoproteins for photoacoustic imaging using directed evolution approaches.

Chapter 3 Ultrasound-Aided Biomarkers Liberation

Biomarkers are important diagnostic and prognostic tools that may be used to accurately and reliably classify many diseases, including cancer. Biomarkers are being explored for many diseases including stroke [171], depression [172], and cancer [173–176]. Despite tissue biopsies being technically challenging, dangerous in some very vascularized tissue, and may possibly promote metastasis [76, 77], biopsies are still the gold standard for assessing the biomarkers in tissues due to their high degree of accuracy, reliability, and specificity. There is much research into alternative means to assess the biomarkers in tissues. One of the most promising candidates are liquid biopsies such as blood tests [7, 177–179]. For liquid biopsies, there have been several clinically-relevant biomarkers found including carcinoembryonic antigen (CEA) [78], prostate-specific antigen [4, 8], and CA-125 [179] for colon, prostate, and ovarian cancer, respectively. Although blood-borne biomarkers have great potential, they are typically found in very low concentrations. Furthermore, biomarkers detected in blood cannot indicate the origin of the biomarkers and have no baseline for comparison.

Ultrasound may provide the key to overcoming these issues. Ultrasound-cell interactions typically result in an increased permeability in the cell membrane due to transient pores forming in the membrane, a process known as sonoporation [95]. This effect can be enhanced by using ultrasound contrast agents such as lipid-stabilized microbubbles. Sonoporation has typically been used for applications involving drug delivery and gene transfection [180–183]. However, in 2009, D'Souza *et al.* showed that colon cancer tissue exposed to ultrasound releases the protein CEA into the surrounding media [28]. Not only did this increase the concentration of CEA, but by taking samples before and after insonification, it provided a mechanism to determine the origin of biomarkers and a baseline could be formed. Figure 3.1 shows the basic workflow of this procedure. In 2010, Kaddur showed that microbubble-enhanced sonoporation could release enhanced green fluorescent protein from cells [184]. In 2012, Fan *et al.* demonstrated transport kinetics of fluorescent molecules into a cell using microbubble-enhanced sonoporation [185].

They demonstrated that a single bubble cavitating near cells could allow entry of impermeable propidium iodide and fluorescent calcein into the cells in *in vitro* studies.

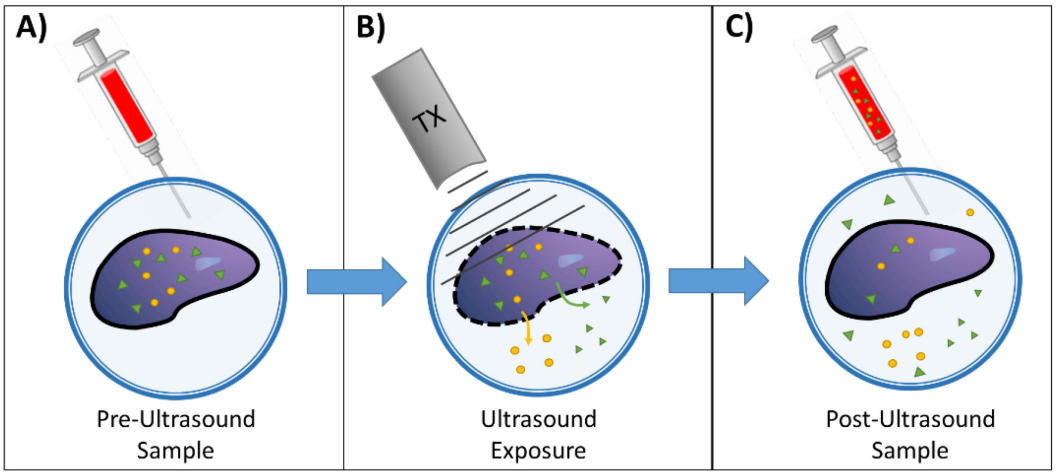

Figure 3.1 Diagram of the ultrasound-aided biomarker liberation processes. (A) A pre-ultrasound sample of the surrounding media is taken as a baseline. (B) The samples are exposed to ultrasound causing transient pores to form releasing biomarkers. (C) A post-ultrasound sample of the surrounding media is taken and the biomarkers are compared to the baseline.

As one of the key questions being addressed in this research, we wanted to further explore how much additional molecular information could be extracted using ultrasound to liberate biomarkers. Since D'Souza *et al.* [28] only demonstrate the effectiveness of ultrasound for liberating protein-based biomarkers, we were interested in extending this technique to other types of biomarkers, specifically nucleic acid biomarkers. For the first time, our work, presented in Chapters 4 and 5, demonstrated that the concentration of free-circulating RNA molecules, such as messenger RNA and micro-RNA, could be enhanced using ultrasound. Furthermore, for the first time we demonstrated that ultrasound contrast agents like lipid-stabilized microbubbles dramatically increase the release of these RNA molecules. This work represents an important step into making some biomarkers more viable in liquid biopsies, potentially reducing the number of tissue biopsies required.

Although there are several ways to quantify the biomarkers in liquid biopsies, we used quantitative PCR (qPCR) as it has high-specificity, seven orders of magnitude dynamic range, and near single-copy sensitivity. Use of qPCR with TaqMan probes and primers has also been well-established in the literature [186, 187]. As an alternative technique, mass spectrometry has great utility for assessing biomarkers in liquid biopsies [188, 189]. However, it has primarily been used

to characterize protein biomarkers and only recently has RNA identification been proposed using mass spectrometry [190].

In Chapter 6, additional contribution to this field of study are presented including work on utilizing nanodroplets to enhance biomarker concentration. Using nanoscale vesicles may be important as they may be able to passively leak out of diseased vasculature and accumulate near target tissue. Finally, during these investigation, we also discovered that ultrasound causes the release of micro-vesicles from cells, which contain a wealth of diagnostic and prognostic information and have led to interesting research that is briefly discussed in Chapter 6.

Chapter 4 Microbubble-Enhanced Ultrasound Liberation of mRNA Biomarkers *In Vitro*

The work presented in this chapter has been published and taken with permission from A. Forbrich, R. Paproski, M. Hitt, and R. Zemp, "Microbubble-Enhanced Ultrasound Liberation of mRNA Biomarkers *In Vitro*" published in *Ultrasound in Medicine and Biology* [29]. The introduction has been modified for structural and formatting reasons.

4.1 Introduction

As one of the leading causes of deaths in women, there has been much effort for early diagnosis and prognosis of breast cancer. However, the heterogeneity of breast cancer tumors requires the development of reliable imaging technologies with the ability to characterize biomarkers. As the principal prognostic markers for breast cancer, estrogen receptors, progesterone receptors, and HER2 can classify tumors and direct treatment. Triple-negative tumors, however, have many prognostic challenges and additional biomarkers are necessary to assess these phenotypes [191]. Unique signatures using multiple biomarkers have been investigated as tools for enhanced specificity and molecular profiling of various diseases [192]. Although most of these biomarkers involve solid tissue biopsies, several liquid biomarkers have been found for breast cancer such as cancer antigen 15-3. Moreover, free-circulating tumor DNA has been found in some liquid biopsies [5, 193]. Liquid biopsies have many challenges, including low concentrations of biomarkers.

To enhance the concentrations of biomarkers in blood, we investigated using ultrasound to increase the permeability of cells. Specifically, for this work, we investigate mammaglobin messenger RNA (mRNA) encoding mammaglobin as a potential prognostic blood biomarker for metastatic breast cancer. Although only found in 50-80% of breast cancer [194, 195] and expressed in several other tissues including the skin and sweat glands, mammaglobin mRNA coupled with an array of other biomarkers could be used to diagnose breast cancer and to evaluate patient prognosis. Mammaglobin mRNA is used here as an example of a tissue-specific

nucleic acid biomarker that is normally absent in mice and hence may be ideal for future animal studies. Moreover, mammaglobin mRNA may be used to assess suspicious lesions in tissues that do not express mammaglobin enabling the identification of breast cancer metastasis using ultrasound and blood tests. Since sonoporation has been suggested as the underlying factor for ultrasound-aided biomarker liberation [28], we demonstrate that microbubble contrast agents, known to enhance sonoporation, are capable of further increasing the biomarker liberation from cells without significantly impacting the viability of the cells.

4.2 Materials and Methodology

4.2.1 Cell Culture

All experiments were conducted using the ZR-75-1 breast cancer cell line (American Type Culture Collection). For *in vitro* experiments, each well of a 12-well plate was inoculated with 2×10^5 ZR-75-1 cells cultured in 2 mL of growth medium (RPMI-1640 medium supplemented with 10% fetal bovine serum (FBS)). These cells were incubated at 37°C for three days at which point the cells were approximately 85% confluent.

4.2.2 Sampling and Sonification Procedure

Prior to each experiment, the growth medium was aspirated and the cells were washed with 1 mL of phosphate buffered saline (PBS) to remove any background mammaglobin biomarkers. The PBS was aspirated and 1 mL of growth medium was added to each well. If lipid-stabilized microbubbles were used in the experiment, the growth medium was first mixed with microbubbles (see microbubble preparation below) in a separate 1.5 mL tube to create a solution of 4×10^7 microbubbles/mL before adding to the well to try to maintain a more homogenous solution. This concentration of microbubbles was chosen to match many of the reported gene transfection procedures. After gently mixing the well for 10-15 seconds a 480 μL pre-ultrasound medium sample was taken.

The 12-well plate was half-immersed in a 37°C water bath overtop of a 1 MHz, unfocused ultrasound transducer (Sonidel SP100 Sonoporator, Sonidel Limited, Raheny Dublin, Ireland). The cells were sonicated with variable intensities, durations, and duty cycles to determine the optimal ultrasound parameters. Throughout the experiment, the transducer was moved to guarantee all cells in the well were hit with ultrasound. After sonication, the plate was gently mixed for 10-15 seconds and a 480 μL post-ultrasound medium sample was taken. The pre- and post-ultrasound

samples were centrifuged at 16,000 rcf (relative centrifugal force) for 1 minute to remove any detached cells and 450 μL of the supernatants were transferred to 1.5 mL tubes, flash frozen in liquid nitrogen, and stored in a -80°C freezer. The remaining supernatant and cell pellet of the post-ultrasound sample were used in characterizing the cell viability (see below). Each experiment was conducted at least three times.

The intensity calibration on the SP100 transducer system was confirmed to within 10% error using a hydrophone (HNP-400, Onda, Sunnyvale, California) to probe the maximum acoustic intensity generated by the transducer at varying system settings. Measurements were taken 1 and 2.5 cm from the transducer head in a water tank.

4.2.3 Microbubble Preparation

The procedure to manufacture lipid-stabilized microbubbles was adapted from Chen *et al.* [180]. A lipid stock solution was prepared consisting of 27 mg/mL 1,2-dipalmitoyl-sn-glycero-3-phosphocholine (Sigma, Saint Louis, MO, USA), 3 mg/mL 1,2-dipalmitoyl-sn-glycero-3-phosphoethanolamine (Sigma, Saint Louis, MO, USA), and 100 mg/mL glucose dissolved in PBS. In brief, 350 μL of the lipid stock solution, 5 μl of 10% albumin solution, and 50 μL of glycerol were combined in a 1.5 mL tube. The air was replaced with octafluoropropane gas (Electronic Fluorocarbons, LLC, Hopkinton, MA, USA) and the tube was vigorously shaken for 30 seconds using a mechanical shaker (D-640 Amalgamator, TPC, City of Industry, CA, US).

The microbubbles were characterized using a particle counter (Z2 Particle Count & Size Analyser, Beckman Coulter). The average concentration of microbubbles, the mean microbubbles diameter, and the mode diameter were 3.6×10^9 microbubbles/mL, 3.26 μm, and 2.40 μm, respectively.

4.2.4 Cell Viability Analysis

After the experiments, the cells in the wells were washed with PBS and trypsinized. The PBS wash, the trypsinized cells, and the remaining supernatant and cell pellet of the post-ultrasound sample from the centrifugation step were combined in a 15-mL centrifuge tube. RPMI growth medium with 10% FBS was added to neutralized the trypsin. The cells were centrifuged at 1,000 rcf for 7 minutes and the supernatant was aspirated. The cells were washed once with PBS, centrifuged at 1,000 rcf for 7 minutes and the supernatant was aspirated. A hemocytometer and trypan blue staining were used to assess cell viability. At least 200 cells were counted in each experiment and each experiment was conducted at least three times.

4.2.5 Biomarker Level Analysis

Quantification of the mammaglobin mRNA biomarker levels in the samples was completed using a three-step procedure – RNA purification, reverse transcription, and quantitative PCR with TaqMan probes and primers. First, the mRNA was purified using total RNA purification kits (miRNeasy Mini Kit, Qiagen). The RNA was eluted with 30 μL of RNase-free water and the eluate was passed through the spin column a second time for higher mammaglobin concentration. Second, the mammaglobin mRNA was reverse transcribed to cDNA using TaqMan Reverse Transcription Kits (Applied Biosystems). The volumes indicated in the protocol were adjusted to make a final volume of 50 μL. Only 10 μL of the purified RNA was reverse transcribed. Third, mammaglobin-specific TaqMan probes and primers (Hs00267190_m1, Applied Biosystems) were combined with 20 μL of the mammaglobin cDNA and TaqMan Universal Master Mix without AmpErase UNG (Applied Biosystems). The samples were analysed using a 7900HT Fast Real-Time PCR System (Applied Biosystems).

A known concentration of purified mammaglobin cDNA was purchased from GenScript and was used to generate a standard curve which quantifies the number of mammaglobin cDNA copies present in the reverse transcribed sample. Figures are corrected to account for dilutions in the sample collection, purification, reverse transcription, and TaqMan PCR steps so that our quantification represents the total number of mammaglobin mRNA molecules released into the surround medium. The reverse transcription step was assumed to be 100% efficient.

4.2.6 Biomarker Liberation due to Cell Death

To quantify the number of mammaglobin mRNA copies released due to cell death, media samples were taken from cells incubated with varying concentrations of hydrogen peroxide for 30 minutes. High concentrations of hydrogen peroxide were necessary to cause sufficient cell death after 30 minutes – the maximum duration of ultrasound in our experiments. The cells were cultured, samples were collected and analysed, and cell death was assessed as described above.

4.3 Results

Two preliminary experiments were conducted prior to exposing cells to ultrasound. First, the RPMI growth medium with 10% FBS was verified to have no mammaglobin mRNA naturally present (results not shown). Second, ZR-75-1 cells were washed with PBS and new growth medium was added, sampled at 0 and 30 minutes, and were found to have no statistically

significant difference in mammaglobin mRNA copies – 0 and 30 minutes had 495 ± 248 and 603 ± 165 mammaglobin mRNA copies per 100,000 cells, respectively. Three important ultrasound parameters were examined in this work – duty cycle, intensity, and exposure duration.

Duty cycle was examined by using the 1 MHz, unfocused transducer to sonicate cells in a 12-well plate for 10 and 20 minutes at 2 W/cm^2 without microbubbles. Specifically, mammaglobin biomarker liberation was examined at 30% and 50% duty cycle, see Figure 4.1. These settings were chosen to verify that ultrasound caused mRNA release, similar to the CEA protein that D'Souza *et al.* [28] examined. Mammaglobin mRNA release was substantially enhanced at higher duty cycles. An order of magnitude increase in mammaglobin mRNA copies was seen at 50% duty cycle compared to 30% duty cycle. All future experiments used 50% duty cycle, since these results and D'Souza *et al.* [28] both indicated that 50% duty cycle is necessary for adequate biomarker liberation.

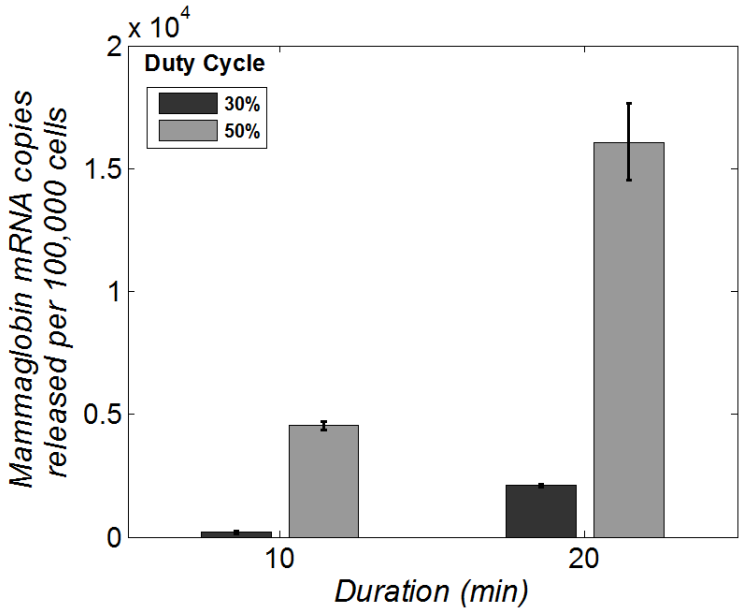

Figure 4.1 Effects of ultrasound duty cycle on mammaglobin mRNA release. Estimated number of mammaglobin mRNA copies released into the growth medium at varying duty cycles, no microbubbles present. Cells were exposed to 2 W/cm^2 ultrasound [29].

Figure 4.2 depicts the cytotoxicity curve generated by exposing the ZR-75-1 cells to 0, 10, 50, 100, 125, and 200 mM of hydrogen peroxide in RPMI growth medium for 30 minutes. These concentrations were examined because they adequately covered the entire range of cell viability in our experiments. A concentration of 200 mM was found to cause near 0% cell viability with

little excess hydrogen peroxide and is used as the maximum concentration for biomarker release. Biomarker liberation at each concentration was assessed and the corresponding cell death equivalent biomarker release is presented in Figure 4.3C.

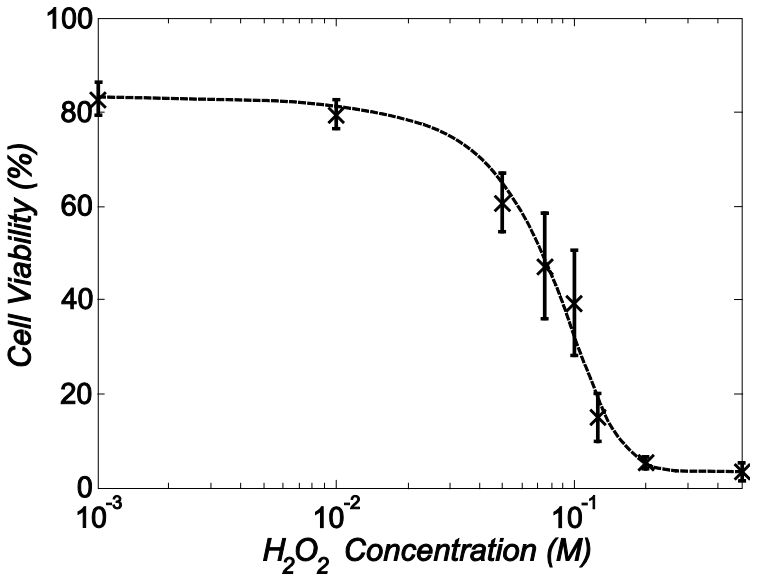

Figure 4.2 Hydrogen peroxide (H_2O_2) cytotoxicity curve. Hydrogen peroxide at varying concentrations were added to ZR-75-1 cells in RPMI growth medium. Cell death was assessed with trypan blue staining [29].

Ultrasound intensity was examined by varying the intensity setting on the SP100 system between 0.1 and 5.0 W/cm^2 with either the presence or the absence of microbubbles at 50% duty cycle and for 10 minutes of exposure, see Figure 4.3A for biomarker release data and Figure 4.3B for cell death at each intensity. Biomarker liberation due to cell death is superimposed on Figure 4.3A, interpolated from the cell death equivalent biomarker release experiments with hydrogen peroxide (Figure 4.3C). Ultrasound consistently amplified the release of mammaglobin mRNA better when microbubbles were present providing 2-3 orders of magnitude increase in biomarker levels compared to the pre-ultrasound sample (not shown). At low intensities, < 1 W/cm^2, microbubbles caused 10-15 fold increase in the amount of mammaglobin mRNA copies released. At high intensities, > 1 W/cm^2, microbubbles did not enhance biomarker liberation substantially compared to ultrasound alone. At the same time as investigating the biomarker liberation-ultrasound intensity relationship, we examined the cell viability-acoustic intensity relationship. Figure 4.3B shows that the addition of microbubbles caused an increase in cell death compared to just ultrasound alone, increasing cell death by 20%. Finally, the duration of ultrasound exposure was examined by using a 1 W/cm^2, 50% duty cycle ultrasound and varying the exposure time

between 1 and 30 minutes, see Figure 4.4. Without microbubbles, the biomarker liberation steadily increased and reached a steady state after 30 minutes. However, with microbubbles the biomarker liberation peaked early at 1 minute and began to decrease steadily.

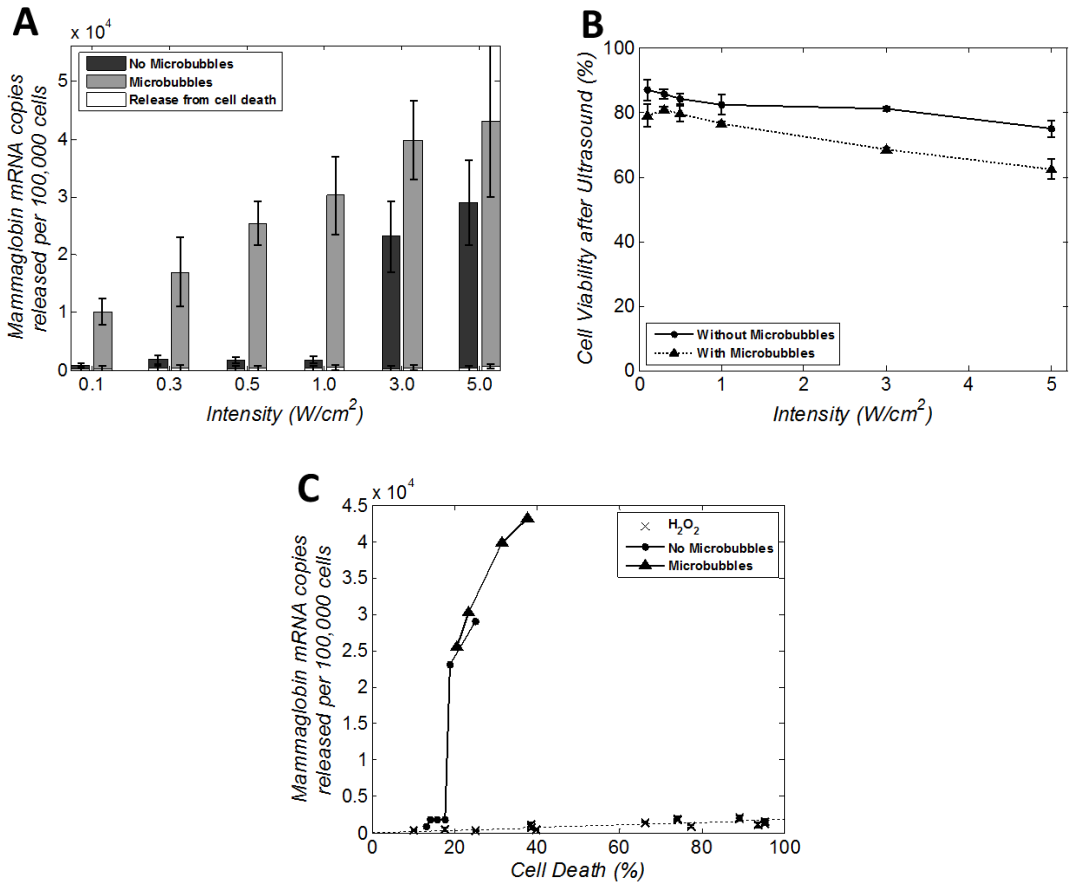

Figure 4.3 Mammaglobin mRNA release and cell response to increasing ultrasound intensity. At each intensity ultrasound was applied for 10 minutes at 50% duty cycle. A) Depicts the number of mammaglobin mRNA copies released into the surrounding medium, compared to the pre-ultrasound sample. The white bars indicate the cell death equivalent biomarker release interpolated from the H_2O_2 cell death studies shown in C. B) Depicts the cell death caused at varying ultrasound intensity. C) Depicts the biomarker release at the measured cell death during ultrasound exposure and incubation with hydrogen peroxide. Biomarker release due to cell injury from incubation with H_2O_2 (dashed lines with 'x' markers) contributes a small portion of biomarker release [29].

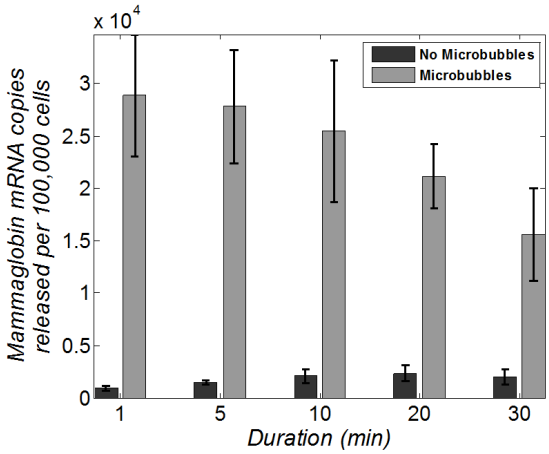

Figure 4.4 Effects of ultrasound exposure duration on mammaglobin mRNA release. Estimated number of mammaglobin mRNA copies released at varying ultrasound exposure durations. ZR-75-1 cells were exposed to 1 W/cm^2, 50% duty cycle unfocused ultrasound in the presence or the absence of microbubbles [29].

4.4 Discussion

We demonstrate that the technique developed by D'Souza *et al.* works not only for proteins but also cytoplasmic nucleic acids, specifically mammaglobin mRNA. We analysed mRNA using qPCR which has many advantages over other common quantitative analysis techniques. qPCR with TaqMan probes has high specificity, a large dynamic range of over seven orders of magnitude, and has near-single copy sensitivity all of which are important for working with serum or blood-borne biomarkers. Even without microbubbles (dark grey bars in Figure 4.3A) the high-intensity ultrasound technique proposed by D'Souza *et al.* [28] is able to amplify the release of mammaglobin mRNA substantially; however, specialized ultrasound transducers may be necessary to achieve and maintain these high-intensities and high duty cycles in the clinic. At 1 W/cm^2, the addition of microbubbles causes biomarker liberation to exceed the biomarker liberation caused from ultrasound alone at 5 W/cm^2. Although current clinical imaging systems cannot maintain the required high duty cycles for biomarker release, the 5-fold reduction in intensities could lead to the development of new clinical ultrasound imaging systems to handle low-duty cycle imaging and high-duty cycle biomarker liberation at current FDA-approved imaging intensities. Furthermore, there are several FDA-approved microbubbles that could be used which would help the introduction of this technique into the clinic.

Our data demonstrates that microbubbles enhance the biomarker levels by 2-3 orders of magnitude compared with the pre-ultrasound samples and over an order of magnitude compared to ultrasound without microbubbles. The addition of microbubbles increases cell death (Figure 4.3B); however, the substantial increase in mammaglobin mRNA biomarkers is attributed to the microbubbles as opposed to the increased cell death as seen in Figure 4.3A and Figure 4.3C. Although the mechanism of biomarker release from ultrasound induced cell death and hydrogen peroxide induced cell death may not be identical, the hydrogen peroxide studies are useful and give insight into the proportion of biomarkers released from sonoporation versus the release from cell death. Although there is increased cell death, the use of a focused ultrasound transducer would substantially limit death of non-target tissue. Focused ultrasound coupled with quantitative thermometry techniques such as ultrasound or magnetic resonance guided therapies could also be used to further reduce high-intensity ultrasound exposure to undesired tissues. Since the target tissue mass identified sonographically or with other imaging modalities would most likely be an abnormal tissue, the increased cell death would likely be deemed acceptable and may further enhance the biomarker release.

At low intensities (< 1 W/cm^2), the biomarker liberation is significantly enhanced with microbubbles. This is most likely due to the microbubbles undergoing stable cavitation at low acoustic intensities and unstable cavitation at high acoustic intensities. Stable cavitation helps maintain the transient pores in the plasma membrane without rapidly destroying the microbubbles [22] and allows more time for the biomarkers to release into the surrounding medium. Unstable cavitation initially causes more stress on the cell [196] and most likely causes a rapid increase in biomarker concentration outside of the cell; however, the microbubbles are destroyed rapidly and the pores are not maintained throughout the procedure making biomarker release rely solely on the acoustic pressure. Since *in vivo* studies would rely on the circulatory system to distribute the microbubbles continuously, unstable cavitation might be necessary to induce rapid biomarker release as the microbubbles will not remain stationary beside the tissue of interest. However, for *in vivo* studies an infusion system of microbubbles can overcome this issue as a continual supply of microbubbles will arrive at the target tissue. Furthermore, Figure 4.4 shows that biomarker release peaks early in the ultrasound exposure when microbubbles are present so exposing the target tissue for a short time should not cause great issues.

Although the trend of increasing biomarker liberation with increasing ultrasound intensity agrees with previously published work, the biomarker liberation-ultrasound exposure duration produced unexpected results when microbubbles were introduced, as seen in Figure 4.4. When microbubbles were present, the number of mammaglobin mRNA copies detected decreased as the exposure duration increased. The most likely cause of this decrease is natural RNA degradation from RNase; however, comparing the biomarkers released from a sample with and without RNase-inhibitors added did not have any significant difference in the number of mammaglobin mRNA biomarker detected (data not shown). Another potential cause of this decrease is that the cavitation of microbubbles can cause substantial, localized increases in temperature [197] or local shock-waves causing the mammaglobin mRNA to denature and degrade. Other possible causes could be the amount of time before sample is frozen and endocytosis of the mammaglobin mRNA back into the cells. Although unexpected, this result is not undesired and is promising for *in vivo* studies, shortening the necessary length of this procedure.

Clearly, this technique works well in cell cultures; however, several barriers may reduce the efficacy of this technique *in vivo*. Although the acoustic energy will be able to release biomarkers from tissues *in vivo*, the presence of an endothelial layer may act as a barrier limiting or preventing the diffusion of mRNA into the bloodstream. The effect of this barrier may be limited as several studies have shown that ultrasound and microbubbles can permeabilize skin [198], epithelial tissue [199], and the blood-brain barrier [200] for enhanced drug delivery. The enhanced permeability has been shown to last for several hours. Since ultrasound and microbubbles are already applied to the region, the endothelial layer may be permeable or semi-permeable allowing biomarkers to enter the bloodstream. Another potential obstacle for *in vivo* studies is the limited proximity of the microbubble to the cancerous tissue due to the endothelial layer. Some groups have overcome this issue by designing sub-micron microbubbles or sub-micron microbubble pre-cursors that can extravasate from the leaky vasculature surrounding most cancers and be activated manually [34]; however, the acoustic energy necessary to induce microbubble cavitation increases dramatically. Additional studies should be designed to determine the effect of the endothelial layer on biomarker release into the bloodstream.

The microbubble concentration used in the *in vitro* experiments will not directly translate into *in vivo* studies. Multiple factors will need to be considered when pursuing *in vivo* studies. First, the

microbubbles will flow past the target region via the circulatory system, reducing the duration of possible microbubble-tissue interactions. Short, high duty cycle bursts of ultrasound would be necessary to cause inertial cavitation and maximize the interaction. Although microbubble concentration would be reduced by the larger blood pool, an infusion of microbubbles can replenish the supply of microbubbles in low concentrations. Targeting microbubbles to specific cancers could also increase tissue specific interactions and increase local concentrations of microbubbles; however, different preparation techniques need to be used to create sub-micron microbubbles that will extravasate outside the vasculature. Additional studies should be designed to assess the minimum concentrations of microbubbles for sufficient biomarker release.

Aside from substantially enhanced biomarker release, microbubbles have high acoustic impedance mismatches which can provide high contrast ultrasound images with single-bubble sensitivity in ultrasound imaging [21]. This could be used to implement a dual-mode ultrasound system, which could image microbubble distribution and induce cavitation once the microbubbles reach the target tissue. Since our data demonstrates that low intensity ultrasound and microbubbles are capable of amplifying the release of mammaglobin mRNA, the proposed ultrasound system could potentially work within the clinically-approved FDA limit for diagnostic ultrasound imaging systems, 0.72 W/cm^2 without specialized HIFU ultrasound transducers. This system could allow *in vivo* studies to verify that microbubbles reach the target tissue before inducing stable cavitation. However, new transducers should be designed to allow for the high-duty cycle necessary for ample biomarker release. Further experiments are needed to determine which type of system would be necessary for *in vivo* and clinical trials.

While our *in vitro* experiments were conducted using 100% ZR-75-1 cells, additional studies could be used to assess mammaglobin mRNA in a mixture of mammaglobin producing and non-producing cells in a 12-well plate, which would better simulate *in vivo* situations. By varying the proportion of mammaglobin producing and non-producing cells, this could give insight into techniques to differentiate cell populations *in vivo* based on the enhanced biomarkers. Although mammaglobin mRNA is seen in many breast cancer tissues, it is not unique to mammary tissue; hence, to provide clinical usability further studies should be designed to analyse a multiplicity of biomarkers to improve characterization of breast cancer tissues using the molecular profile released into the surrounding medium. Additionally, studies should be conducted to see if this

technique can be extended to other types of biomarkers including surface-bound proteins, nuclear nucleic acids, and micro-RNA (miRNA) [201, 202].

4.5 Conclusion

In this chapter, we extend previous work on biomarker release using ultrasound to include mRNA. We also demonstrate significant enhancement of mRNA release using microbubbles as cavitation seeds. In our *in vitro* experiments, these microbubbles release up to 2-3 orders of magnitude more copies of mammaglobin mRNA compared to a pre-ultrasound sample, and 1-2 orders of magnitude more copies compared with just ultrasound alone.

Chapter 5 Comparing Efficiency of micro-RNA and mRNA Biomarker Liberation with Microbubble-Enhanced Ultrasound Exposure

In the previous chapter, the 502-nucleotide sequence mammaglobin mRNA was examined. We believed that large nucleic acids would be released less efficiently than small nucleic acids such as micro-RNA. The work presented in this chapter has been published and taken with permission from A. Forbrich, R. Paproski, M. Hitt, and R. Zemp, "Comparing Efficiency of micro-RNA and mRNA Biomarker Liberation with Microbubble-Enhanced Ultrasound Exposure" published in *Ultrasound in Medicine and Biology* [30]. The introduction has been modified for structural and formatting reasons.

5.1 Introduction

The large size of many mRNA molecules may limit efficiency of release from cells. One goal of this work is to investigate the hypothesis that smaller biomarker molecules will be released more efficiently compared to larger ones. A number of small molecule biomarker candidates could be considered; however, we choose to focus on micro-RNA (miRNA) as a related but smaller-sized class of the mRNA biomarkers we previously investigated (Chapter 4) for ultrasound-aided liberation.

Recently, there has been a rising interest in miRNA as potential biomarkers for many diseases including various forms of cancer [201, 203–208]. miRNAs are small non-encoding RNAs, typically less than 25 nucleotides in length, which regulate the expression of many genes. In many cancers miRNAs are substantially dysregulated creating a unique molecular profile capable of differentiating cancers and normal tissues [208, 209]. A unique signature of 13 miRNA has been associated with chronic lymphocytic leukaemia progression [210] and specific miRNA profiles have been correlated with estrogen and progesterone receptors, as well as HER2 – common receptors used to guide treatment and evaluate prognosis of breast cancer patients [205, 211,

212]. miRNA may also be advantageous compared to other RNA molecules in terms of stability. miRNA have been found to be much more stable in blood samples [213] and they do not degrade greatly in common collected, formalin-fixed, paraffin-embedded clinical tissue samples [209].

This work presents a study of how miR-21, a 22-nucleotide RNA molecule, is liberated by ultrasound and microbubbles. miR-21 is an ideal candidate miRNA biomarker as it is substantially upregulated in many cancers including breast, colon, pancreatic, prostate, and lung cancers [214]. We hypothesize that as the length of the nucleic acid decreases, the ability of ultrasound to amplify the release of the biomarker will increase. To demonstrate this, we show that miR-21 is released more efficiently compared to mammaglobin mRNA. Verification of this hypothesis, however, requires additional studies investigating a large library of nucleic biomarkers. We also show that microbubbles can be used to obtain substantial increases in biomarker levels for miR-21. To our knowledge, the findings reported here are the first to quantitatively compare cellular release efficiency of different sized biomarker molecules and suggest that other small molecules that are candidate biomarkers for a range of diseases could offer enhanced diagnostic sensitivity when liberated by ultrasound-microbubble exposure.

5.2 Methodology

5.2.1 Microbubble Preparation

Lipid-stabilized microbubbles were created by combining 350 μL lipid stock solution (27 mg/mL 1,2-dipalmitoyl-sn-glycero-3-phosphocholine (Sigma, Saint Louis, MO, USA), 3 mg/mL 1,2-dipalmitoyl-sn-glycero-3-phosphoethanolamine (Sigma, Saint Louis, MO, USA), and 100 mg/mL glucose dissolved in PBS), 5 μl of 10% (w/v) albumin solution, and 50 μL of glycerol in a 1.5 mL tube, replacing the air in the tube with octafluoropropane gas (Electronic Fluorocarbons, LLC, Hopkinton, MA, USA), and shaking the tube for 30 seconds using a mechanical shaker (D-650 Amalgamator, TPC, City of Industry, CA, US). This yielded an average concentration of 3.6×10^9 bubbles/mL with mean and mode diameters of 3.26 and 2.40 μm, respectively. This formulation was modified from Chen *et al.* [180] who demonstrated the microbubbles formulation potential for *in vivo* experiments. Using this formula allows future studies to investigate *in vivo* biomarker release using microbubbles without major modifications to the techniques presented here.

5.2.2 Sample Preparation and Collection

A procedure similar to Forbrich *et al.* [29] was used to allow direct comparison of mammaglobin mRNA to miR-21 miRNA. The procedure is pictorially summarized in Figure 5.1. In brief, each well of a 12-well plate was inoculated with 200,000 ZR-75-1 breast cancer cells (American Type Culture Collection) in 2 mL of RPMI with 10% fetal bovine serum and incubated for 3 days. Prior to insonifying a well: (1) the growth medium was aspirated, (2) the well was washed with PBS, (3) 1 mL of the growth medium with or without lipid-stabilized microbubbles (4×10^7 bubbles/mL) was added to the well, (4) the plate was gently mixed for 10-15 seconds, and (5) a 480 μL pre-ultrasound sample was taken. The 12-well plate was then half-immersed in a 37°C water bath directly above a 1 MHz, unfocused ultrasound transducer (SP100 Sonoporator, Sonidel Limited, Raheny Dublin, Ireland). Acoustic parameters ranged from 0.1 to 5 W/cm^2 (spatial-average, temporal peak (SATP) intensity), 25-50% duty cycle, and 1 to 30 minutes of exposure. The transducer was constantly moved in a raster pattern during sonicating to interrogate all the cells. After sonication and 10-15 seconds of mixing, a 480 μL post-ultrasound sample was taken. The samples were centrifuged at 16,000 x g and 450 μL of the supernatant was transferred to a new vial which was flash frozen in liquid nitrogen and stored in a -80°C freezer until later processing. Each experimental setting was conducted at least three times.

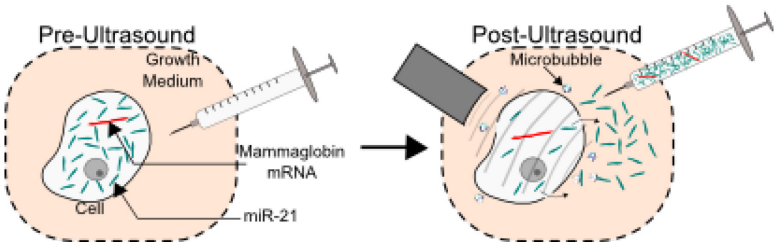

Figure 5.1 Diagram of the ultrasound-aided biomarker liberation processes. Pre- and post-ultrasound medium samples are taken and compared [30].

The acoustic intensity calibration for the SP100 ultrasound system was verified by submerging a hydrophone (HNP-400, Onda, Sunnyvale, California) and the SP100 system in a water tank and recording the detected pressures. References to the acoustic intensity throughout this chapter refer to the system settings. The acoustic intensity at the cell layer within the well was also determined by placing the tip of the hydrophone into ~500 μL PBS in the 12-well plate and exposing the well to ultrasound. The hydrophone was moved in a raster pattern to obtain 2D pressure profiles within the well under various conditions.

5.2.3 Cell Viability

After the biomarker liberation experiment, PBS and trypsin were used to collect all cells from each well. The centrifuged post-ultrasound vial was washed with PBS to collect any cells that detached during the experiment. Cell viability was assessed with trypan blue staining and a hemocytometer after an hour to allow the resealing of pores formed during sonication as many groups have reported that small pore resealing occurs within a few minutes [215, 216]. Larger pores may not have resealed in this time [217] and may allow trypan blue to stain the cells; these cells are considered dead in our analysis.

5.2.4 miR-21 Biomarker Liberation due to Cell Death

Cell incubation with hydrogen peroxide (H_2O_2) was performed to induce cell death and quantify the number of copies of miR-21 released due to cell death. The ZR-75-1 cells (cultured and plated in 12-well plates as described above) were incubated with H_2O_2 for 30 minutes (the maximum length of the ultrasound experiments) at concentrations varying from 10 μM to 500 mM. Samples of the medium were collected and analysed for cell death and biomarker liberation as presented above.

Ideally it would be preferred to have some chemical treatment which would kill cells but not lyse them and not affect RNA levels as a control treatment to compare to ultrasound treatments. Unfortunately, many chemical treatments may affect RNA expression levels. Our approach was to use H_2O_2 (which is shown to induce apoptosis) as a chemical treatment and correct for the alteration in RNA expression levels using a correction factor. To account for the effects of H_2O_2 either on miR-21 expression in cells or on miR-21 itself, ZR-75-1 cells incubated with or without H_2O_2 were lysed (using Qiazol as part of the RNA purification kit protocol) and RNA levels were compared. Using this data, a correction factor (miR-21 from Qiazol-lysed cells incubated with H_2O_2 divided by miR-21 from lysed cells incubated without H_2O_2) is obtained and applied to the H_2O_2 release data in all figures. This correction factor is meant to account for reduction in RNA levels associated with H_2O_2, while still having some means to compare RNA release from ultrasound treatment.

It could be argued that H_2O_2 treatment is a biased control because it does not bring about mechanical stresses and could instead induce changes in miRNA expression. For this reason, we accounted for mRNA expression level changes due to H_2O_2 and also included mechanical lysing as

an alternate control. For mechanical lysis, we used a Pro300A Homogenizer (Pro Scientific, 8 bursts of ~20 seconds at 18,000 RPM) to mechanically lyse cells. Trypan blue staining confirmed that > 95% of cells were dead.

5.2.5 Biomarker Quantification

Absolute quantification of the miR-21 miRNA was completed using a standard qPCR and TaqMan probes and primers. First, total RNA was purified into a 30 μL eluate using a total RNA purification kit (miRNeasy Mini Kit, Qiagen, Mississauga, ON, Canada). Second, miR-21 was reverse transcribed by using TaqMan® MicroRNA Reverse Transcription Kit (Applied Biosystems, Burlington, ON, Canada). Third, TaqMan probes and primers specific for miR-21 were combined with the miR-21 complimentary deoxyribonucleic acid (DNA), TaqMan® Universal Master Mix II (Applied Biosystems, Burlington, ON, Canada) and analysed using the 7900HT Fast Real-Time PCR System (Applied Biosystems, Burlington, ON, Canada). Standard curves were created for miR-21 by creating a known concentration of RNA primers (GenScript, Piscataway, NJ, USA) with the miR-21 nucleotide sequence. This standard curve is used in analysis to determine the number of miR-21 copies present in the reverse transcribed solution. To account for the dilutions in the analysis, a correction factor of 7.45 is used to determine the number of copies in the original 500 μL pre- and post-ultrasound samples. One-way and two-way analysis of variance (ANOVA) and Tukey honest significant difference (HSD) were used to determine statistical significance.

5.3 Results and Discussion

Although miR-21 was found naturally in the growth medium, the subtraction of the pre-ultrasound sample from the post-ultrasound sample accounts for ultrasound-aided release relative to the baseline. Control experiments were conducted to account for the natural release of miR-21 over the length of the experiment. After 30 minutes (the maximum length of our sonication experiments) there were $6 \times 10^6 \pm 2 \times 10^6$ miR-21 copies released per 100,000 cells. The natural release of miR-21 was 1-2 orders of magnitude less than the amount released by ultrasound and microbubbles.

Figure 5.2 shows a two-dimensional raster scan of the pressure profile within a 12-well plate while the SP100 ultrasound system delivered 2 W/cm^2 (SATP (spatial average, temporal peak) averaged over the transducer aperture) at 50% duty cycle. The measured spatial peak, temporal peak (SPTP) intensity was 12.1 W/cm^2 with a full-width half-maximum (FWHM) of ~3.5 mm. Averaging

over the entire effective radiating area, we found the SATP intensities in the well were ~2.95 W, nearly a 50% increase in intensity compared to the reported value. These results are consistent with results from Kinoshita and Hynynen [218] and Hensel *et al.* [219] who found intensities can vary by a factor of four due to the formation of standing waves in the well. Variations in the volume of liquid in the well, slight streaming effects, and transducer motion constantly changed the location of standing wave nodes and cause a large variation of the measured intensities. The hydrophone measured a symmetric acoustic pressure wave allowing for the determination of the peak negative pressure (PNP) and mechanical index (MI) – crucial values for cavitation. PNP is determined by $(2\rho_0 c_0 I)^{1/2}$, where ρ_0 and c_0 is the density and speed of sound in the liquid, respectively, and I is the intensity. MI is calculated as $PNP/f^{1/2}$ where f is the frequency of the ultrasound in MHz. Reported intensities of 0.1, 0.3, 0.5, 1, 3, and 5 W/cm^2 thus correspond to PNPs of 0.05, 0.09, 0.12, 0.17, 0.30, 0.39 MPa_{PNP} and MIs of 0.05, 0.09, 0.12, 0.17, 0.30, 0.39, respectively. All intensities on the figures refer to the SP100 system settings; however, hydrophone measurements reveal that the intensity within the well could be 1-4 fold greater, consistent with Kinoshita and Hynynen [218] and Hensel *et al.* [219].

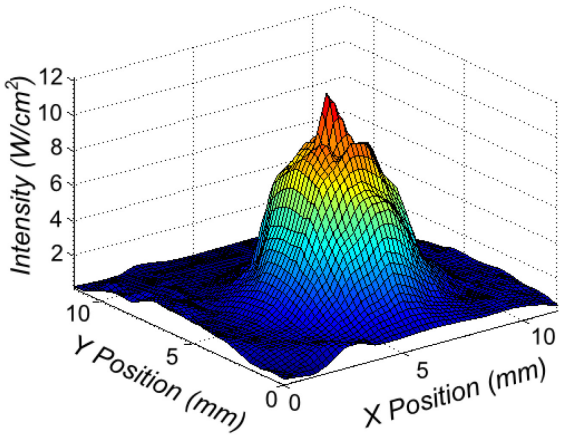

Figure 5.2 Pressure profile of a 1 MHz unfocused transducer within a well of a 12-well plate. The SP100 system lists the intensity at 2 W/cm^2 [30].

Microbubble cavitation was confirmed through microscopy and hydrophone measurements. Using a 20-cycle burst of 1 MHz ultrasound we found that the intensity required to destroy over 95% of the bubbles was over 14.8 W/cm^2. However, with enough cycles even the lowest intensity ultrasound used in this paper (0.1 W/cm^2) was able to destroy the microbubbles.

The results of the H_2O_2 studies are presented in Figure 5.3. Figure 5.3A shows the cytotoxicity and was used to find appropriate H_2O_2 concentrations to determine the cell death equivalent biomarker released used in Figure 5.4, Figure 5.5, and Figure 5.6. Figure 5.3B shows the biomarker liberation due to incubation with the H_2O_2. Although the mechanisms of biomarker liberation due to ultrasound-microbubble exposure and H_2O_2 incubation are not necessarily identical, these experiments give a good idea as to the contribution cell death has on the amount of biomarkers liberated. As a constant source of chemical, oxidative stress high levels of H_2O_2 have previously been shown to dysregulate the expression of genes [220] and can potentially damage DNA [221]. This is believed to be a dominant mechanism of cell necrosis. We used H_2O_2 treatment as a chemical means of inducing cell death in contrast to the mechanical mechanisms believed to operate in ultrasound-microbubble interactions. H_2O_2 chemical stresses can also affect miRNA expression and indeed we observe that H_2O_2 treatment reduces miR-21 levels. This effect is accounted for by comparing gene expression of lysed cells incubated with and without H_2O_2. Comparing miR-21 expression in Qiazol-lysed cells incubated with or without H_2O_2 showed that the cells incubated with H_2O_2 expressed ~1.8 ± 0.2 fold less than cells incubated without H_2O_2. A correction factor was applied to the H_2O_2 data shown in the figures to account for this expression difference. It should be noted that the mechanism of H_2O_2 on biomarker release is unclear and could be a topic of further research.

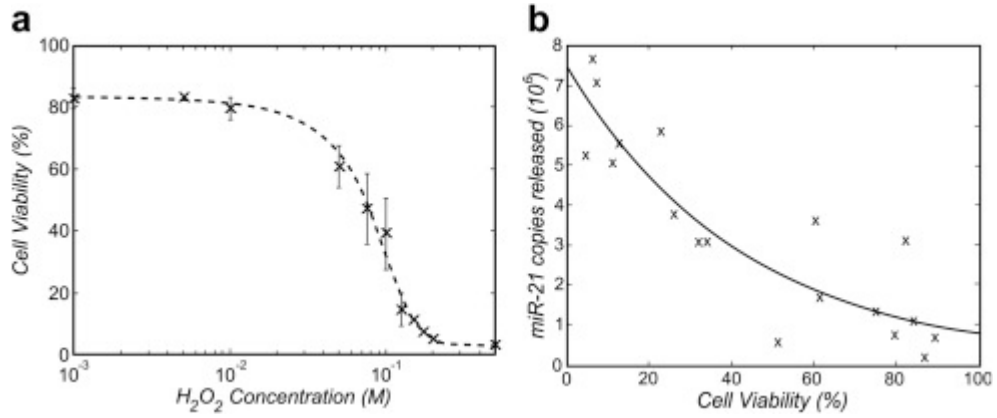

Figure 5.3 Cell viability and miR-21 release due to H_2O_2 exposure. Hydrogen peroxide induced cell death (a) and miR-21 liberation due to hydrogen peroxide incubation (b) [30].

In addition to the use of H_2O_2 to chemically lysed cells as a control treatment, we also considered mechanical lysing treatments as an alternate control. The miR-21 biomarker concentration from mechanically lysed cells (via homogenizer) was 2.6 ± 0.3-fold less than the cells lysed with the

purification kit and 1.4-fold less than H_2O_2 treatments. This mechanical lysing data was counter-intuitive to us as we expected mechanical lysing to release cell contents and present total RNA levels. It is likely that exosomes, micro-vesicles, and cell fragments created or released during the homogenization procedure and containing RNA were removed during the centrifugation step common to all post-treatment protocols. As a reference for comparison for Figure 5.4, Figure 5.5, and Figure 5.6, a maximum of 4.2×10^8 copies per 100,000 cells could be liberated as determined by complete mechanical lysis of the cells using a homogenizer and is indicated on Figure 5.4, Figure 5.5, and Figure 5.6 by a solid black line.

The effect of duty cycle on miR-21 liberation with and without microbubbles was examined by applying 1 MHz, 2 W/cm^2 ultrasound for 1 minute (Figure 5.4). Without microbubbles cell viability was measured at 92.1 ± 2.0 and 89.5 ± 1.0% while with microbubbles cell viability was measured at 70.2 ± 6.5 and 69.9 ± 2.2% at 25% and 50% duty cycle, respectively. The cell death equivalent biomarker liberation shown in Figure 5.3 shows that only a small portion of biomarker liberation is released due to cell death. Two-way ANOVA shows that both microbubbles ($p < 0.001$) and duty cycle ($p < 0.05$) have a statistically significant effect on biomarker liberation with no significant interaction between the two variables. As in previous work [28, 29], high duty cycle is a crucial factor when working with ultrasound alone ($p < 0.05$); however, the addition of microbubbles allows even low duty cycle ultrasound to exceed the miR-21 liberation at high duty cycle ultrasound without microbubbles. Microbubbles increase biomarker miR-21 liberation by 6.4 and 2.6-fold at 25% and 50% duty cycles, respectively, compared to ultrasound alone ($p < 0.05$). The effect of increasing duty cycle from 25% to 50% is reduced when microbubbles are present only providing a 1.4-fold increase in copies, while a 5-fold increase is seen with ultrasound alone. Previous publication [28, 29] indicated that protein and mRNA biomarkers require high duty cycle to sufficiently release biomarkers – CEA liberation wasn't achieved even at acoustic intensities of 6 W/cm^2 at 20% [28]. However, this data shows that it may be possible to examine an array of important miRNA at clinically-used lower duty cycles and intensities.

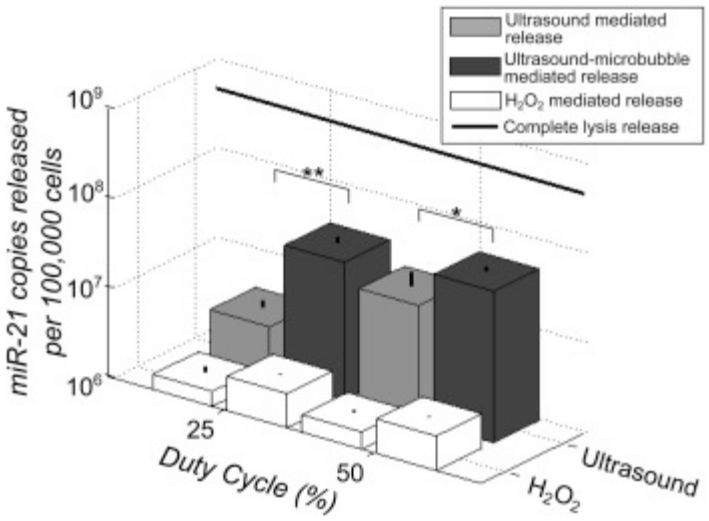

Figure 5.4 Effects on ultrasound duty cycle and microbubbles on miR-21 liberation. Biomarker release from ZR-75-1 cells exposed to either a 1 MHz, 2 W/cm^2 unfocused ultrasound transducer for 1 minute with or without microbubbles (dark gray and light gray bars, respectively) or exposed to H_2O_2 without ultrasound. White bars represent release due to H_2O_2 exposure at similar cell viabilities as corresponding ultrasound experiments (cell death equivalent biomarker release). The solid black line represents the maximum possible biomarkers. Asterisks (*) represent statistical significance as determined by two-way ANOVA and Tukey HSD analysis. Both microbubbles ($p < 0.001$) and duty cycle ($p < 0.05$) have statistical significance without statistical interaction ($p \approx 0.92$). Note: H_2O_2 treated cells were not exposed to ultrasound [30].

Using microbubbles may be an important factor to reduce the required duty cycle and may lead to current clinical ultrasound systems being capable of releasing biomarkers into the blood. Furthermore, tissue damage is a concern that would be mitigated by reducing the duty cycle and intensity. Since microbubbles reduce both the duty cycle (Figure 5.4) and the intensity (Figure 5.5) required, ultrasound-aided biomarker release may show promise at clinical diagnostic limits for ultrasound exposure. Alternatively, novel ultrasound systems could be designed to handle high duty cycle biomarker liberation. As suggested in the introduction, microbubbles give high contrast, in fact single microbubble sensitivity [21], in ultrasound imaging, hence, an ultrasound system could be dual-purposed for low duty cycle imaging and high duty cycle biomarker release.

Although no substantial increase is seen at 50% duty cycle compared with 25% duty cycle when microbubbles are present all future experiments are conducted at 50% duty cycle to be consistent with other protocols. Slightly lower, but still significant ($p < 0.05$), number of miR-21 miRNA copies are expected at 25% duty cycle with microbubbles and may be used if heating and power

delivered to the tissue becomes an issue. Higher duty cycles and continuous ultrasound was not examined as transducer and tissue overheating and power delivery were concerns.

Figure 5.5 shows how miR-21 release is substantially increased with microbubbles and moderate intensity. Cells were sonicated for 10 minutes at 50% duty cycle at varying acoustic intensities. Without microbubbles, cell viability was measured at 86.8 ± 3.3, 85.8 ± 1.6, 84.1 ± 1.5, 82.3 ± 3, 81.0 ± 0.7, and 74.8 ± 2.64% at 0.1, 0.3, 0.5, 1.0, 3.0, and 5.0 W/cm^2, respectively. With microbubbles, cell viability was measured at 79.0 ± 3.6, 80.8 ± 1.0, 79.5 ± 2.4, 76.6 ± 0.5, 68.4 ± 0.7, and 62.3 ± 3.2% at 0.1, 0.3, 0.5, 1.0, 3.0, and 5.0 W/cm^2 ultrasound intensity, respectively. Results from the H_2O_2 studies show that the contribution of biomarker liberation from cell death is minimal compared to the total amount of miR-21 released due to ultrasound-microbubble exposure. Two-way ANOVA shows that both microbubbles ($p < 0.01$) and acoustic intensity ($p < 0.01$) have statistically significant effects on biomarker liberation. At low acoustic intensities < 1 W/cm^2 the microbubbles produce dramatic increases in miR-21 release ($p < 0.05$), causing nearly an order of magnitude increase in the miR-21 miRNA concentration compared with no microbubbles. However, at high acoustic intensity (5 W/cm^2) both ultrasound alone and with microbubbles release a high concentration of miR-21 into the surrounding medium causing only 1.2-fold increase in the miR-21 miRNA concentrations compared to ultrasound alone. The most substantial increase in copy count due to microbubbles is seen at 3 W/cm^2 where over 25 million miR-21 molecules are released per 100,000 cells. The results follow the same trend as the mammaglobin mRNA [29], however, the copies released are three orders of magnitude greater for miR-21 (Figure 5.7A).

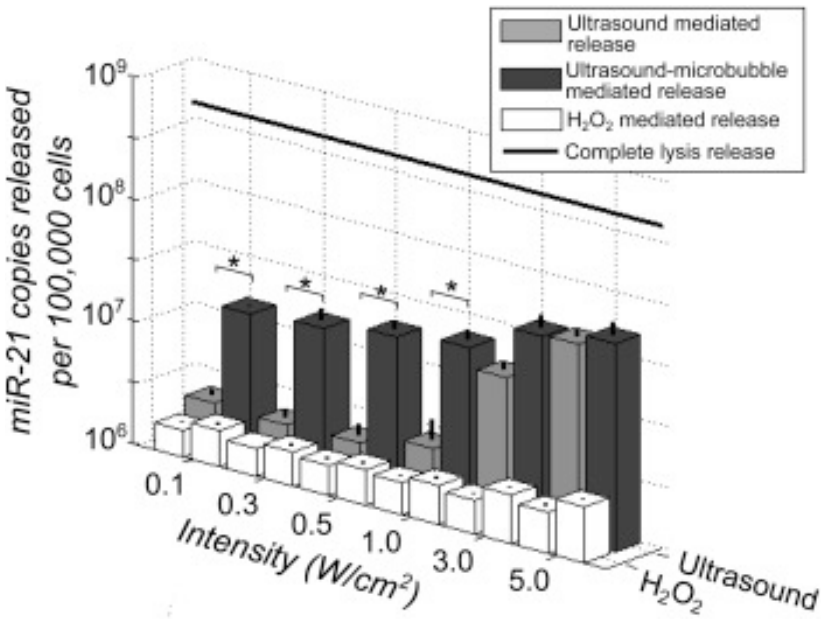

Figure 5.5 Effects of ultrasound intensity and microbubbles on miR-21 liberation. Biomarker release from ZR-75-1 cells exposed to either a 1 MHz, 50% duty cycle unfocused ultrasound transducer for 10 minutes with or without microbubbles (dark gray and light gray bars, respectively) or exposed to H_2O_2 without ultrasound. White bars represent release due to H_2O_2 exposure at similar cell viabilities as corresponding ultrasound experiments (cell death equivalent biomarker release). The solid black line represents the maximum possible biomarkers. Asterisks (*) represent statistical significance as determined by two-way ANOVA and Tukey HSD analysis. Both microbubbles and intensity have statistical significance ($p < 0.01$) without statistical interaction ($p \approx 0.44$). Note: H_2O_2 treated cells were not exposed to ultrasound [30].

Figure 5.5 shows that acoustic intensity is an important factor for biomarker liberation ($p < 0.05$). With and without microbubbles, the biomarker release substantially increases after 1 W/cm^2 and by 5 W/cm^2 the biomarker liberation without microbubbles is nearly identical to the with microbubble scenario. The substantial increase after 1 W/cm^2 may be due to the acoustic intensity being great enough to induce cavitation without immediate microbubble destruction, while the minute differences at 5 W/cm^2 are most likely due to inertial cavitation of the microbubbles early in the ultrasound therapy limiting microbubble-cell interaction duration. Although the large biomarker liberation at 5 W/cm^2 is ideal, our results indicate that cell death starts to increase drastically after 1 W/cm^2. At low acoustic intensities ≤ 1 W/cm^2 there is a substantial difference between non-microbubble and microbubble experiments ($p < 0.05$). This is most likely due to microbubbles undergoing stable cavitation instead of inertial cavitation and therefore remaining in the growth media throughout the entire experiment. Furthermore, the continual presence of microbubbles throughout the experiment at low intensities may cause microstreaming effects

that place sheer stress in the cell membrane causing small pores to form [222, 223]. Larger pores can form at high intensity due to microbubble collapse creating microjets and shock waves [217, 224–226]. The larger pores created at high intensity may allow the biomarkers to more easily diffuse out of the cell thus giving rise to higher biomarker liberation.

Figure 5.6 shows that miR-21 concentrations peak at 5 minutes; however, unlike mammaglobin mRNA which decreased by over 45% over 30 minutes, miR-21 remains relatively constant for 30 minutes in the growth medium only decreasing by 7% (not statistically significant $p > 0.05$). This difference may be due to miRNA being more stable than mRNA outside of cells. Without microbubbles, the miR-21 concentration slowly rises and plateaus within 5 minutes. However, with microbubbles there is a statistically significant ($p < 0.01$) increase in miR-21 concentration (18-25 fold increase compared with no microbubbles). Although the reason for the decrease in concentration is unknown, the early peak in miR-21 concentration is desirable for *in vivo* experiments. Furthermore, Figure 5.6 demonstrates the high stability of miR-21 which make miRNA more desirable than mammaglobin mRNA for lengthy procedures. Without microbubbles cell viability was determined as 89.5 ± 1.0, 90.9 ± 3.4, 84.9 ± 5.5, and 82.2 ± 0.8% at 1, 5, 20, and 30 minutes of ultrasound exposure, respectively. With microbubbles cell viability was determined as 69.9 ± 2.2, 67.3 ± 7.9, 66.8 ± 4.1, and 61.8 ± 3.4% at 1, 5, 20, and 30 minutes of ultrasound exposure, respectively.

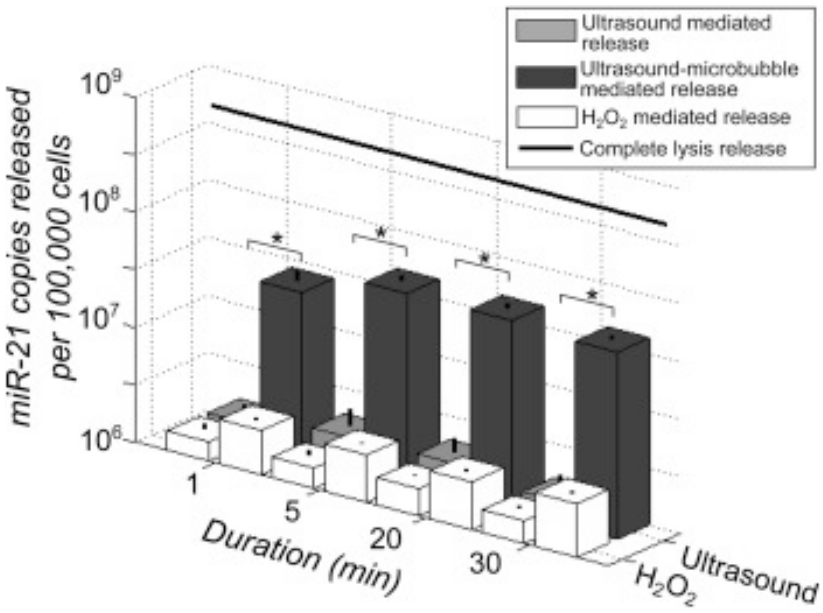

Figure 5.6 Effects of ultrasound exposure duration and microbubbles on miR-21 liberation. Biomarker release from ZR-75-1 cells exposed to either a 1 MHz, 2 W/cm^2 (50% duty cycle) unfocused ultrasound transducer with or without microbubbles (dark gray and light gray bars, respectively) or exposed to H_2O_2 without ultrasound. White bars represent release due to H_2O_2 exposure at similar cell viabilities as corresponding ultrasound experiments (cell death equivalent biomarker release). The solid, thick line represents the maximum possible biomarkers. Asterisks (*) represent statistical significance as determined by two-way ANOVA and Tukey HSD analysis. The addition of microbubbles caused statistically significant increase in biomarkers ($p < 0.01$) while duration had less statistical significance ($p \approx 0.05$) with minimal interaction between these parameters ($p \approx 0.069$). Comparing no microbubbles to microbubbles reveals statistical significance ($p < 0.05$). Note: H_2O_2 treated cells were not exposed to ultrasound [30].

Examining miRNAs presents several advantages over other potential biomarkers including proteins and mRNAs. Since many miRNAs regulate the expression of more than one gene, an unusual level of miRNA may be indicative of more than one abnormally expressed gene. Simultaneous profiling of a number of biomarkers could offer improved sensitivity and specificity. As with our previous mRNA study [29], our present study with miRNA uses qPCR and TaqMan probes to quantify the levels of RNA which has high specificity, has over seven orders of magnitude dynamic range, and most importantly for blood biomarkers has near single-copy sensitivity. Overall our *in vitro* results indicated that miRNAs have great potential as biomarkers. Their small size and low molecular weight allow miRNAs to more easily diffuse out of cells compared to mRNA. The number of copies released of miR-21 is orders of magnitude greater than

that of mammaglobin mRNA, Figure 5.7A. Quantifying the number of RNA molecules present in a solution of lysed ZR-75-1 cells resulted in ~82 mammaglobin mRNA copies per cell and ~1,110 miR-21 copies per cell. This implied that only 0.4% and 20.3% of the mammaglobin mRNA and the miR-21 molecules in the cells were released into the growth media, respectively (using data for a 1 MHz unfocused transducer at 1 W/cm^2, 50% duty cycle, and 10 minutes of ultrasound exposure), when microbubbles were present as depicted in Figure 5.7B. This supports our hypothesis that biomarker liberation is related to the size of the molecule in that the smaller molecules (miR-21, 22 bases) inside the cell are more easily liberated than the larger molecules (mammaglobin mRNA, 502 bases). However, it should be noted that mRNA and miRNA are sometimes apart of large biomolecules or structures. More investigation is required to determine if the biomarkers detected in this research corresponds to free RNA molecules.

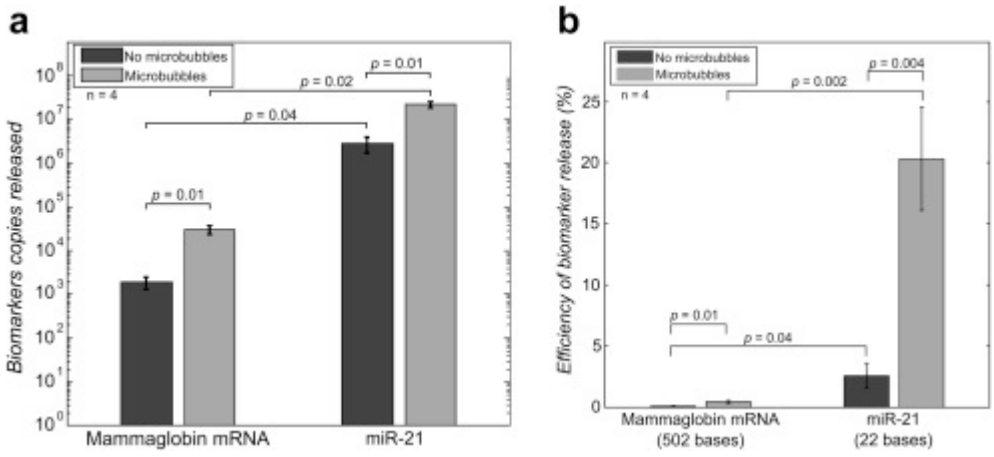

Figure 5.7 Comparison of mammaglobin mRNA and miR-21 liberation. A 1 MHz unfocused transducer to expose ZR-75-1 breast cancer cells to 10 minutes of 1W/cm^2, 50% duty cycle ultrasound was used. A) Copies released on a logarithmic scale. B) Biomarker liberation efficiency. The number of biomarkers per cell was determined and used to estimate the efficiency of biomarker release. Two-way ANOVA shows that both the addition of microbubbles and the type of biomarker are statistically significant ($p < 0.05$) and that there is significant interaction ($p < 0.05$) [30].

Although the concentration of microbubbles used in our *in vitro* studies is not attainable *in vivo*, a continuous IV injection of microbubbles would allow the microbubbles to continuously flow throughout the target tissue, replenishing the microbubbles that burst. This could allow for enhanced biomarker liberation. Targeted microbubbles could also be designed with ligands to bind to the target tissue, causing a buildup of microbubbles and a potentially large biomarker release. Furthermore, primary radiation forces from the ultrasound can act on the microbubbles

in vivo causing microbubble translation, moving the microbubbles closer to the blood vessel walls and the target tissue – potentially increasing the biomarker release and binding efficiency of targeted microbubbles. Given that the total number of cells per well is approximately 800,000 at the time of the experiments, the ratio of bubbles to cells is quite high at 50 to 1. This observation should be tempered with the fact that cells are growing in a monolayer while microbubbles are distributed throughout the volume of the growth medium. Microscopy of the cell monolayers show that there are significantly fewer microbubbles visible compared to cells; however, due to acoustic streaming and mixing effects it is difficult to know the number of microbubbles that interact with each cell.

Microbubbles are advantageous in many aspects; however, several limitations will exist when translating this work into animal models. Microbubbles are intravascular agents and are too big to escape the vasculature. Endothelial cell lining increases the microbubble-tumor cell separation and may reduce the effects of ultrasound-microbubble interaction on the cancerous tissues. Sub-micron microbubbles [101, 227] and phase-change nanodroplets [34, 228] have been developed that can extravasate out the leaky vasculature surrounding tumors providing passive accumulation. Studies should be designed to examine how well these microbubbles and nanodroplets work for biomarker liberation. The potential of nanodroplets for biomarker liberation is briefly discussed in Chapter 6. Analysing miR-21 levels alone does not provide great insight for diagnostic classification and prognostic evaluation; hence, an array of miRNAs must be examined to determine the diagnostic ability of this technique. Future studies should investigate larger arrays of RNA and protein to examine the diagnostic potential of this technique. Preliminary results using the housekeeping rRNA 18S (1869 bp) and the micro-RNA miR-155 (22 bp) verify that this process is not unique to miR-21. Using 1 MHz, 1 W/cm^2, 50% duty cycle ultrasound for 10 minutes, a fold increase of up to 1.24 ± 0.16 and 2.56 ± 0.48 was measured without microbubbles while with microbubbles a fold increase of up to 2.36 ± 0.09 and 6.06 ± 0.12 was measured for 18S and miR-155, respectively. miR-155 was found to be expressed at very low concentrations in the ZR-75-1 cells compared to miR-21; hence, only a small fold increase is seen. Ultrasound-induced release efficiency may depend not only on molecular size, but also on concentration gradients across cell membranes, intracellular packaging of molecules, and other complex effects. Future investigation should assess how concentration gradients and other factors affect biomarker liberation.

There has been much research into how biomarkers are shed into the bloodstream; however, the exact mechanism is not well understood. Extracellular RNAs have been shown to be released as free-circulating molecules, exosomes, micro-vesicles, apoptotic bodies, and ribonucleoproteins [229, 230]. As many papers have demonstrated that ultrasound-microbubble interaction near cells induces sonoporation, we speculate that the primary mechanism of biomarker liberation from cells due to ultrasound and ultrasound-microbubble exposure is sonoporation. However, more investigation is needed to determine the exact mechanisms for biomarker release and is left for future studies.

Overall, miRNAs have great potential as diagnostic markers and this technique may help release biomarkers into the blood allowing for minimally-invasive diagnostics. This ultrasound-enhanced liberation technique applied to miRNAs may aid diagnostic and prognostic medicine since: (1) miRNAs are small, low molecular weight molecules that can diffuse out of cells with over 50 fold higher efficiency than previously investigated mammaglobin mRNA using ultrasound-microbubble exposure, (2) as a model miRNA, miR-21 has been detected with several orders of magnitude increase in copy number compared to background levels making detection and reproducibility promising, and (3) miRNAs are much more stable than mammaglobin mRNA in our previous work.

Our findings demonstrate that miR-21 is released much more efficiently than mammaglobin mRNA and supports the hypothesis that ultrasound-mediated biomarker liberation of smaller molecules is more efficient than larger molecules. Although more investigation is needed to verify this hypothesis for a large library of biomolecules, these data suggest that other smaller molecules that are candidate biomarkers for a range of diseases may offer enhanced diagnostic sensitivity when liberated by ultrasound-microbubble exposure compared with larger molecules, an effect that may be further amplified by microbubbles.

Chapter 6 Ultrasound-Aided Biomarker Liberation – Additional Work

The work presented in Chapters 4 and 5 was conducted with microbubbles as an agent to enhance sonoporation and further increase the concentration of biomarkers in the surrounding media. Although microbubbles have great utility in ultrasound imaging, their large size restricts their movement to the vasculature and limits their utility for targeting and biomarker liberation to tissues that are directly adjacent to the blood vessels. Since the vasculature around some tumors is 'leaky' [33, 96, 97], it would be highly beneficial to use ultrasound imaging and diagnostic agents that could escape the vasculature, passively (through the enhanced permeability and retention (EPR) effect) or actively (through targeting moieties) accumulating around the tissue of interest. One possible solution is to use phase-change nanodroplets. These phase-change nanodroplets are created by pressurizing lipid-stabilized, perfluorocarbon, microbubbles at low temperatures. The combination of high pressure and low temperature causes the perfluorocarbon to phase-change into a liquid state and can reduce the size of the contrast agent to only a few hundred nanometers in diameter [34]. Many of the formulations of these nanodroplets are stable even at physiologically relevant temperatures due to the surface tension causing high Laplacian pressures. Although the liquid form of these contrast agents is not detectable by ultrasound imaging, the nanodroplets can be vaporized into microbubbles by applying a high-intensity ultrasound pulse. The vaporized nanodroplets – *i.e.* microbubbles – can be detected by ultrasound. Similar to microbubbles, phase-change nanodroplets have been investigated for ultrasound-aided drug delivery [38, 231] but had not been studied for release biomarkers from tissues.

We investigated using these phase-change nanodroplets as a potential alternative to the microbubbles for releasing biomarkers. Although not the lead on this work, I worked on many of the experiments, and I helped process and quantify some of the results. This work has been published in *Ultrasound and Medicine and Biology* [31]. To complete the discussion of my contributions to the work on ultrasound-aided biomarker liberation, this work and my

contributions will briefly be discussed. For this work, I helped with preparing the cell cultures and the phase-change nanodroplets, exposing the cells to ultrasound, processing the samples, as well as helping quantify and compare some of the data to the data in my first two publications.

The phase-change nanodroplets were prepared as described in Sheeran *et al.* [34] and is described in Section 7.2.1. In brief, the headspace of a vial containing a lipid stock was replaced with perfluorobutane gas and the vial was sealed and shaken to form microbubbles. The vial was placed in -5°C isopropanol and pressurized by injecting air through the septa of the vial which phase-changed the microbubbles to liquid nanodroplets. Fluorescent microscopy of the microbubbles and the nanodroplets were taken by using a rhodamine-conjugated lipid stock and is presented in Figure 6.1. Cells were prepared in 12-well plates, ultrasound was applied, cell viability was assessed, and the liquid biopsy samples were analyzed as described in Chapters 4 and 5.

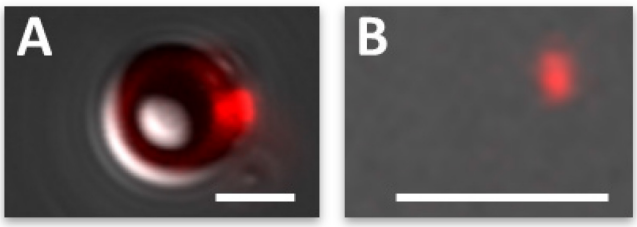

Figure 6.1 Fluorescent microscopy of a microbubble and a nanodroplet. A) Before pressurization, the vial shaken with perfluorobutane and a rhodamine-conjugated lipid stock contains microbubbles. B) After pressurization, the majority of the microbubbles have condensed into nanodroplets which are typically 7-fold smaller than their microbubble counterparts. The red signal is from the rhodamine molecule in the lipid shell of the microbubbles and nanodroplets. The nanodroplet is too small to see or does not have good contrast in the white-light microscope image; however, the rhodamine molecule can easily be seen indicating the location of the nanodroplet. The scalebar represent 2 µm. This image was modified from the poster presented at the *IEEE International Ultrasonic Symposium* that accompanied the conference proceedings by Forbrich *et al.* [35].

Similar to the ultrasound and microbubble-aided biomarker liberation experiments described in Chapters 4 and 5, the nanodroplets were found to have a very similar increase in biomarker concentration in the surrounding medium. However, the cell viability was higher with nanodroplets compared to microbubbles. Since the biomarker liberation with nanodroplets was found to be similar to the biomarker liberation with microbubbles, these agents are good

candidates for diagnostic purposes. Moreover, their small size makes them capable of passively escaping the leaky vasculature surrounding tumors.

Although phase-change nanodroplets show great potential for enhancing ultrasound-aided biomarker liberation, for providing contrast outside of the vasculature after phase-changing, and for targeting tissues outside of the vasculature, they do not provide contrast for ultrasound imaging in the liquid form. It is important to verify their location prior to inducing the phase-change to microbubbles. Moreover, it is important to be able to map the phase-change events such as the vaporization of nanodroplets or the destruction of microbubbles to validate the efficacy of biomarker liberation or drug delivery. Chapter 7 will discuss several methods to visualize the nanodroplets and phase-change events.

Throughout our research into ultrasound-aided biomarker liberation, we also discovered that micro-vesicles are released from cells [32]. These micro-vesicles were found to be released in much higher concentrations than some of the biomarkers. They were also found to contain a lot of genetic information including DNA and RNA. Additionally, the biomarkers in these micro-vesicles were found to be more stable than those found in just blood. This discovery has profound implication for liquid biopsies and biomarkers for many diseases. Many previously unusable or new biomarkers may be useful for diagnosing, classifying, or assessing the prognosis of diseases.

Although much research is still required, microbubble and nanodroplet-enhanced ultrasound-aided biomarker and micro-vesicles liberation may have a profound impact in diagnostic and prognostic medicine by allowing the characterization of diseases non-invasively without the need for a solid biopsy. Further studies should investigate panels of biomarkers to enhance specificity, accuracy, and aid in genetic profiling of the tissue. Additional animal experiments should also be done to determine the viability of these techniques for *in vivo* and translational research. To that end, future studies should examine the utility of clinically-approved microbubbles and clinical ultrasound systems for biomarker liberation. This would help translation into the clinic where both microbubbles and diagnostic ultrasound systems are widely used and clinically approved.

Chapter 7 Real-time Flash-Difference Ultrasound Imaging of Phase-Change Perfluorocarbon Nanodroplet Activation

As discussed in the previous chapters, ultrasound contrast agents such as microbubbles and phase-change nanodroplets can release biomarkers from nearby tissues and have been investigated for delivering therapeutic drugs to target tissues. For both of these applications, it is critical to be able to visualize the contrast agents and monitor phase-change events and microbubble destruction events to assess the efficacy of biomarker liberation and drug delivery. For the former criteria, microbubbles are advantageous compared to nanodroplets as the microbubbles provide high contrast in ultrasound imaging while the liquid form of the nanodroplets are invisible to ultrasound imaging. For the latter criteria, ultrasound imaging sequences have typically been too slow to reliably capture microbubble destruction and nanodroplet vaporization phase-change events. Moreover, motion artifacts such as the microbubbles flowing through blood vessels make it difficult to differentiate phase-change artifacts from other movement.

To monitor phase-change events, the first part of this chapter is dedicated to a high frame rate ultrasound image sequence capable of suppressing background signals while detecting the phase-change events, such as nanodroplet vaporization. This work has been published and taken with permission from A. Forbrich, T. Harrison, R. Paproski, and R. Zemp “Realtime Flash-Difference Ultrasound Imaging of Phase-Change Perfluorocarbon Nanodroplet Activation” published in *IEEE International Ultrasonics Symposium* [35]. To visualize nanodroplets, a different formulation is briefly discussed at the end of the chapter and my contributions to this work is presented. This work can be found in the article by R. Paproski, A. Forbrich, E. Huynh, J. Chen, J. Lewis, G. Zheng and R. Zemp, “Porphyrin Nanodroplets: Sub-micrometer Ultrasound and Photoacoustic Contrast Imaging Agents” published in *Small* [39].

7.1 Introduction

Ultrasound imaging is a real-time, reliable, and easy-to-use imaging technique which has proven invaluable in clinical medicine. Constant advancements are being made, improving image processing and resolution for more accurate detection and diagnoses of abnormalities. Ultrasound contrast agents such as lipid or albumin-stabilized microbubbles provide several advantages in ultrasound imaging. First, microbubbles have been shown to be detectable with single bubble sensitivity using ultrasound systems [21]. Second, microbubbles can be designed to contain and deliver drugs to specific tissues limiting the effect of the therapeutic on normal or untargeted tissues [232]. Furthermore, many groups have designed targeted microbubbles that allow delivery of therapeutic drugs to target tissues [233, 234]. Finally, microbubbles have been proven to reduce the cavitation energy necessary for sonoporation (transient cellular membrane permeabilization) aiding ultrasound gene transfection both *in vitro* and *in vivo* [180, 183, 232–234].

Although microbubbles are a decent contrast agent for ultrasound imaging with great potential in many areas, their micron-size limits distribution and accumulation through vasculature. Targeted microbubbles may not be able to reach the target tissue because of the endothelial layers of the blood vessel. Many cancers have leaky vasculature around tumor sites which allows extravasation of small sub-micron particles; however, microbubbles cannot leak out.

Recently, a new generation of ultrasound contrast agents have been developed known as phase-change nanodroplets, creating a two-stage contrast agent. Initially, the nanodroplets are sub-micron sized particles which can extravasate out of the vasculature and are stable in physiological conditions. However, when energy is added to the nanodroplets they activate and undergo a phase-change event into microbubbles (Figure 7.1). Phase-change nanodroplets have been designed to be triggered by acoustic energy [34] and electromagnetic fields such as with laser light [228]. Many groups are working on incorporating therapeutics and targeting ligands on nanodroplets to enhance drug delivery, gene transfection, and imaging [38, 235]. Nanodroplets are proving to be a promising advancement in ultrasound imaging having all the benefits of microbubbles, as well as the ability to escape the vasculature and be activated.

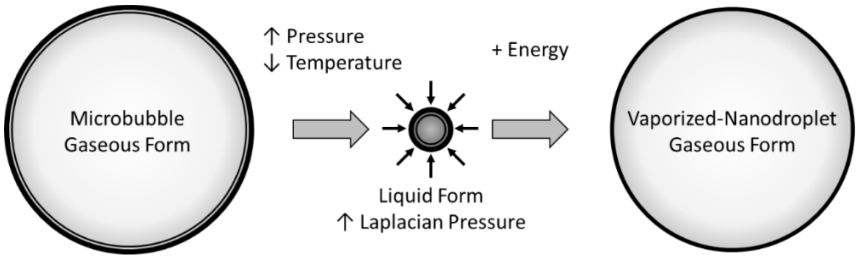

Figure 7.1 Microbubble and nanodroplet formation and activation. Lipid-stabilized microbubbles are created by shaking lipid-stock solutions and perfluorocarbon gases. Phase-change nanodroplets can be formed by increasing the pressure and decreasing the temperature. This causes the gas compression and phase-change to a liquid. The small diameter of the nanodroplets results in very high Laplacian pressures that make it stable at physiologically-relevant temperatures. Finally, by adding acoustic energy the nanodroplets can phase-change back into microbubbles to provide acoustic contrast.

Many imaging techniques have been developed to enhance contrast from microbubbles. Pulse inversion uses two pulses (one with positive initial pressure wave and one inverted with negative initial pressure wave) and the nonlinear properties of microbubbles to eliminate the constant background signals, while enhancing the nonlinear microbubble signals (Figure 7.2). Harmonic imaging examines the higher order frequency bands that are generated from the nonlinear properties and oscillations of microbubbles interacting with the acoustic pressure wave. These imaging techniques are limited for *in vivo* applications due to blood flow causing motion artifacts and, for the pulse inversion technique, require precise waveform generation or knowledge to accurately process the images.

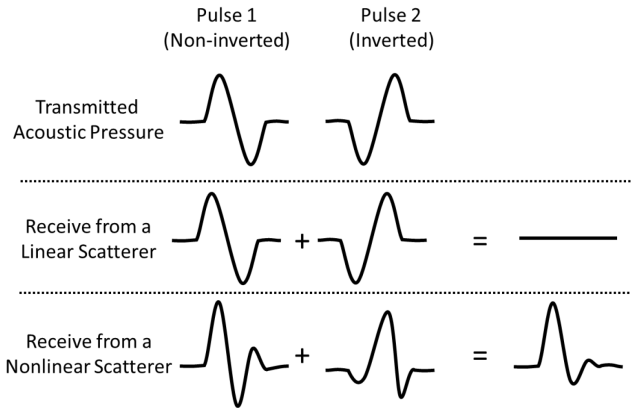

Figure 7.2 Pulse inversion image sequence. Two pulses are transmitted by the transducer, the first with positive initial pressure and the second with negative initial pressure. The detected signal from linear scatterers (background signals, some tissues, etc.) will be symmetric and the summation of the detected signals from each pulse will nullify the signal. However, the detected signals from nonlinear scatterers (microbubbles, fatty tissues, etc.) will be asymmetric and the summation will not nullify the signal.

For nanodroplets, a new imaging technique is needed to detect phase-change events which could help assess and verify the efficacy of drug delivery and gene transfection *in vitro* and *in vivo*. We demonstrate a novel imaging technique called flash-difference imaging to overcome many of the challenges of imaging ultrasound contrast agents which can handle moderate flow rates and low concentrations of contrast agents. Using new, high-speed Verasonics ultrasound systems, which perform software beamforming to dramatically increase the flexibility and the frame rate (> 1,000 frames per second) of ultrasound systems, we can detect phase-change events in real-time including nanodroplet vaporization and microbubble destruction. Flash-difference imaging could have many powerful applications in drug delivery, gene transfection, and biomarker liberation using both microbubbles and nanodroplets, as well as *in vivo* evaluation of the efficacy of ultrasound contrast agent for therapeutic applications.

7.2 Methodology

7.2.1 Nanodroplet Preparation

Lipid-stabilized nanodroplets were created following a similar procedure as outline in Chen *et al.* [180]. In brief, dipalmitoyl-phosphatidylcholine (DPPC), 1,2-dipalmitoyl-sn-glycero-3-phosphatidylethanolamine-polyethyleneglycol-2000 (DPPE-PEG-2000), and 1,2-dipalmitoyl-3-trimethylammonium propane (chloride salt; TAP) were purchased from Avanti Polar Lipids. A lipid stock solution was created by dissolving 1.95 mg/mL DPPC, 0.15 mg/mL DPPE-PEG-2000, and 0.9 mg/mL TAP in a solution of 15% propylene glycol, 5% glycerol, and 80% saline. A 2 mL septum capped vial was filled with 1.5 mL lipid stock solution and the headspace was replaced with decafluorobutane gas. The vial was vigorously shaken for 45 seconds using a Vialmix shaker (Bristol-Myers-Squibb) to form lipid-stabilized microbubbles. Nanodroplets were created by immersing the vial in a -5°C isopropanol bath and applying ~600 kPa of pressure on the sample using a 30 G needle inserted into the septum of the vial to add air. Both lipid-stabilized microbubbles and nanodroplets were used in subsequent experiments. The size distribution of the nanodroplets were characterized using a zetasizer (Malvern). The average nanodroplet size was 185 ± 39 nm as described in Paproski et al. [39].

7.2.2 Microscopy

Microscopy was used to confirm that high-intensity ultrasound was capable of inducing phase-change events in the nanodroplets. Approximately 10 mL of diluted nanodroplets were injected

into an OptiCell (Thermo Scientific). The OptiCell and a high-intensity focused ultrasound (HIFU) transducer were immersed in a water bath above a microscope objective lens on an inverted microscope. Images were taken before and after application of ultrasound.

7.2.3 Experimental Setup

Figure 7.3 depicts the experimental setup for imaging the tube phantoms. A high-intensity focused ultrasound (HIFU) transducer (VHP100-1, Ultran Group) was used to activate nanodroplets flowing through tubes and an ATL L12-5 linear array transducer (Verasonics Inc.), controlled by a 192-transmit/64-receive channel Verasonics Ultrasound System, was used to image the tubes. The HIFU transducer was positioned perpendicular to the array transducer such that the focus was ~2 cm below the center of the array transducer. A hydrophone (HNP-0400, Onda) was used to determine the output intensity of the HIFU transducer and verify the alignment of the HIFU and array transducers. The HIFU transducer was connected to a power amplifier (2100L, Electronics & Innovation Ltd.), which was connected to a function generator (AFG3021B, Tektronix) to vary the intensity and the number of cycles. For synchronization, the Trigger In on the function generator was connect to the Trigger Out on the Verasonics ultrasound system.

Phantoms were constructed with a ~4 mm tube embedded 2 cm deep in tissue mimicking gel (10% cornstarch w/v, 10% porcine gelatin w/v dissolved in water) and positioned such that the focus of the HIFU transducer was on the tubes. Blood mimicking fluid (BMF, 5% cornstarch w/v dissolved in water) mixed with or without microbubbles or nanodroplets (<2% nanodroplet solution) was forced through the tube at a constant rate using a syringe pump (NE-300, New Era Pump Systems Inc.). To make sure that each tube received that same intensity of ultrasound, the experiments were also repeated with only a single tube and the HFIU transducer position with the focus on that tube.

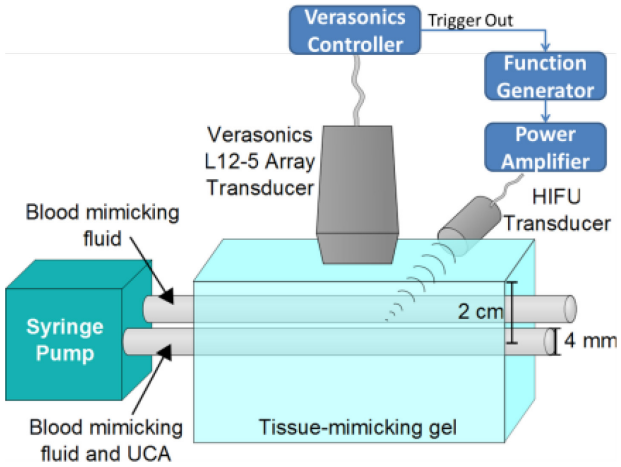

Figure 7.3 Experimental setup to monitor phase-change events. An ATL L12-5 array transducer was positioned overtop two tubes that had either blood-mimicking fluid with or without ultrasound contrast agents (UCA). A HIFU transducer was coaligned along the lateral axis of the array transducer. The focus of the HIFU transducer was positioned on the tubes [35].

7.2.4 Pulse Sequence

Either a single plane-wave (flash) image or a sequence of non-inverted and inverted plane-wave images at five different angles was taken using the linear array transducer and beamformed to form the images before and after a phase-changed pulse from the HIFU transducer. After the first image sequence, the Verasonics ultrasound system triggered the function generator and a high-intensity activation pulse was applied to the tube. To avoid reverberation artifacts from the activation pulse, a 20 ms delay was applied before acquiring the second image sequence. Flash-difference images were created by subtracting the pre-images from the post-images resulting in images that had either positive signals representing nanodroplets activation or negative signals representing microbubble destruction.

7.3 Results

The diameter of the lipid-stabilized nanodroplets was determined to range from 230-800 nm with an average diameter of ~530 nm. Since the Laplacian pressure exerted on the exterior of the nanodroplets is quite high, many of the nanodroplets were stable at room temperature; however, as the pressure is inversely proportional to the radius of the bubbles, some of the larger bubbles (under less pressure) naturally phase-changed over several hours. To mitigate this natural phase-change process, the nanodroplets were used within one hour of creation. Moreover, the vial of nanodroplets was kept in ice to prevent the expansion of the nanodroplets.

Microscopy images confirmed that intense ultrasound was able to induce phase-change events in the nanodroplets. Nanodroplets were injected into a Opticell cell culture cassette and, since nanodroplets and microbubbles may be expected to float, the microscope was focused on the upper surface of the container. Figure 7.4A shows a condensed nanodroplet sample prior to applying high intensity ultrasound. Figure 7.4B shows the activated nanodroplets after applying 10 cycles of 1.7 MI ultrasound. A 5-fold expansion in the nanodroplet diameter is observed after activation, which is consistent to the expansion of the liquid to gaseous decafluorobutane.

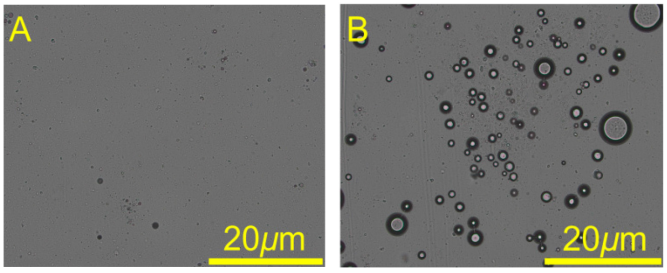

Figure 7.4 Nanodroplet activation imaged using an inverted microscopy. A) Image prior to ultrasound activation of the nanodroplets. B) Image after applying 10 cycles of 1.7 MI focused ultrasound to the nanodroplets [35].

Our pulse sequence and image processing techniques were initially confirmed with blood mimicking fluid with and without nanodroplets in thin latex (nearly acoustically transparent) membranes in water. The HIFU, array transducer, and latex membranes were positioned as described above. Figure 7.5 demonstrates the resulting flash-difference phase-change image created using our algorithm. Nanodroplet phase-change events were clearly evident only in the blood mimicking fluid with nanodroplets.

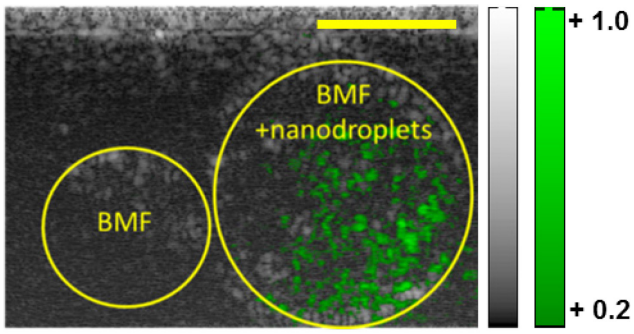

Figure 7.5 Flash-difference images of nanodroplets in between a latex membrane. The latex membranes were filled with blood-mimicking fluid (BMF) with (right) or without (left) nanodroplets. Yellow scalebar represents 5 mm. The gray and green colormap represents ultrasound signal before the HIFU pulse and the percent change in ultrasound signal after the HIFU burst, respectively [35].

Phantom experiments were conducted by varying a wide range of parameters including the flow rate (0-20 mL/s), the intensity (0.5-2.4 MI), and the number of cycles (10-1000 cycles). Figure 7.6 depicts several images obtained from these experiments that did not use pulse inversion or multiple angle imaging. Flow rate higher than 8 mL/min and intensities above 2.4 MI began to give both positive and negative signal changes from both tubes indicating that the image sequence was not suitable for these flow rates. At these flow rates the resulting images have a mixture or red (signal decrease) and green (signal increase) in both tubes. As shown in Figure 7.6C, even a flow rate of 6.0 mL/min begins to show this artifact. However, flow rates below 8 mL/min and intensities as low as 0.5 MI (100 cycles) were capable of producing signals only from the BMF tube with nanodroplets. Figure 7.7 depicts flash-difference imaging with microbubbles. Large side lobes were observed from the tube containing microbubbles.

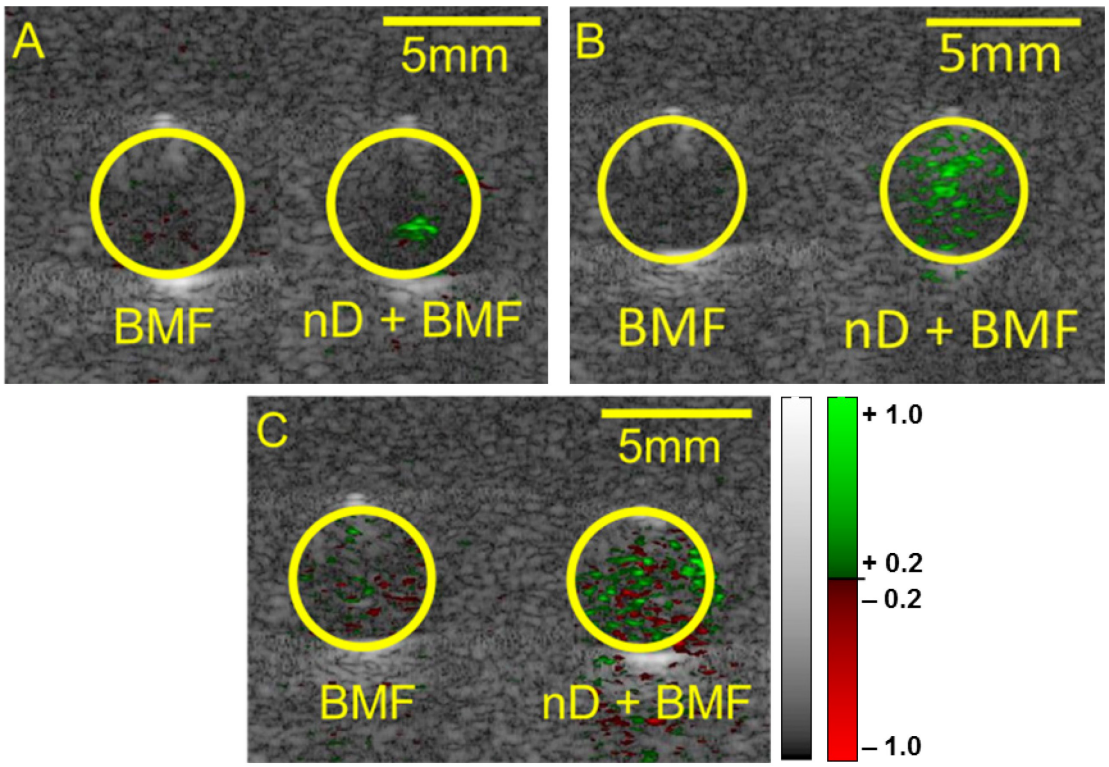

Figure 7.6 Flash-difference images with a single angle image sequence of nanodroplets. Two tubes were placed 2 cm deep in tissue mimicking gelatin. Blood mimicking fluid (BMF) with or without 2% nanodroplets (nD) flowed through the tubes (shown as yellow circles). Experimental parameters for each case are as follows: A) 100 cycles at 1.0 MI with 1.0 mL/min flow rate. B) 100 cycle at 1.7 MI with 1.0 mL/min flow rate. C) 100 cycles and 1.7 MI with 6.0 mL/min flow rate. The gray and red-green colormap represents ultrasound signal before the HIFU pulse and the percent change in ultrasound signal after the HIFU burst, respectively [35].

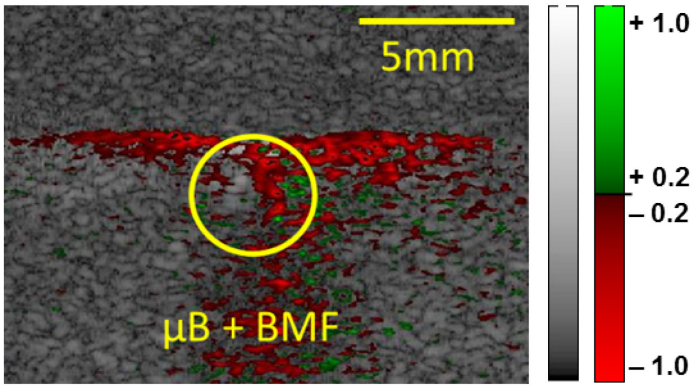

Figure 7.7 Flash-difference images with a single angle image sequence of microbubbles. A tube (shown as yellow circles) was placed 2 cm deep in tissue mimicking gelatin. Blood mimicking fluid (BMF) with 5% microbubbles (μB) flowed through the tube at 1 mL/min. A 1000 cycles, 1.7 MI ultrasound activation pulse was used to destroy the microbubbles. The gray and red-green colormap represents ultrasound signal before the HIFU pulse and the percent change in ultrasound signal after the HIFU burst, respectively [35].

After additional optimization and increasing the frame rate of the image acquisition, phantom experiments were performed that captured data at multiple angles each with pulse inversion (Figure 7.8). With this optimized program and image sequence, the background signal was substantially suppressed and the nanodroplet excitation become more salient. Furthermore, these results were subject to less motion artifacts and could reliably detect phase-change events of nanodroplets flowing at 20 mL/min.

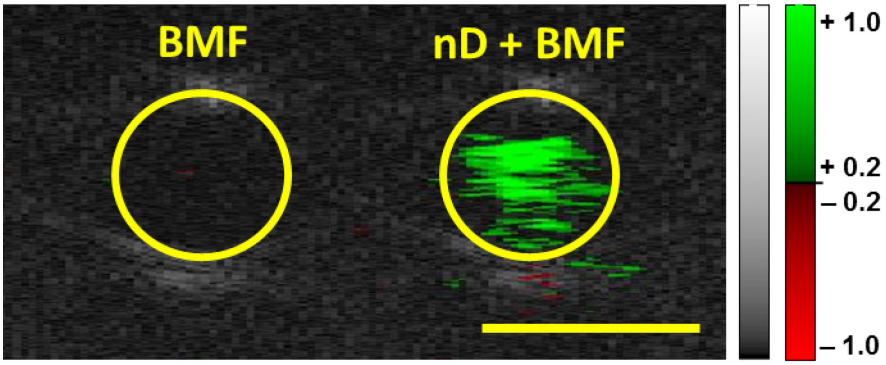

Figure 7.8 Flash-difference images using multi-angle pulse inversion image sequences. Two tubes (shown as yellow circles) were placed 2 cm deep in tissue mimicking gelatin. The tubes were subjected to a 500 cycle at 1.2 MI ultrasound and the contents were flowing at 20.0 mL/min. Yellow scalebar represents 5 mm. The gray and red-green colormap represents ultrasound signal before the HIFU pulse and the percent change in ultrasound signal after the HIFU burst, respectively [35].

7.4 Discussion

Our results have clearly demonstrated that flash-difference imaging using the Verasonics system can image phase-change events reliably with a low concentration of ultrasound contrast agents, a wide range of ultrasound intensity and cycles from a HIFU transducer, and at high flow rates in blood mimicking fluid deep within a tissue mimicking phantom. Even without multi-angle and pulse inversion, this technique improves the contrast-to-noise ratio of blood mimicking fluid and nanodroplets by up to 14-fold greater than tubes with only blood mimicking fluid. With multi-angle and pulse inversion imaging pulse sequences the contrast-to-noise ratio increased by another factor of 2-3 and supported flow rates up to 20 mL/min. Flow rate is an important consideration for flash-difference imaging as contrast agents entering or leaving the imaging voxel will cause erroneous signals from within the tubes. Although this limitation can be overcome by reducing the delays between the before and after images and the activation pulse, the delay is necessary to reject acoustic signal generated from the activation pulse itself. We believe that this technique could be used to image phase-change events for flow rates even higher than 20 mL/min; however, the flow rate on the syringe pump we had available throughout this experiment could not be increased further. Further work is needed to assess the maximal flow rate that could be imaged without detrimental motion artifacts being introduced.

One challenge we had when integrating pulse inversion imaging into the flash-difference pulse sequence was the asymmetrical pulse profile of the noninverted and inverted pulses. Using similar voltages, the inverted pulse became distorted. This asymmetry in the pulse profile created artifacts in the pulse inversion image processing and led to sub-optimal background signal suppression. Some ultrasound systems use a sequence of three pulses to do pulse inversion. Two inverted pulses with half the amplitude of the noninverted pulse are used and then all three signals are summed to reject background signal. Since we required high frame rate imaging, we decided to perform hydrophone measurements and do slight optimization of the transmit voltage to minimize the asymmetry in the pulses while still maintaining a high acoustic signal. Although not perfect, this correction was enough to reject a large portion of the background signal as seen in Figure 7.8.

Although we have demonstrated that this technique works well at numerous ultrasound settings and high flow rates, we required an external transducer to deliver the activation pulse. This leads to a rather large setup that is difficult to align as the activation pulse has to be coaligned with the

imaging pulse very precisely. The Verasonics system has an add-on option that is capable of increasing the output intensity of the array transducer. By implementing delays in the array elements, it would be possible to focus the ultrasound into a powerful acoustic wave capable of causing phase-change events with the array transducer, thus eliminating the need for an external transducer. This greatly simplifies the setup and avoids potential alignment issues from using two transducers. Future studies should investigate this technology for flash-difference type imaging sequences. This would greatly help with the alignment and, with advanced user interfacing methods, it may be possible to dynamically select where the activation pulse is targeted within the image allowing for phase-changing at a large range of depths and locations.

One change that may enhance the contrast of the phase-change events without affecting imaging speed would be to perform harmonic imaging. Harmonic imaging involves transmitting at a low frequency and receiving at a high frequency. Background signals are typically only a reflection of the transmitted wave; however, microbubbles give nonlinear signal with higher order harmonics. By only processing the higher frequency signals, the signal from only the contrast agent can be visualized and the background signals would be further suppressed.

Further investigation is required on imaging microbubbles using the flash-difference imaging technique. Our work (Figure 7.7) shows that the signal reflected by the microbubbles has large side lobes. Several factors make working with the microbubbles more difficult. First, the microbubbles have a natural tendency to float and accumulate at the top of the tube. Second, the high acoustic reflectance of the microbubbles creates a strong signal and large side lobes appear. Third, the high acoustic reflectance gives reverberation artifacts below the microbubbles, seen as a ring-down artifact in Figure 7.7. Alternative pulse sequences may be required to reduce these artifacts from microbubbles.

This work investigating the novel approach to image phase-change events of ultrasound contrast agents has great potential in research and clinical medicine. Microbubbles and novel nanodroplets are constantly being developed for delivery of therapeutics and gene transfection; however, *in vivo* assessment of microbubble destruction and nanodroplet activation is difficult and a decent imaging technique is needed. The proposed technique may be the ideal solution to aid researchers in studying phase-change events and cavitation *in vivo* as this technique can verify the destruction and activation of drug-loaded vessels such as microbubbles and nanodroplets. Additional *in vivo* work should be investigated.

In summary, this work introduced a novel image sequence that we called flash-difference imaging that is capable of imaging nanodroplet phase-change events deep within tissues. Tubes containing nanodroplets were demonstrated to have 14-fold improvement in the contrast-to-noise ratio compared to tubes without nanodroplets at a depth of 2 cm in a tissue mimicking phantom using a single plane-wave based image sequence. Further, contrast-to-noise improvements were seen by introducing pulse inversion techniques and multi-angle imaging. This imaging technique could aid researchers in evaluating newly created microbubbles or nanodroplets for drug delivery or gene transfection in both phantom and animal studies

7.5 Additional Work

The flash-difference imaging sequence described above enables monitoring of the phase-change events of nanodroplets. This is of great importance for assessing the efficacy of drug delivery, gene transfection, and biomarker liberation; however, it is also able to visualize the nanodroplets before inducing the phase-change events. By using a different formulation of the nanodroplets, porphyrins can be integrated into the shell. Porphyrins are biologically-compatible optically absorbing molecules which produce photoacoustic signals when exposed to a laser pulse at ~700 nm. This has two application: First, phase-change events can be induced with an intense laser pulse [228]. Second, dual-modality ultrasound and photoacoustic imaging can be used to visualize the nanodroplets in the liquid and gaseous form.

The latter has been demonstrated in our publication entitled “Porphyrin Nanodroplets: Sub-micrometer Ultrasound and Photoacoustic Contrast Imaging Agents” published in *Small* [39]. For this work, I helped with some of the initial photoacoustic imaging and laser-induced nanodroplet vaporization work. We were able to use photoacoustic imaging to spectrally separate the porphyrins from oxyhemoglobin and deoxyhemoglobin. This can have a profound impact in image tissue targeting of the nanodroplets and may aid in determining when an activation pulse should be applied to release therapeutic drugs or induce biomarker liberation. Combining the techniques described in this work with the flash-difference imaging would be a valuable tool in molecular imaging.

Chapter 8 Engineering Dark Chromoprotein Reporters for Photoacoustic Microscopy and FRET Imaging

This section describes the work pertaining to the development of proteins for photoacoustic imaging. This work has been published by Y. Li, A. Forbrich, J. Wu, P. Shao, R. Campbell, and R. Zemp in the article "Engineering Dark Chromoprotein Reporters for Photoacoustic Microscopy and FRET Imaging" in *Scientific Reports* in 2016 [40]. This work is conducted in collaboration with Yan Li and Robert Campbell at the University of Alberta. The ultrasound and photoacoustic imaging, as well as the signal processing and system development, were done by A. Forbrich, whereas the chemical and biological preparation and characterization of the proteins were performed by Y. Li. This section describes my contribution to the work and expands on the engineering aspects of imaging and enhancing proteins for optimal photoacoustic signal generation.

8.1 Introduction

Although some of the coloration presented by organisms are due to interference patterns of light formed by the organization of tissues, biological pigments are one of the key factors for the diverse range of colors found in many organisms such as marine corals [236, 237]. Typically, these biological pigments exist as either fluorescent proteins or chromoproteins. Both types of proteins exhibit a strong absorption of light; however, fluorescent proteins are capable of converting and emitting the absorbed energy as red-shifted light. With the discovery and isolation of the green fluorescent protein (GFP) gene from jellyfish (*Aequorea victoria*) and its homologues [15, 238], fluorescent proteins have been the subject of a great deal of research and have revolutionized optical imaging techniques. Since the underlying chromophores causing the color and fluorescence properties of these proteins are autonomously formed from the protein's intrinsic amino acid sequence, the fluorescent proteins can be genetically-encoded to enable the

investigation of biological processes and genetic pathways [16, 17]. Some fluorescent proteins do not require additional prosthetic groups or cofactors further enhancing their utility as reporter molecules [239]. For instance, GFP only requires oxygen for the protein to mature.

8.1.1 Fluorescent Proteins

Optical imaging of tissues in live animals is important for unravelling biological processes *in vivo*. Reporter molecules such as GFP and its variants have been used to optically identify populations of cells, to localize and investigate gene expression, and to non-invasively visualize biological processes occurring in the intra-cellular environment [240, 241]. Furthermore, when genetically fused to a protein of interest, reporter molecules enable sub-cellular imaging and localization of proteins. Although fluorescent proteins have revolutionized optical imaging and our understanding of biological processes, optical scattering in tissues limits high-resolution imaging at depths exceeding a transport mean free path (several hundred micrometers) [18]. Photoacoustic imaging offers a unique way to image these reporter molecules with a high depth-to-resolution ratio.

Recently, fluorescent proteins have been demonstrated to have some potential as photoacoustic reporter molecules. Razansky *et al.* [166] demonstrated that photoacoustic tomography could detect tissue-specific expression of enhanced GFP, DsRed, and mCherry fluorescent proteins several millimeters deep in tissues while maintaining 20-100 μm resolution. In 2012, an infrared fluorescent protein, engineered from a bacteriophytochrome that binds a biliverdin chromophore, was used for photoacoustic imaging *in vivo* [242]. In 2014, Krumholz *et al.* demonstrated photoacoustic imaging of infrared fluorescent proteins at a tissue depth of 8 mm with sub-millimeter resolution [167]. Although fluorescent proteins have great potential, most have limited photostability and exposure to pulsed laser energy causes absorption bleaching. Furthermore, most commonly used fluorescent proteins are optimized for the highest fluorescence quantum yield resulting in inefficient laser energy conversion into thermoelastic expansion required for photoacoustic imaging.

8.1.2 Chromoproteins

Chromoproteins are proteins that consist of a pigmented prosthetic group or cofactor bound to the folded protein structure. In tissues, the most prevalent chromoprotein is hemoglobin which allows photoacoustic imaging to visualize the vasculature network non-invasively and label-free

in vivo. Pocilloporins, from *Scleractinian* coral, were the first chromoproteins discovered in nature [243]. In 2000, the chromoprotein asCP was isolated from *Anemonia sulcate*, cloned and expressed in bacteria and mammalian cells [244]. Many other chromoproteins were isolated from nature [170, 244, 245] and, through genetic engineering, some chromoproteins were created from fluorescent proteins [246, 247]. Since chromoproteins are essentially non-fluorescent, the absorbed energy must be dissipated as heat through non-radiative relaxation pathways which is useful for photoacoustic signal generation.

Recently, these non-fluorescent chromoproteins have been investigated for use in photoacoustic imaging. Laufer *et al.* compared several fluorescent proteins to GFP-like non-fluorescent chromoproteins and demonstrated that the chromoproteins cjBlue and aeCP597 were more robust to laser-induced absorption bleaching compared to the fluorescent proteins [27]. Furthermore, since cjBlue and aeCP597 were not fluorescent, they found that the photoacoustic signal was higher with these chromoproteins.

Although these preliminary studies demonstrate that chromoproteins are promising candidates for genetically-encodable photoacoustic reporter molecules, chromoproteins are limited in the number of spectrally distinct proteins available. Fortunately, fluorescent proteins and chromoproteins are amenable to genetic engineering to modify and improve their spectral characteristics. For example, the chromoprotein Ultramarine was derived from the Rtms5 fluorescent protein for use as a dark FRET acceptor in biosensor applications [169]. To engineer the proteins, two approaches are typically taken: (1) Rational computational design relies on the theoretical analysis of existing data for the sequence and structure of proteins to enhance the desired protein characteristic [248, 249]. (2) Mutagenesis with directed evolution uses the concept of “survival of the fittest” by applying an artificial selection bias to gene libraries [250]. Although my contributions to this work were primarily on the engineering and photoacoustic imaging aspects, the latter strategy is briefly discussed since the work presented in this chapter utilizes it. Additional details on the chemical and biological aspects of this project can be found in the thesis entitled “Engineering a Chromoprotein Optimized for Photoacoustic Imaging and Biosensing Applications” by Y. Li.

8.1.3 Mutagenesis with Directed Evolution

As mentioned, mutagenesis guided by directed evolution is a process akin to the “survival of the fittest” with the aim to improve specific characteristics for the protein. This approach is often

done iteratively to gradually improve the desired characteristics. This approach is depicted in Figure 8.1. In brief, (1) a diverse gene library is generated by using some well-established techniques such as site-directed mutagenesis, random mutagenesis, and/or gene recombination [250–252]. (2) The gene library is transfected into the genome of an organism, typically *E. coli* due to their fast growth cycle. (3) The organism is allowed to grow and express the genes. (4) The gene library is screened for variants with the desired characteristics. (5) Finally, the 'best' variant is selected, isolated, and used as the template for the next iteration of mutagenesis. This process is repeated until the desired gene is found.

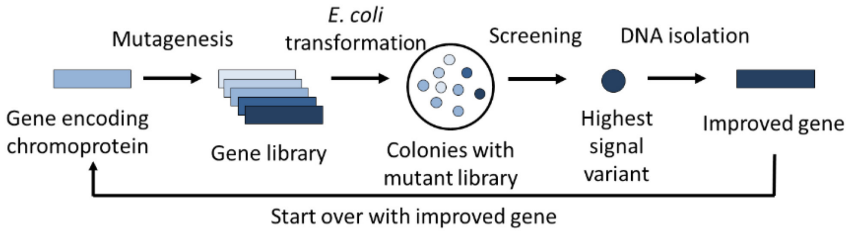

Figure 8.1 Directed evolution procedure. The gene of interest is randomly mutated to form a gene library. The gene library is used to transform *E. coli* cells, which are then grown as colonies on agar plates. The colonies are screened on the basis of their photoacoustic signal. The best colonies are selected and used as the templates for the subsequent iteration. Image courtesy of Yan Li.

For optical imaging, directed evolution approaches have expanded the number of suitable fluorescent protein greatly and have been used to (1) enhance the fluorescent emission by improving the fluorescent quantum yield or the absorption coefficient, (2) shift the absorption peak of the protein, and (3) decrease the toxicity of the gene improving cell viability. These advancements were only made possible by effective screening techniques such as direct screening of *E. coli* colonies growing on agar media [253]. Furthermore, advances in the screening techniques are correlated with the success of protein engineering efforts.

Although photoacoustic microscopy has many advantages over other imaging modalities, there are no genetically-encodable reporter proteins that have been optimized specifically for photoacoustic imaging. Furthermore, no effective screening techniques have been proposed to improve the photoacoustic properties of these protein. Just as engineered fluorescent proteins have led to major advances in live cell fluorescence imaging, engineering and optimization of new genetically-encoded reporters specifically for photoacoustic imaging will lead to improved signal-to-noise (SNR) *in vivo* imaging and help to realize the full potential of photoacoustic imaging. Part

of this chapter is devoted to a novel screening method we developed to enhance genetically-encoded proteins for optimal photoacoustic qualities. This method is analogous to directed evolution techniques that are commonly used in fluorescent protein engineering (Figure 8.1). This high throughput technique should be generally applicable to different classes of photoacoustic reporter proteins, beyond those described in this work.

8.1.4 Förster Resonance Energy Transfer

Although the simplest application of fluorescent and non-fluorescent molecules is as static reporter molecules, the utility of these reporter molecules can be extended to allow the visualization and investigation of additional properties. The fluorescent lifetime is often dependent on the molecular environment and can be affected by the polarity, pH, presence of analytes such as Ca^{2+} or O_2, concentration of fluorescent molecule, among other environmental factors [16]. These properties of fluorescent molecules allow fluorescent proteins to be engineered as active biosensors for many different applications. These biosensors have been used to study analyte flux, enzyme activity, biological recognition, and signal transduction in live cells.

One of the most commonly used biosensor takes advantage of long-range dipole-dipole interactions causing energy to be transferred between molecules in a phenomenon known as Förster resonance energy transfer (FRET) [254, 255]. FRET-constructs are formed by pairing an acceptor molecule with a donor molecule. When the molecules are in close proximity (in the nanometer range), energy that is absorbed by the donor molecule can be transferred to the acceptor molecule. However, when the molecules are more distant the energy transfer cannot occur. Often the acceptor is a fluorescent molecule which emits fluorescent when the donor molecule is excited (Figure 8.2A). However, these 'bright' acceptor-based FRET constructs often have spectral contamination such as direct acceptor excitation or donor emission bleed-through. 'Dark' acceptor-based FRET constructs (Figure 8.2B) have been investigated where the fluorescent donor protein is quenched when in close proximity to a non-fluorescent chromoproteins [169, 246, 247].

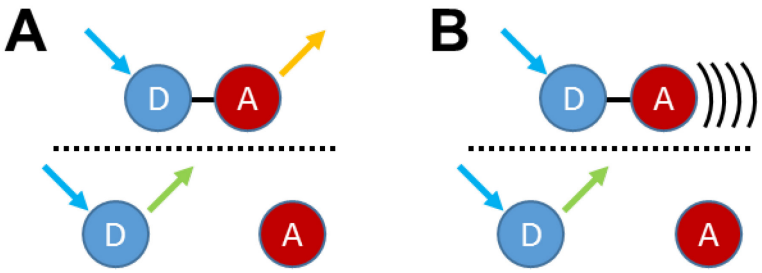

Figure 8.2 Two types of FRET constructs. Energy transfer between the donor molecule, D, and the acceptor molecule, A, can only happen when the two molecules are in close proximity. (A) For bright FRET constructs, the energy absorbed by the donor molecule is passed to the acceptor molecule which emits light. (B) For dark FRET constructs, the energy absorbed by the donor molecule is passed to the acceptor molecule and is dissipated as heat. For both cases, the energy can only be transferred when the donor and acceptor are in close proximity (above the dashed line). When the molecules are far apart the energy is not transferred and the donor molecule can fluoresce (below the dashed line).

The rate of conversion for FRET, $k_T(r)$, is found as Eq. 3.

$$k_T(r) = \frac{1}{\tau_D}\left(\frac{R_0}{r}\right)^6 \tag{3}$$

Where τ_D is the fluorescent lifetime of the donor in the absence of the acceptor molecule, r is the distance between the two molecules, and R_0 is the Förster radius. The rate of conversion of FRET is inversely related to the sixth power of the distance between molecules; hence, even small changes in r at the nanometer scale give a large, detectable change in fluorescence. For this reason, FRET is often termed as the 'spectroscopic ruler'. Practically, for the largest changes r must be within $(1 \pm 0.5)R_0$. The Förster radius, R_0, can be determined by Eq. 4 and is typically between 2-10 nm.

$$R_0^6 = \frac{9c^4\kappa^2 Q_D}{8\pi}\int_0^\infty \frac{f_D(\omega)\sigma_A(\omega)}{n^4(\omega)\omega^4}d\omega \tag{4}$$

Where c is the speed of light, κ^2 represents the relative orientation between the transition dipoles of the donor and acceptor (normally assumed to be 2/3 corresponding to random dipole orientation), Q_D is the fluorescent quantum yield of the donor, $f_D(\omega)$ represents the normalized emission spectrum of the donor, $\sigma_A(\omega)$ is the absorption spectrum of the acceptor, $n(\omega)$ is the refractive index, and ω is the angular frequency. Obviously, a high quantum yield is required by the donor to make sure most electrons decay through the fluorescent de-excitation pathway allowing for resonance energy transfer. The overlap between emission and absorption spectra of

the donor and acceptor molecules, respectively, must be maximized as seen within the integral in Eq. 4. Furthermore, to avoid potential ambiguity we must be able to excite the donor molecule such that very little excitation of the acceptor occurs. This implies that a donor with a long Stokes shift should be used. Finally, the overall efficiency of FRET, Φ_{FRET}, is related through Eq. 5.

$$\Phi_{FRET} = \frac{k_T(r)}{k_T(r) + \tau_D^{-1}} = \frac{R_0^6}{R_0^6 + r^6} \tag{5}$$

FRET-based biosensors can be encoded into the genome of cells allowing investigation of protein-protein interactions [256–259]. One example of a FRET-based biosensors is the 'cameleon' Ca^{2+} biosensor [256, 258]. When binding to calcium ions, the protein undergoes a conformational change and brings the molecules in close proximity increasing the FRET efficiency. This allows the use of a calcium-based biosensor to study neurological activity. Another strategy for developing FRET-based biosensors is to link the donor and acceptor molecules with a protease cleavage substrate. When a protease cleaves the substrate the donor and acceptor separate and hence the efficiency of FRET is decreased.

Although FRET-based biosensors have been widely explored in optical imaging, photoacoustic imaging of the FRET effect has been limited to studies of high concentrations of dye and have not been applied to biological applications [260, 261].

8.1.5 Overview

In this research, we initially describe our investigations of photoacoustic signal generation from fluorescent proteins and chromoproteins. Our preliminary studies revealed chromoproteins to be very promising genetically-encodable reporter molecules for photoacoustic imaging. These results motivated us to develop a screening methodology to enable the directed evolution of chromoproteins for improved photoacoustic signal generation. Specifically, the Ultramarine [169] and cjBlue [170] templates were subjected to multiple rounds of directed evolution to produce several fold increases in photoacoustic signal. We demonstrate multiwavelength imaging for spectral demixing the original and evolved variants of the chromoproteins in mammalian tissue. Dark FRET constructs were made of the original and evolved variants and evaluated for photoacoustic imaging.

8.2 Photoacoustic and Optical Properties of Fluorescent Proteins and Chromoproteins

To justify using chromoproteins as reporter molecules for photoacoustic imaging, we compared several optical and photoacoustic properties of representative fluorescent proteins (mCherry, EYFP, and a dark YFP-based chromoprotein known as REACh) to the chromoproteins Ultramarine and cjBlue (Table 8.1). Similar to Laufer *et al.* [27], we observed that a lower fluorescent quantum yield (QY) was associated with higher photoacoustic signal. Specifically, EYFP with a quantum yield of 0.61 gives the least photoacoustic signal, while the chromoproteins with near zero quantum yield show over an order of magnitude greater signal. We attribute the increased signal from chromoproteins to a more efficient photothermal conversion. Based on Table 8.1, we estimate that at the ANSI (American National Standards Institute) limit of 20 mJ/cm^2 imaging of 200 nM Ultramarine and 600 nM cjBlue chromoproteins with 10 dB SNR should be possible. Our estimated sensitivity agrees to within an order of magnitude with Li *et al.* [74] and Filonov *et al.* [242] who demonstrated sensitivity of 515 nM of the blue product (5,5′ -dibromo− 4,4′ -dichloro-indigo) from the *LacZ* gene and 16 μM of the infrared FP (iRFP) sample embedded in tissue, respectively.

Table 8.1 Spectral characteristics of selected fluorescent proteins and chromoproteins [50]

Protein	$\lambda_{Exc.}$ (nm)	ε_{Max} (10^3 $M^{-1}cm^{-1}$)	QY	SNR * (dB)	SNR/ε_{Max} * (10^{-6} dB/($M^{-1}cm^{-1}$))	Reference
mCherry	587	72.0	0.22	10.1	140	[262, 263]
EYFP	514	83.4	0.61	-1.9	23.2	[264]
REACh	513	100.1	0.02	18.6	186	[246]
cjBlue	610	52.7 (66.7) ‡	< 0.0001	36.1	541	[170]
Ultramarine	587	64.4 (64.0) ‡	0.001	46.4	724	[169]

*: SNR is for 100 μM of protein using 2.5 mJ/cm^2 laser fluence at the peak absorption wavelength
‡: Number provided was measured by Y. Li followed by the literature value in parentheses

Additionally, we found that the fluorescent proteins were more susceptible to photobleaching than the chromoproteins (Figure 8.3). After 1,000 laser pulses at 2.5 mJ/cm^2, the photoacoustic signal from the EYFP and REACh fluorescent proteins decreased to 40-50% while the photoacoustic signal from the Ultramarine and cjBlue chromoproteins decreased by less than 10%. The enhanced photostability and higher photoacoustic signal generated from the proteins suggested that Ultramarine and cjBlue chromoproteins would be promising tools for photoacoustic imaging.

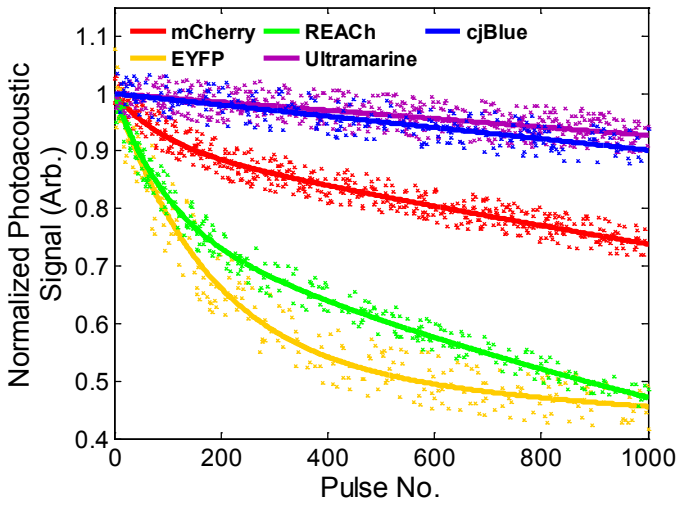

Figure 8.3 Photostabiliity of select fluorescent proteins and chromoproteins. The normalized photoacoustic signal from a series of 2.5 mJ/cm^2 laser pulses for purified mCherry (red, $\lambda_{exc.}$ = 587 nm), EYFP (yellow, $\lambda_{exc.}$ = 514 nm), REACh (green, $\lambda_{exc.}$ = 513 nm), Ultramarine (purple, $\lambda_{exc.}$ = 587 nm), and cjBlue (blue, $\lambda_{exc.}$ = 610 nm) proteins is shown. Solid lines represent curve fitting to a biphasic exponential function [50].

Multiwavelength photoacoustic imaging was used to characterize the photoacoustic spectral characteristics of Ultramarine and cjBlue. The photoacoustic spectrum closely resembled the absorption spectrum of the proteins (Figure 8.4). Furthermore, the potential for spectral demixing techniques to separate the chromoproteins Ultramarine and cjBlue from blood was evaluated. Using the multiwavelength photoacoustic signals, we performed a constrained least squared algorithm to separate the four components in the tubes: Ultramarine, cjBlue, deoxyhemoglobin, and oxyhemoglobin (Figure 8.5). Although the demixing algorithm accurately separated the cjBlue chromoproteins from Ultramarine and blood, there was slight cross-talk between the Ultramarine chromoprotein and the blood as evidence by the small amount of Ultramarine signal in the tube containing only blood. This is most likely due to the similar absorption spectrum of the Ultramarine and deoxyhemoglobin above 585 nm. *In situ* animal studies were also performed to assess the demixing of Ultramarine and cjBlue from blood. Two-dimensional ultrasound scans over a region in the hindlimb of rats where *E. coli*, expressing either Ultramarine or cjBlue protein, had been injected demonstrated that we can accurately detect the chromoproteins at depths exceeding 1 mm (Figure 8.6).

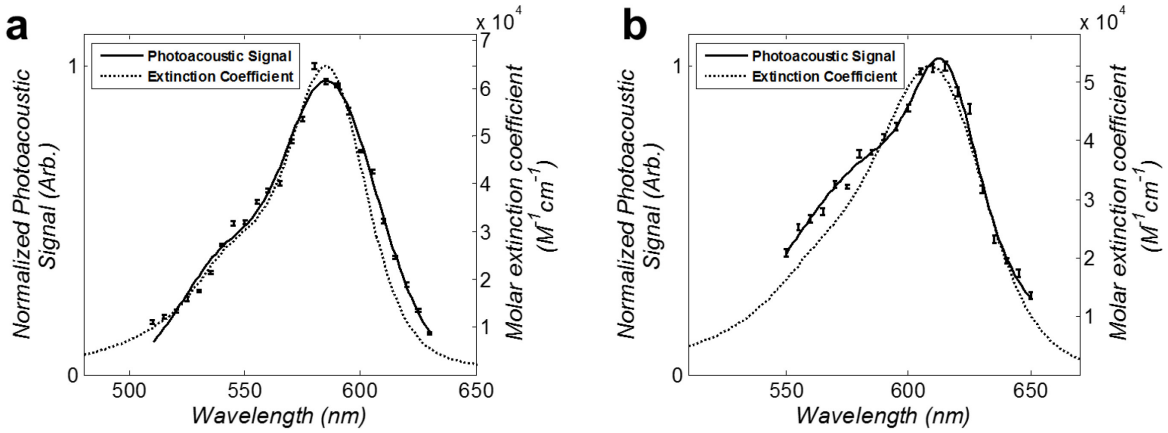

Figure 8.4 Absorption and photoacoustic spectra of Ultramarine (A) and cjBlue (B) chromoproteins. The dashed black line represents the extinction coefficient. The solid black line represents the photoacoustic signal. Error bar represent the standard deviation of the photoacoustic signal over 25 pulses [50].

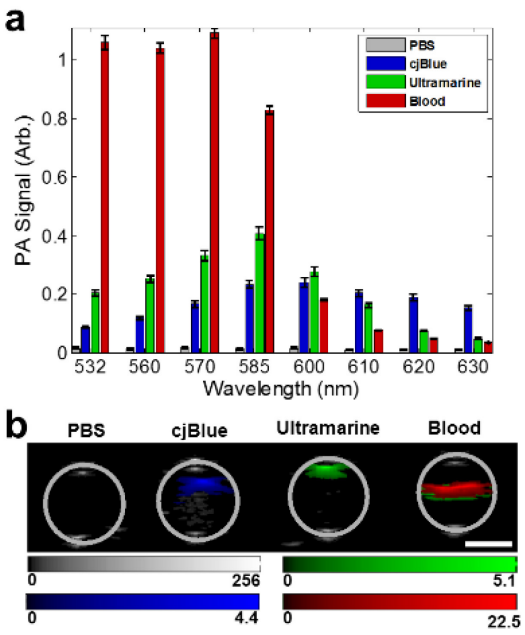

Figure 8.5 Photoacoustic signal of chromoproteins in tubes. (A) Photoacoustic signal from PBS, cjBlue, Ultramarine, and blood at 532, 560, 570, 585, 600, 610, 620, and 630 nm. (B) The estimated relative concentration of cjBlue (blue colormap), Ultramarine (green colormap), and blood (red colormap) in each tube was determined through a constrained, least-squares linear regression inverse algorithm. White scalebar represents 1 mm [50].

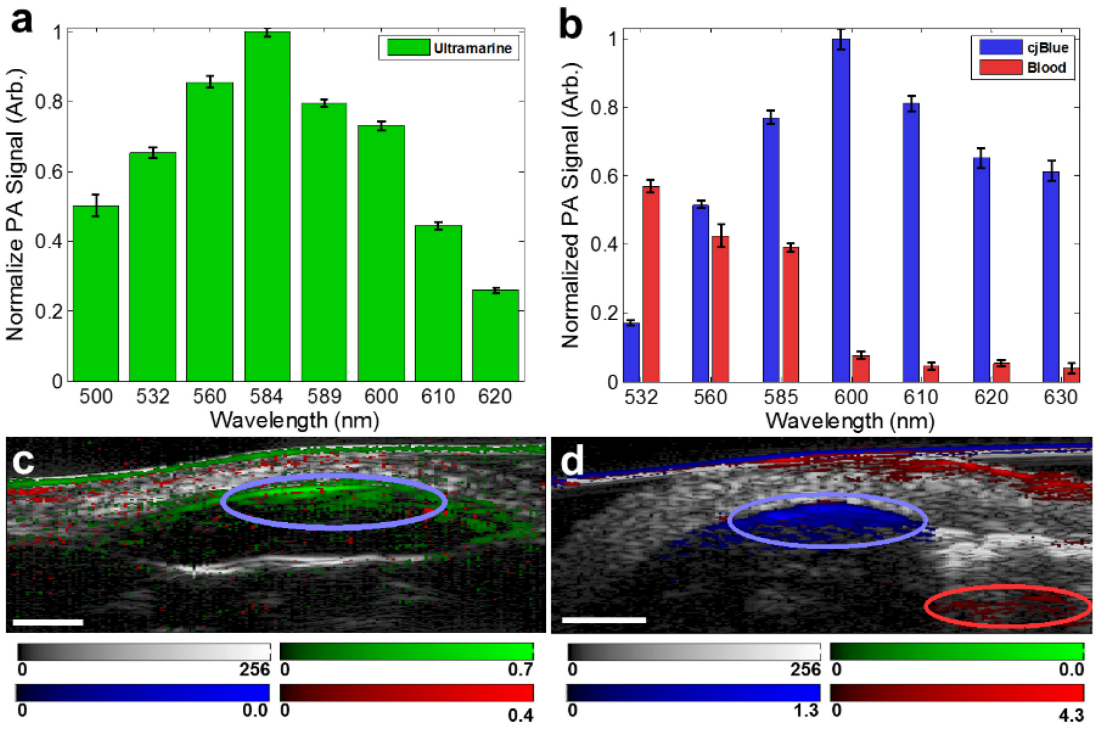

Figure 8.6 *In situ* multispectral PA imaging and spectral unmixing. *E. coli* cells (~2 × 10^8 cells/ml) producing either Ultramarine (a,c) or cjBlue (b,d) were injected into a recently sacrificed rat. Normalized average PA signal from the Ultramarine injection site of animal 1 (a) and cjBlue, as well as a region of interest thought to be blood in animal 2 (b). Spectrally unmixed B-Scan image of animal 1 (c, Ultramarine indicated by a blue ellipse) and animal 2 (d, cjBlue and blood indicated by a blue and red ellipse, respectively). The gray colormap represents the ultrasound intensity, while the blue, green, and red colormaps represent the relative concentration of cjBlue, Ultramarine, oxygenated hemoglobin, respectively. White scalebar represents 1 mm [50].

Given the characteristics of the transducer and the signal detected from the phantom imaging, we estimate that the minimum number of cells required to give 10 dB SNR at the ANSI limit is 100 - 1,000 cells per voxel. This is consistent with Figure 8.6 where a SNR of 25 dB was seen from an injection of ~2,000 cells/voxel (estimated from a 10 μL injection of 10^7-10^8 cells /mL). This is similar to Razansky et al. [265] who demonstrated that the minimum number of cells is ~10^3 for imaging DsRed-expressing HeLa cells.

8.3 Directed Evolution of Chromoproteins for Photoacoustic Imaging

As our initial data demonstrated that the Ultramarine and cjBlue chromoproteins are promising genetically-encodable reporters for photoacoustic imaging, we investigated the potential of using directed evolution to enhance these chromoproteins with better characteristics for photoacoustic imaging. As shown in Figure 8.1, one of the key steps in directed evolution for successful enhancement of protein characteristics is the screening technique. We found two screening techniques that could be used to enhance the chromoproteins for photoacoustic imaging. In the first screening strategy, the gene libraries could be qualitatively characterized with a primary direct visual inspection and quantitatively assessed using a secondary *in vitro* absorbance measurement. The assumption for this first technique is that a darker or stronger color results in better absorption. In the second screening strategy, the photoacoustic signal from each colony in the gene library was directly assessed by using photoacoustic imaging. Figure 8.12 depicts a schematic of this screening strategy. The sensitivity of this screening technique was assessed by imaging plates of *E. coli* colonies uniformly expressing the chromoprotein. The variation in photoacoustic signal was quantified as 10–13%. This variation may be due to variations in the colony size, stability of the protein, or photobleaching. The lateral resolution for the photoacoustic imaging system (~125 μm) was finer than the size of the typical colony (0.5 – 1 mm). As shown in Figure 8.7, a lateral resolution of ~0.64 mm for an *E. coli* colony of diameter 0.55 mm was measured.

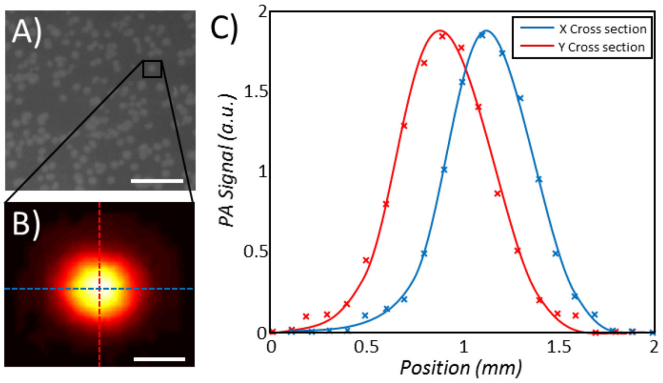

Figure 8.7 Resolution of photoacoustic imaging for screening *E. coli* colonies. (A) Grayscale camera image of a small portion of the gene library. *E. coli* colonies are seen as lighter round circles. Scalebar represents 5 mm. (B) Photoacoustic imaging of a single colony (0.55 mm diameter). The scalebar represent 0.5 mm. (C) Cross-section of the photoacoustic signal generated by the *E. coli* colony. The full-width half-maximum of the signal is 0.65 and 0.63 mm for the x and y cross-section, respectively.

The photoacoustic screening of a gene library produced by error-prone PCR (Figure 8.8A) revealed that typically there is a loss-of-function with respect to photoacoustic signal generation. The colonies that generated high photoacoustic SNR were picked off and used as the template for the subsequent round of directed evolution. After several iterations, all high-signal producing colonies were plated on a single agar dish for imaging (Figure 8.8B). The colony that produced the highest photoacoustic signal was picked for further characterization.

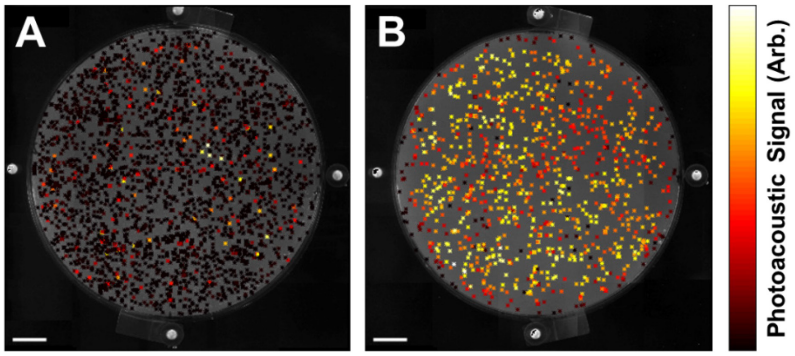

Figure 8.8 Directed evolution of Ultramarine. Screening results of either *E. coli* samples transfected with error-prone PCR Ultramarine DNA (A) or the selected enhanced variants (B). Grayscale background image represents the camera image of the agar plate, while the red colormap represents the photoacoustic overlay. Scalebar represents 1 mm [50].

For Ultramarine, four iterations of screening by absorbance-based screening followed by three iterations of photoacoustic-based screening were performed. Similarly, for cjBlue three iterations of absorbance-based screening followed by four iterations of photoacoustic-based screening were performed. These efforts led to the identification of variants of Ultramarine and cjBlue with enhanced photoacoustic signals and 5 and 4 mutations, respectively, relative to their starting templates. For a more thorough discussion of the crystal structure and the importance on these mutations see the thesis by Y. Li [50] and our equally-contributing first author paper [40].

The relative photoacoustic signal from solutions of purified Ultramarine, dUltramarine2 (the intermediate result of absorption-based screening), and tdUltramarine2 are presented in Figure 8.9A and the relative photoacoustic signal from solutions of purified cjBlue and cjBlue2 are presented in Figure 8.9B. The spectra of the original and variants are presented in Figure 8.9C,D and were found to be very similar. On a per molecule basis, we saw substantial improvements in the variants compared to the original chromoprotein. Relative to Ultramarine, the dUltramarine2 and tdUltramarine2 variants have a 1.9-fold and 4.3-fold increase in photoacoustic signal,

respectively. Relative to cjBlue, the cjBlue2 variant has a 2-fold increase in photoacoustic signal. This increase in signal is most likely attributed to the higher extinction coefficient and lower quantum yield (Table 8.2) in the variants compared to the original chromoprotein; however surprisingly, there is not a linear relationship between these factors. More research is required to understand all the factors that can affect the photoacoustic signal intensity generated from these proteins.

Table 8.2 Optical characteristics of Ultramarine and cjBlue chromoproteins and their variants

Protein	$\lambda_{Exc.}$ (nm)	ε_{Max} * (10^3 $M^{-1}cm^{-1}$)	QY	SNR ** (dB)	Oligomeric State
Ultramarine	585	64.4	0.001	46.4	monomer
dUltramarine2	587	81.5	< 0.0001	50.4	dimer
tdUltramarine2	587	203.4	< 0.0001	57.4	tandem dimer
cjBlue	610	52.7	< 0.0001	36.1	tetramer
cjBlue2	587	56.6	< 0.0001	42.4	tetramer

* : εMax is based off the monomer concentration

** : SNR is for 100 μM of protein using 2.5 mJ/cm^2 laser fluence at the peak absorption wavelength

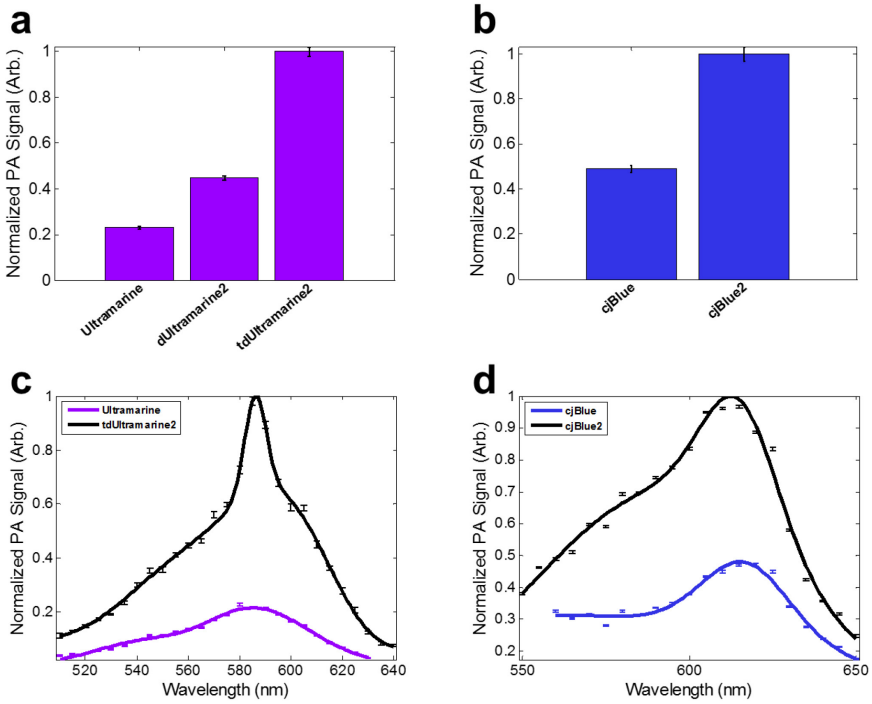

Figure 8.9 Photoacoustic characteristics of several variants found by directed evolution. (A) and (B) represent the photoacoustic signal (measured at the peak absorbance of the protein) of Ultramarine and cjBlue and variants, respectively. (C) and (D) represent the photoacoustic spectra of tdUltramarine2 and cjBlue2 variants compared to the original, respectively [50].

Since tdUltramarine2 provided the largest signal on a per molecule basis, we further investigated the utility of this protein for *in vivo* imaging. We injected *E. coli* cells (10 μL of 10^7-10^8 cells/mL) producing either the Ultramarine or tdUltramarine2 protein into the ear of an anaesthetized rat. Figure 8.10 shows the results of spectral demixing with Ultramarine expressing cells. Photographs were used to verify the site of injection. The Ultramarine-producing *E. coli* cells were difficult to detect compared with blood and demixing of the signals had mediocre results. For the *E. coli* cells producing tdUltramarine2, the SNR was much higher and demixing accurately revealed the cell distribution. Although our phantom studies showed that the tdUltramarine2 variant had 4-fold greater signal than Ultramarine at 585 nm, the peak spectrally demixed tdUltramarine2 signal in injected regions *in vivo* was on average only 2.7 ± 1.1-fold greater than the spectrally demixed Ultramarine ($p < 0.05$, $N = 4$). This may be due to the demixing algorithm including wavelengths that may not absorb as strongly as the peak absorption wavelength and noise from each acquired wavelength may propagate through the algorithm.

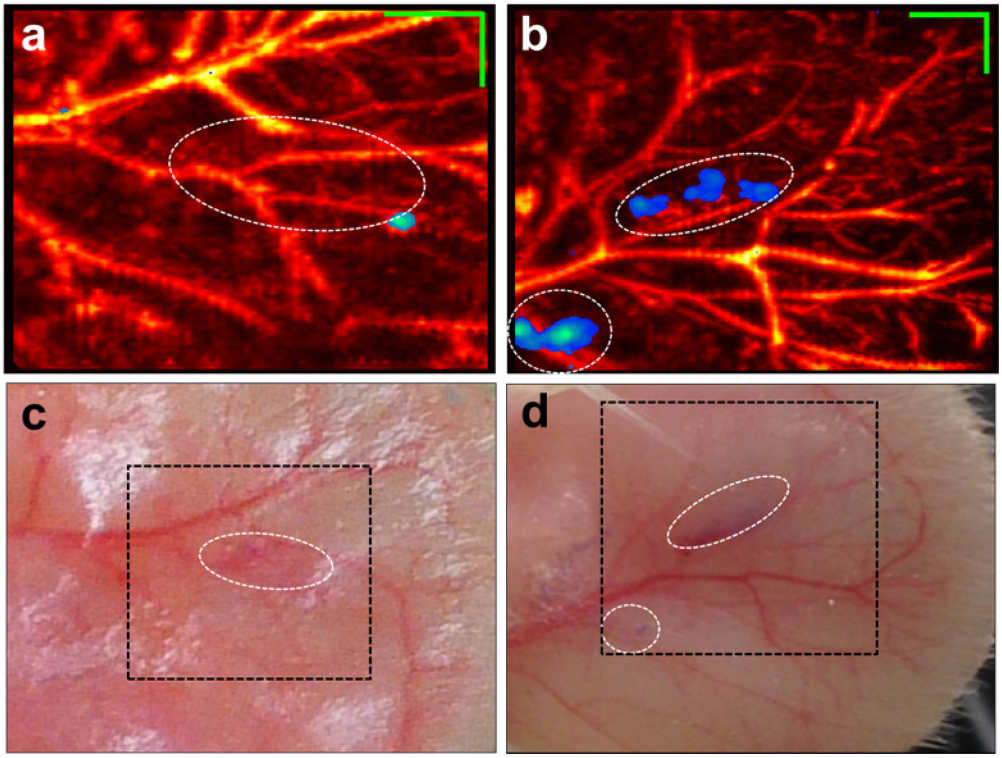

Figure 8.10 *In vivo* imaging of Ultramarine and tdUltramarine2. (A) Ultramarine-producing and (B) tdUltramarine2-producing *E. coli* pellet injected directly into the ear of a rat and the corresponding photographic images (C) and (D), respectively. The white ellipses represent the approximate injection site. Green scalebar represents 1 mm [50].

8.4 Photoacoustic Imaging of Förster Resonance Energy Transfer

Fluorescence-based FRET biosensors have proven to be useful in a range of biotechnology applications but light-scattering in tissues and tissue autofluorescence limit their utility for *in vivo* applications. Photoacoustic imaging offers an alternative and promising means for imaging of FRET-based biosensors. Specifically, changes in FRET efficiency are expected to change the efficiency of photothermal conversion, particularly for dark FRET-based constructs where the donor has a high quantum yield (*i.e.*, a poor chromophore for photoacoustic imaging) and the acceptor has a low quantum yield (*i.e.*, a good chromophore for photoacoustic imaging). Y. Wang *et al.* [260, 261] have demonstrated photoacoustic-based FRET imaging with an enhanced penetration depth and improved spatial resolution compared to planar fluorescence imaging. However, these experiments were conducted by using high concentrations of donor and acceptor dyes to produce proximity-quenching effects and no actual FRET-biosensor constructs were evaluated.

Although optimized for its photoacoustic signal and not its utility as a FRET acceptor, we expected that the tdUltramarine2 variant has utility as a dark acceptor in FRET-based protein constructs. To evaluate tdUltramarine2 as a dark acceptor, we genetically fused it to EGFP, mPapaya1, and mRuby2 via a 10-amino acid linker to create a set of 3 fusion proteins. Similarly, FRET constructs were created using Ultramarine and dUltramarine2. The linker (a 10-residue peptide sequence – GSGKKVDGGT) contained lysine amino acids which can be cleaved by trypsin. We predicted that when the FRET construct was intact, the photoacoustic signal generated when using the peak excitation wavelengths for the donor would be greater than when the FRET construct was separated (in the presence of trypsin). To test this hypothesis, we first incubated the EGFP-Ultramarine construct with varying concentrations of trypsin (0, 5, and 50 μg/ml) and imaged over time at 488 nm (the donor peak absorption) using our photoacoustic imaging setup. As shown in Figure 8.11A, we observed an exponentially decay in the photoacoustic signal, attributed to trypsin cleaving the FRET molecule and separating the donor (EGFP) from the acceptor (Ultramarine) thus decreasing the FRET efficiency. The control sample without trypsin has a much slower decay in photoacoustic signal and is attributed to photobleaching. Additional FRET constructs, with Ultramarine, dUltramarine2, or tdUltramarine2 as the acceptor, were purified and incubated with either PBS or trypsin for 30 minutes. The samples were imaged at both the donor and acceptor absorption peaks and the ratio was taken (photoacoustic signal at the

acceptor peak to the donor peak, Figure 8.11B). There was a general increase in the ratiometric signal after trypsin was added. Furthermore, the enhanced dUltramarine2 variant gave a much higher ratiometric signal increase when paired with EGFP compared with the original Ultramarine. Using the data for the extinction coefficient of blood from the literature, we estimate that a ratio of signal from oxygenated blood at 587 and 488 nm would result in a ratio of only 1.2, while our data demonstrated up to 9-fold difference in ratiometric signals from the FRET biosensors before cleavage. This potentially improves the ability to spectrally separate these components.

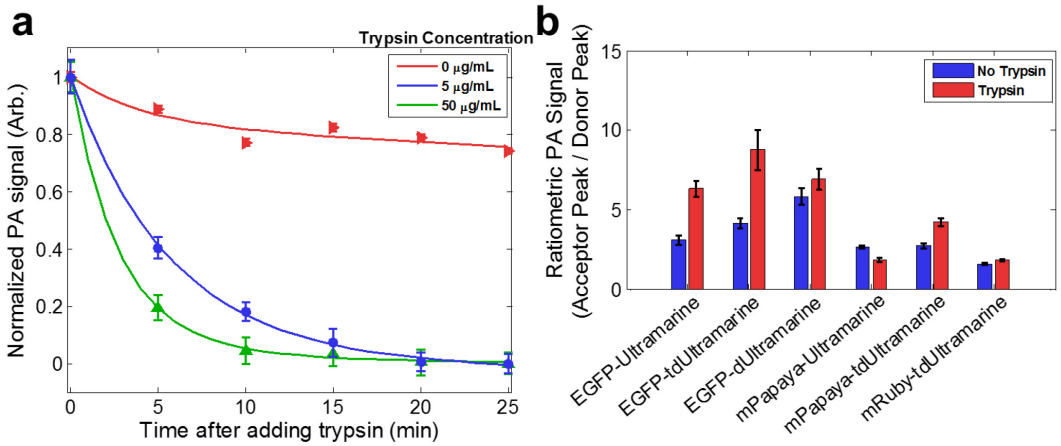

Figure 8.11 Photoacoustic FRET imaging. (a) Photoacoustic signal from a 587 nm, 2.5 mJ/cm^2 laser pulse from a FRET construct (EGFP-Ultramarine). (b) Ratiometric photoacoustic imaging of FRET molecules [50].

8.5 Discussion

While the original Ultramarine and cjBlue chromoproteins proved to be promising candidates for photoacoustic imaging due to low quantum yield, low absorption bleaching, high extinction coefficient, and high photoacoustic signal, we believed that improvements could be made to further enhance these proteins specifically for photoacoustic imaging. The directed evolution approach and associated novel screening technique presented here open up many new possibilities for photoacoustic imaging including protein engineering of genetically-encodable chromophores optimized for photoacoustic imaging and the potential for many new reporter genes to be developed. For example, the techniques developed here could be used to develop dark versions of fluorescent proteins, starting from the template of a high quantum yield fluorescent protein. This optimization could be crucial for single cell detection and for imaging proteins with low levels of expression *in vivo*.

Although we only examined chromoproteins, this same screening technique should be capable of imaging many types of proteins including fluorescent proteins. It may be expected that by evolving high quantum yield fluorescent proteins to become dark variants a larger improvement in photoacoustic signal will be seen compared to our experiments which enhanced an already-dark chromoprotein. This is expected because the change in quantum yield will be more significant greatly enhancing the photothermal conversion efficiency. Furthermore, since red and near-infrared absorption peaks are desirable for *in vivo* applications due to less light absorption and scatter, this technique could also be used to evolve proteins with red-shifted absorption peaks. This may be accomplished by performing multiwavelength photoacoustic screening and using a ratiometric approach to select the best variant with a red-shifted absorption peak. Future work could attempt to use directed evolution to red-shift the absorption peaks to the near-infrared tissue window.

One of the problems with the imaging setup is that the agar is not necessarily flat, especially around the edges where the meniscus forms. This caused a decrease in signal as seen around the edges of the plate, seen in Figure 8.8. This could be resolved by using a third axis and placing the transducer based on the time-of-flight of acoustic signals; however, we did not find this necessary since after many iterations the likelihood of detecting the best variant is very high. Another potential improvement that will provide higher throughput could be to use a linear array transducer. Furthermore, this could limit the potential effects of pulse-to-pulse instability.

Another question that arises is why the photoacoustic signal improves? The enhanced signal could come from many factors including an increased extinction coefficient, faster or enhanced protein folding, less toxic effects on the *E. coli* cells, or higher expression levels in the colonies. All these effects indicate better photoacoustic potential; however, it is important to note that the improvement may not come entirely from a higher extinction coefficient. Although it may be expected that the normalized SNR will scale linearly with one minus the quantum yield, it is interesting to note that this was not the case. For example, the ratio of the normalize SNR to one minus the quantum yield for mCherry, EYFP, REACh, cjBlue, and Ultramarine is 56, 25, 86, 950, and 3250, respectively. Factors other than the quantum yield and extinction coefficient seem to be acting in parallel to provide the increased SNR. Additional work is warranted to better understand this phenomenon.

Another interesting potential application of this work would be to study bacterial infections. Many diseases and surgical procedures have the risk of bacterial infection. These variants could be used in animal studies to non-invasively image bacterial infection with high-resolution. It could be used to perform longitudinal studies into bacterial drug treatments and study drug-resistant bacteria. Finally, future work could take the improved variants and transfect these variants into mammalian cells as reporter genes for various diseases.

To summarize, we presented a novel method to screen and evolve genetically-encodable proteins with enhanced photoacoustic characteristics. Chromoproteins were found to generate large photoacoustic signals while being relatively stable compared with other fluorescent proteins. For this reason, chromoproteins were selected as ideal candidates for directed evolution for our photoacoustic screening system. After several iterations of screening, we achieved 2 to 4-fold improvements in photoacoustic signal, which could be attributed to a higher extinction coefficient, lower quantum yield, and some other unknown factors. We believe that this screening technique will open many avenues for photoacoustic imaging of reporter molecules and help in deep-tissue, non-invasive, *in vivo* studies. While fluorescence acceptor-bleed-through was not significantly reduced for fluorescence imaging compared to wild-type Ultramarine FRET constructs, dual-wavelength photoacoustic imaging of the optimized dUltramarine2 FRET constructs produced significantly higher ratiometric signals than those from the wild-type Ultramarine FRET constructs. Photoacoustic-based directed evolution could play a role in the engineering and optimization of a large variety of spectrally unique dark reporter chromoproteins with improved spectral demixing for many applications including FRET-biosensing.

8.6 Methodology

8.6.1 Purified protein and *E. coli* sample preparation

E. coli cells were transformed by electroporation with the vectors containing either mCherry (pBAD vector, Invitrogen), EYFP (enhanced yellow fluorescent protein, pRSET vector, Invitrogen), dark EYFP (pRSET vector, Invitrogen), Ultramarine (pQE9N vector, kindly provided by Dr. Mark Prescott), or cjBlue (pRSET vector, kindly provided by Dr. Atsushi Miyawaki). A 4 mL culture, inoculated with a single *E. coli* colony, was grown overnight before being diluted into 250 mL of media (LB medium for mCherry, EYFP, and dark EYFP; M9 medium for cjBlue; Terrific broth medium for Ultramarine) containing 0.1 mg/mL ampicillin. This culture was grown in 250 mL baffled shake flasks (37°C and 225 rev./min) to the desired optical density (0.6-0.8). Protein

expression is induced by adding either 0.02% L-arabinose (mCherry), 1 mM IPTG (EYFP and dark EYFP), or 0.2 mM isopropyl 1-thio-β-D-galactopyranoside (Ultramarine and cjBlue). The *E. coli* cells were then cultured at 28°C for 24 hours for EYFP and dark EYFP, 30°C for 24 hours for mCherry and Ultramarine, or 30°C for 48 hours for cjBlue. The *E. coli* was either centrifuged down (10,000 g for 5 min) for photoacoustic imaging experiments or plated on an agar dish for photoacoustic screening (described below).

Purified proteins were used to compare optical and photoacoustic characteristics of the protein. For purification of the mCherry, EYFP, and dark EYFP proteins, the cultured bacteria were subjected to centrifugation (10,000 g for 5 min), then re-suspended in 30 mM Tris-HCl buffer (pH 7.4). French press was used to lyse the bacteria and the bacterial lysate was subjected to centrifugation (13,000 g for 45 mins at 4°C). After centrifugation, the supernatant was collected and Ni-NTA affinity chromatography (Agarose Bead Technologies) was then applied to extract purified proteins. Purified proteins from Ni-NTA affinity chromatography were then subjected to dialysis into 10 mM MOPS, 100 mM KCl, pH 7.2 for measurement.

For purification of the Ultramarine and cjBlue chromoproteins, the centrifuged *E. coli* cells were lysed by a cell disruptor (Constant Systems), purified by Ni-NTA chromatography (Amersham), then dialyzed into PBS (pH 7.4).

8.6.2 Random mutagenesis and *E. coli* plate preparation

Random mutagenesis was performed by error-prone polymerase chain reaction (PCR) as described in Fromant *et al.* [266]. In brief, Ultramarine in pQE9N (Qiagen) and cjBlue in pRSET-B (Invitrogen) were amplified with a 5' *Xho*I forward primer and a 3' *Hin*dIII reverse primer using *Tag* polymerase (New England Biolabs) in the presence of $MnCl_2$. Full-length gene libraries were digested with *Xho*I/*Hin*dIII (Fermentas) and ligated into similarly digested pBAD/His B plasmid (Invitrogen) with T4 DNA ligase (Invitrogen). Plasmid libraries were expressed in *E. coli* strain DH10B (Invitrogen) on LB (Luria-Bertani) agar plates supplemented with 0.1 mg/mL ampicillin and 0.02% L-arabinose at 37°C overnight. Fresh 0.2% agar was overlaid on the top of colonies prior to photoacoustic screening to mitigate contamination.

8.6.3 Absorbance-based screening

E. coli colonies expressing the Ultramarine or cjBlue libraries were grown on 10 cm Petri dishes. The darkest 20-30 colonies were manually picked into 4 mL LB media supplemented with 0.1

mg/mL ampicillin and 0.02% L-arabinose and incubated overnight. Crude protein extracts were obtained by taking advantage of B-PER Protein Extraction Reagent (Pierce/Thermo Scientific). 100 µL crude protein extracts were subject to absorption tests and spectra (400-800 nm wavelength scan) were recorded by a DU-800 UV-visible spectrophotometer (Beckman). After absorption-maximum comparison, the 5-10 best variants were picked and used as templates for next round mutagenesis.

8.6.4 Construction of tandem Ultramarine 7.2 dimer

To construct a tandem dimer, dimer Ultramarine 7.2 in pBAD/His B was amplified in two separate PCR reactions. In the first reaction, 5' *Xho*I and 3' *Pst*I restriction sites were introduced. In the second reaction, 5' *Pst*I with a linker and 3' *Hin*dIII sites were introduced. Three-way ligation strategy provided a tandem gene of the form A-linker-A in the *Xho*I*/Hin*dIII sites of pBAD/His B, where the linker was a 13-residue SCSGTGSTGSGSS including *Pst*I restriction site.

8.6.5 Protein characterization

Absorption spectra of the original and variant protein structures were measured by placing dilute samples into 1 cm quartz microcell cuvettes then into a DU-800 UV-visible spectrophotometer (Beckman). Molar extinction coefficients were determined by using the absorption measurements for serial dilutions of the protein, the known concentration of proteins, and the Beer-Lambert principle.

mCherry was used as a reference to determine the quantum yield of chromoproteins. Briefly, serial dilutions of the reference and proteins were created with absorbance ranging from 0.01-0.1. The fluorescence spectra of the samples were recorded using a QuantMaster spectrofluorometer (Photon Technology International). The quantum yield could be determined by using the equation $\Phi_{sample} = \Phi_{reference} \times (S_{sample}/S_{standard})$, where Φ represents the quantum yield and S represents the slope of curves obtained by plotting the total fluorescence intensity (integration of wavelength) versus the absorbance.

Gene sequence and x-ray crystallography was used to determine the amino acid sequence and the crystal structures of the variant proteins. All sequencing was performed at University of Alberta Molecular Biology Service Unit (MBSU) or University core DNA Services at University of Calgary. The X-ray crystal structure of Rtms5 (PDB ID 1MOU) is used to represent Ultramarine. The monomeric cjBlue subunit (PDB ID 2IB5) is exhibited.

8.6.6 Photoacoustic system

Figure 8.12 shows a schematic of the experimental setup. A 10 Hz, Q-switched Nd:YAG laser (SLIII-10, Continuum) and an optical parametric oscillator (SL OPO Plus, Continuum) were used to generate wavelengths ranging from 450 to 700 nm. The light was coupled into a light guide (CeramOptec Industries, 900 fibres [185 μm core diameter, 200 μm cladding diameter, 250 μm jacket diameter], NA = 0.26/0.37 ± 0.02) with one input and ten outputs to direct the light to the sample, homogenize the beam shape, and illuminate the sample uniformly. The outputs of the light guide were arranged concentrically around a 25 MHz, 12.7 mm focused ultrasound transducer (V324-SM, Olympus Panametrics-NDT) such that the center of the illumination spot was aligned with the focus of the transducer. The holder for the transducer and light guide was mounted on a motorized stage for raster scanning and positioning of the transducer. A camera was used to visualize the samples, verify the alignment of the ultrasound and sample, and detect the *E. coli* colonies on the agar plates. To automatically determine the location of the colony a circle-based Hough transform was used. This allowed point-to-point (colony-to-colony) scanning rather than raster scanning which reduced the time required per plate.

The acoustic and photoacoustic signals detected by the transducer were amplified by 39 dB using a pulser-receiver unit (5073PR, Olympus Panametric NDT) and recorded with a data acquisition card (CS8229, Gage Applied Technologies). For interlaced photoacoustic and ultrasound imaging, a digital input-output card (NI CB-2162, National Instruments) was used to synchronize the ultrasound and laser systems, similar to previous work by Harrison *et al.* [267]. A photodiode signal was recorded and used to normalize the photoacoustic signals.

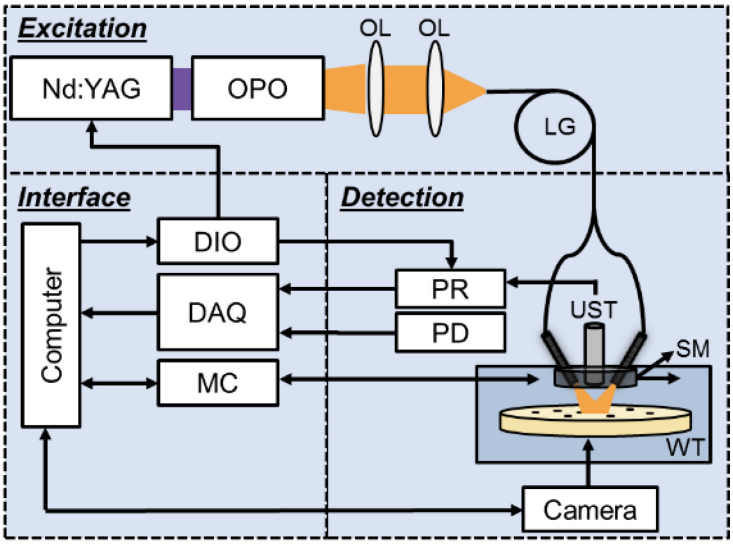

Figure 8.12 Schematic of the photoacoustic screening system. OPO, optical parametric oscillator; OL, objective lens; UST, ultrasound transducer; PD, photodiode; PR, pulser-receiver; DIO, digital input-output card; DAQ, data acquisition card; MC, motor controller; M, mirror; WT, water tank; SM, scanning motor; LG, light guide [50].

To assess the photoacoustic characteristics, purified proteins or resuspended *E. coli* cells (1-10 × 10^9 cells/mL) were diluted in PBS and injected into a 1.57 mm inner diameter tube (PE-205, Intramedic). The tubes were sealed and positioned beneath the transducer for M-mode scans (one-dimensional imaging over time), B-scan (two-dimensional imaging), and C-scan (three-dimensional imaging). To screen the *E. coli* plates, custom software was designed to integrate the data acquisition card, digital input-output card, motion controller, and camera to automatically detect and position the transducer above the *E. coli* colonies.

Animal imaging was performed by injecting 10 µL of 10^7-10^8 cells/mL *E. coli* cells producing chromoproteins or their variants into the hindlimb of a rat sacrificed just prior to the imaging or by injecting 10 µL of 10^7-10^8 cells/mL chromoprotein-producing *E. coli* cells into the ear of live rats. The rat was anaesthetized using isofluorane. Photoacoustic imaging started within 30 minutes of the injection. All animal experiments were conducted in accordance to the protocols set out by the Animal Care and Use Committee at the University of Alberta.

8.6.7 Signal and Image processing

The detected photoacoustic signals were first processed using an envelope detection algorithm, known as the Hilbert transform. SNR was calculated using the average maximum value of the enveloped photoacoustic signal divided by the noise standard deviation. For image display of C-

scans, the maximum values of each enveloped signal were used and interpolated using linear interpolation. To separate different optically-absorbing molecules such as blood and Ultramarine or cjBlue, a demixing algorithm was implemented using a constrained, non-negative, least-squares regression algorithm. All post-processing was done in MATLAB.

8.7 Future Work

8.7.1 Screening techniques with different detectors

The screening technique developed in this chapter used a single element focused ultrasound transducer to detect the photoacoustic signal generated from the *E. coli* colonies. To reduce imaging time, a custom application was developed to take in images acquired from a CCD camera and automatically locate the *E. coli* colonies reducing the number of acoustic samples that were required to image the entire plate. However, imaging times were still slow and only one position on the *E. coli* sample was imaged. Furthermore, careful alignment was needed to make sure that the image from the CCD camera was coaligned with the two motor stages to guarantee that the detected photoacoustic signal from each colony was at the center and maximized. As only a single position measurement on each colony was made, it is not possible to do post-processing to fix alignment issues or validate that the signal comes from the colony of interest.

One alternative method that was explored to try to overcome these issues was to use an array-based ultrasound system. During my graduate studies, I was fortunate enough to have the opportunity to work at FUJIFILM VisualSonics Inc. where high-frequency ultrasound array transducers and commercial multiwavelength photoacoustic imaging systems (Vevo LAZR) are developed. Using the Vevo LAZR system and a lateral motion stage, 3D ultrasound and photoacoustic images could be obtained (Figure 8.13). This gives the ability to not only validate the origin of the photoacoustic image, it could also be used to extend the parameters assessed by the screening technique. For instance, with the ultrasound image it is possible to estimate the size and depth of the colony and may allow an estimation of the photoacoustic signal per unit volume or per cell. Additionally, as the Vevo LAZR already has the ability for multiwavelength imaging, it is possible to quickly change wavelength during a scan. This could provide ratiometric datasets for developing red-shifted photoacoustic reporter molecules.

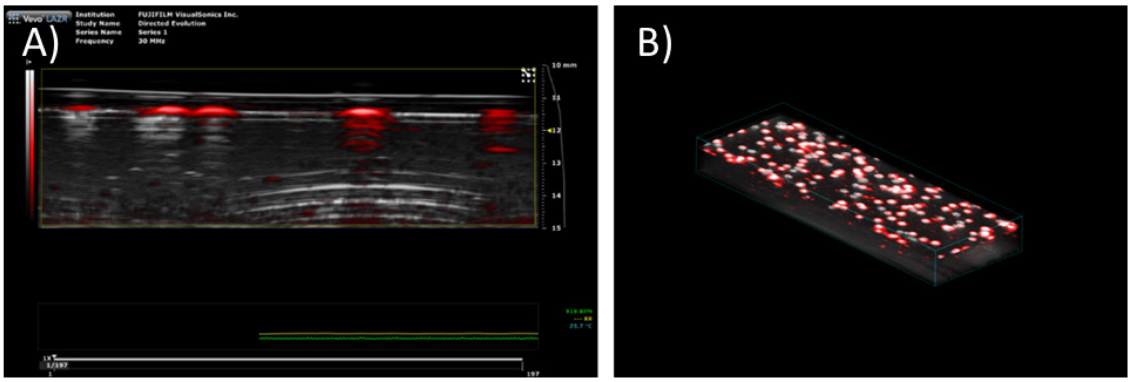

Figure 8.13 Array-based screening of *E. coli* colonies. (A) Interlaced ultrasound (gray colormap) and photoacoustic (red colormap) signals of a single slice taken with a 30 MHz array transducer. (B) A 3D reconstruction of a strip along the *E. coli* plate.

The initial results were very promising and the speed of acquisition was substantially increased. For instance, in the original screening technique an entire plate would take approximately 75 minutes to complete per wavelength. Although the array transducer required 10 scans to image the entire plate (due to the width of the transducer and travel distance of the lateral motor), the array-based screening was estimated to take only 30 minutes per plate per wavelength. With additional wavelengths, imaging would be faster with the Vevo LAZR due to the faster switching time compared with the Continuum Surelite OPO used in the single-element array transducer screening described earlier. Although the initial results were very promising, it was found that the sensitivity of the system could not easily differentiate colonies with similar amplitudes. More investigation is required on this approach for using ultrasound arrays for screening.

Another approach that could be explored is using optical-resolution photoacoustic microscopy to screen the plates (Figure 8.14). The approach would enable very high-resolution imaging of the plates and provide the ability to examine local variation of gene expression in each colony. This approach, however, is not well suited for full plate imaging as only very small portions of the plate could be imaged at a time. Additionally, due to the high fluence we found that this approach had great potential to bleach the proteins within a few pulses. Although this technique may not be suitable for screening of plates, I believe that there is great potential to develop a photoacoustic flow cytometer based on OR-PAM that could be utilized as a screening technique for cells with high photoacoustic signal expression. Further research should be conducted exploring this approach and optimizing parameters to avoid bleaching of the proteins.

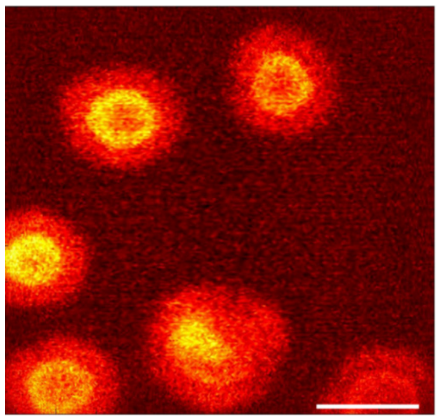

Figure 8.14 Optical-resolution photoacoustic microscopy-based screening of *E. coli* colonies. The white scalebar represents 0.5 mm.

8.7.2 Protein characteristics

As mentioned there are a number of protein characteristics that could be explored to optimize proteins for photoacoustic imaging. In the work developed for this thesis, we focused on improving extinction coefficient and reducing quantum yield to enhance the photoacoustic signal. However, screening for wavelength characteristics (using multiwavelength ratiometric approaches), photostability (using a time analysis of the photoacoustic signal from multiple laser pulses), toxicity (analysing colony size), and expression in mammalian cells (screening mammalian cells rather than *E. coli* cells) could be performed to enhance the photoacoustic characteristics of the reporter molecule. Recently, photo-switchable proteins have gained interest in the research community as a potential reporter molecule for differential imaging which may be used to decrease background signals, increase detection sensitivity, and increase penetration depth [41]. These photo-switchable proteins change their absorption characteristics when exposed to certain wavelengths of light and, in certain proteins, this process is reversible. The screening technique described here may be adapted to enhance the photoacoustic signals from these proteins, modify the absorption characteristics in either 'on' or 'off' state, or increase the efficiency of photo-switching.

8.8 Conclusion

This section was dedicated to the development of a novel method to screen and evolve genetically-encoded proteins with enhanced photoacoustic characteristics. We demonstrated a 2-4-fold increase in photoacoustic signal after only a few iterations of directed evolution with both Ultramarine and cjBlue chromoproteins. We also demonstrated, for the first time, FRET-

based photoacoustic imaging with genetically-encodable proteins. There is still much more potential that could be explored to further enhance proteins for photoacoustic imaging.

As with fluorescent proteins, there are many nonlinear properties of molecules that could be examined. This chapter briefly investigated the nonlinear phenomenon of FRET using photoacoustic imaging. With slight modifications, this screening technique can be used to enhance these nonlinear properties; however, first a better understanding of these nonlinear properties is required. In the next chapter, photoacoustic imaging of lifetime-based imaging is explored. Although the following chapter utilizes dyes for examine the excited-state and ground-state of molecules, the same concepts can be applied to proteins and new screening techniques may eventually be required to develop proteins with nonlinear photoacoustic properties compatible with *in vivo* studies.

Chapter 9 Lifetime-Weighted Photoacoustic Imaging

One of the goals of my research is to expand the contrast mechanisms available for ultrasound and photoacoustic imaging in order to provide new methods to extract molecular information. One optical technique that can be adopted to photoacoustic imaging is lifetime-based imaging. Photoacoustic lifetime imaging has been used to assess the partial pressure of oxygen in tissues by imaging methylene blue; however, fast imaging techniques for assessing the relative lifetime of the molecules using photoacoustic imaging has not been explored greatly. The work presented in this chapter has been published and taken with permission from A. Forbrich, P. Shao, W. Shi, and R. Zemp "Lifetime-Weighted Photoacoustic Imaging" published in the *Journal of Optics* [45].

9.1 Introduction

Photoacoustic imaging has emerged as a powerful hybrid bioimaging technology providing optical absorption contrast with ultrasonic or optical spatial resolution. There has been extensive research in photoacoustic imaging demonstrating utility for imaging angiogenesis and microvascular networks [268, 269], estimating oxygen saturation and oxygen flux [72, 144], imaging optical reporters such as chromoproteins and fluorescent proteins [27, 166, 167, 242], the *lacZ* operon [74, 118] or an inducible tyrosinase gene [164]. In such applications, absorption spectra can be used to spectrally separate photoacoustic images into maps of dominant absorbing molecules. However, many molecules have similar absorption peaks and spectral demixing algorithms may not be able to separate these molecules based on the static photoacoustic signal generated. Excited-state lifetimes (ESL) and ground-state recovery (GSR) times are additional molecular properties that can lead to new contrast mechanisms for photoacoustic imaging.

Although lifetime imaging techniques have been widely studied in other optical modalities, such as fluorescence imaging, and have the capabilities to indirectly study the local molecular environments (pH, analyte concentrate ion, etc. [16, 17]), it has not been investigated greatly for photoacoustic imaging [44, 270]. Lifetime imaging typically involves a pump-probe experiment to first excite the molecules to a higher state and then image the molecules in the transient state. Using this technique, Ashkenazi [44] demonstrated photoacoustic lifetime imaging of dissolved

oxygen using methylene blue, a highly absorbing molecule that has long, oxygen-dependent lifetimes. By varying the time separation between the pump and probe pulses and fitting the resulting photoacoustic signal to an exponentially-decaying curve, he was also able to determine the partial pressure of oxygen in a sample. Recently, due to their high optical absorption, stability, and biocompatibility, porphyrins have been investigated for use as a photoacoustic contrast agent in the form of biochemical constructs such as porphysomes, microbubbles, and nanodroplets [39, 99]. As with methylene blue, porphyrins have long lifetimes and can be used for lifetime-based photoacoustic imaging to probe the molecular environment surrounding a sample.

One issue with these lifetime imaging methods is that they can require many pump-probe pulse pairs at varying time separations. This makes imaging slow and subject to the accumulation of many errors such as motion artifacts. Furthermore, requiring many pulses for imaging may make the molecule undergo absorption bleaching or photobleaching. Finally, imaging over a long period of time may result in a slight change in the molecular environment around the particles such as temperature, pH, and ion concentration which may affect the lifetime parameter and may affect the accuracy of the recovered decay rate of the molecules. To improve imaging speeds, S. Huang *et al.* [271] demonstrate a differential imaging approach that sacrificed quantitative imaging and instead imaged the relative change in signal due to nonlinear lifetime effects. This approach only used three pulses to visualize nonlinear effects: once with pump and probe, once with pump only, and once with probe only. In these experiments, the pump and probe pulses were offset by 10 ns and the photoacoustic signals of the pump and probe signal were overlapped. To get the differential image, the overlapped pump and probe signal was subtracted by the pump only and the probe only signal resulting in only the signal due to the molecules in the excited state.

We further improved on these experiments and demonstrate a pump-probe experiment to provide lifetime-weighted images with only two pump-probe pulse pairs. This technique visualizes molecules with long lifetimes, such as methylene blue and porphyrins, while nulling those with short ones, such as hemoglobin. This approach has potential applications to photodynamic and photothermal therapy monitoring and contrast-enhanced molecular imaging. This work also extends lifetime imaging to photoacoustic imaging of the GSR time which has not been explored in the photoacoustic literature.

9.2 Theory

When a molecule absorbs energy, it undergoes a transition from the ground state (N_0) to a higher energy state (N_2). The excited molecule returns back to ground state through several competing radiative and non-radiative relaxation pathways including fluorescence, resonant energy transfer, vibrational and rotational relaxation, and phosphorescence. Most of the relaxation pathways occur quickly (on the order of femtoseconds to nanoseconds); however, phosphorescence is relatively slow (on the order of microseconds). Phosphorescence typically involves an intersystem transition of an electron from a singlet-excited state (N_2) to a triplet-excited state (N_1). Since it requires an electron to flip its spin, the transition from the triplet-excited state back to the singlet-ground state is unfavoured and, consequently, it is a slow process. Due to the slow process, many interesting phenomena can be investigated more easily with phosphorescent molecules including ESL and GSR time of a molecule. Experiments investigating these phenomena typically involve a pump-probe approach where the molecule is first excited to a higher energy state and then the molecule is interrogated as it recovers back to the ground state.

For both ESL and GSR imaging, the wavelength of the pump pulse is often selected as the peak absorption of the molecule of interest. At time t after the pump pulse, the number of molecules that are in the triplet-excited state $N_1(t)$ can be represent by an exponential decaying function as given by Eq. 6, where I represents the intensity of the pump pulse, τ_L represents the excited-state lifetime of the molecule, N_0 represents the number of molecules, I_{sat} represents the saturation intensity, ν_{pump} represents the frequency of the pump pulse, $\sigma_{A_{pump}}$ represents the absorption cross-section at the wavelength of the pump, and h represents Planck's constant. For simplicity, the intersystem crossing efficiency (50% for methylene blue [272]) is left out of the equation.

$$N_1(t) = \frac{N_0}{I_{sat}/I + 1} e^{-\frac{t}{\tau_L}}, \text{ where } I_{sat} = \frac{h\nu_{pump}}{\sigma_{A_{pump}}\tau_L} \quad (6)$$

For ESL imaging (Figure 9.1A), the probe pulse has sub-bandgap energy and can only be absorbed by molecules in the triplet-excited state. Therefore, the photoacoustic signal generated by the probe pulse is proportional to the number of molecules in the triplet-state. The lifetime-weighted signal, $LWI(T)$, can be represented by the photoacoustic signal of the pump-present probe signal, $PA_+(\lambda_{probe}, T) \approx P_+ e^{-T/\tau_L} + P_{bkgnd}$, subtracted by the pump-absent photoacoustic probe signal, $PA_- \approx P_{bkgnd}$, as given by Eq. 7. P_+ and P_{bkgnd} are constants that are independent of the

time interval, T, between the pump and probe pulses and are related to $P = \mu_A \Phi \Gamma$, where μ_A represents the absorption coefficient, Φ represents the fluence, and Γ represents the Grüneisen parameter. The ESL-weighted imaging signal computed for each photoacoustic image pixel is thus:

$$LWI(T) = PA_+ - PA_- = P_+ e^{-\frac{T}{\tau_L}}, \text{ where } P_+ \approx \left(\frac{\Gamma \eta_{th} \sigma_A(\lambda_{probe}) \Phi_{probe} N_0}{1 + \frac{\tau_{laser} h\nu_{pump}}{\Phi_{pump} \sigma_A(\lambda_{pump}) \tau_L}} \right) \quad (7)$$

Equation 7 demonstrates that the lifetime-weighted image for ESL imaging exponentially weights the lifetime. Hence, this imaging technique is sensitive to molecules with long ESL, such as methylene blue and porphyrins, and rejects molecules with short lifetimes, such as blood.

For GSR imaging (Figure 9.1B), the probe pulse has similar energy as the pump pulse and is only absorbed by the molecules that have returned to the ground-state. Therefore, the photoacoustic signal generated by the probe pulse is proportional to the number of molecules that have returned to the ground-state. A similar exponential decay can be found for GSL-weighted imaging. Eq. 8 represents the ground-state population after a pump pulse, where τ_{GSR} represents the ground-state recovery lifetime.

$$N_0(t) \approx N_0 - \frac{N_0}{I_{sat}/I + 1} e^{-\frac{t}{\tau_{GSR}}} \quad (8)$$

The ground-state based lifetime-weighted signal, LWI_{GSR}, can be represented by subtracting the pump-present probe signal, $PA_{GSR+}(\lambda_{probe}, T) \approx P_0 \left(1 - \frac{1}{\zeta + 1} e^{-\frac{T}{\tau_{GSR}}} \right) + P_{bkgnd}$, by the pump-absent probe signal, $PA_-(\lambda_{probe}) \approx P_0 + P_{bkgnd}$, as given by Eq. 9.

$$LWI_{GSR}(T) = \frac{P_0}{\zeta + 1} e^{-\frac{T}{\tau_{GSR}}} \quad (9)$$

where $P_0 = \Gamma \eta_{th} \sigma_{A_{probe}} \Phi_{probe} N_0$ and $\zeta = \frac{\tau_{laser} h\nu_{pump}}{\Phi_{pump} \sigma_A(\lambda_{pump}) \tau_L}$.

Again, there is an exponential weighting of the ground-state recovery lifetime on the lifetime-weighted image. This imaging technique would be sensitive to molecules with long GSR times, such as methylene blue and porphyrins, and eliminate signal from molecules with short GSR times, such as blood. It should be emphasized that the theoretical work presented here is based on a 3+1 energy level model which may be an oversimplification for many molecular species with more complicated energy-level dynamics.

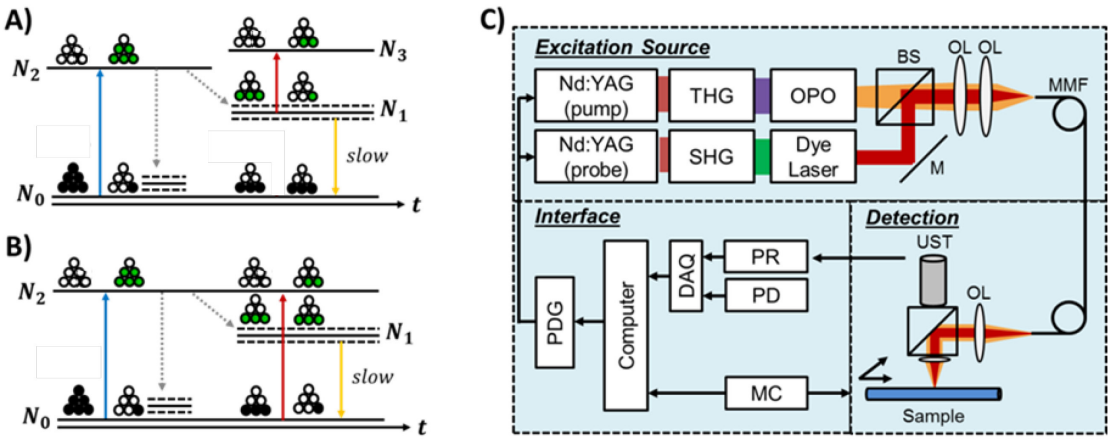

Figure 9.1 State diagram and experimental setup for (A) excited-state lifetime imaging and (B) ground-state recovery. For simplicity, a 3+1 energy level diagram is depicted. For both (A) and (B), a pump pulse (blue) is used to excite molecules to a higher electronic state. Note that the open and closed circles represent the probability of the state be empty or occupied by a molecule, respectively. In (A), the probe pulse (red) is only absorbed by those molecules that are in the higher electronic state. In (B), the probe pulse (red) has enough energy to be absorbed by the molecules in the ground state. Since the molecules return to ground state slowly, the photoacoustic signal generated by the pump will depend on the delay between the pump and probe pulses. (C) Experimental setup for excited-state lifetime and ground-state recovery based experiments. THG: Third harmonic generator; SHG: Second harmonic generator; OPO: Optical parametric oscillator; BS: Beamsplitter, OL: Objective Lens; MMF: Multimode fiber, M: Mirror; UST: Ultrasound transducer; PR, Pulser-receiver; PD: Photodiode; DAQ: Data acquisition card; MC: Motor controller; PDG: Pulse delay generator.

9.3 Materials and Methods

Similar to Forbrich *et al.* [273], two Nd:YAG lasers (Surelite III, Continuum) were used in the lifetime-weighted photoacoustic system (Figure 9.1C). The first Nd:YAG laser was used to pump a dye laser (ND6000, Continuum) containing LDS 698 and generate a 5 ns, ~50 mJ pulse at 680 nm. The second Nd:YAG laser was frequency-doubled and used to pump an OPO (optical parametric oscillator, Continuum) and generate either a 10 ns, ~40 mJ pulse at 680 nm or a 10 ns, ~60 mJ pulse at 810 nm. A pulse-delay generator was used as a master clock to trigger both the flashlamp and Q-switch triggers of the lasers and synchronize the pump and probe laser sources. The pump and probe light paths were combined and co-aligned through a beam splitter and a pair of objective lens into a 600-micron multimode fiber. The output of the multimode fiber was collimated and then focused through a prism, which was designed to reflect light at 90° while allowing the transmission of ultrasound. A 50 MHz ultrasound transducer was used as a detector

capable of 50 µm resolution. The output of the light was centered through an acoustic lens that was attached to the prism and co-aligned with the acoustic detector. The fluence at the surface of the sample was approximately 15 mJ/cm^2 and 10 mJ/cm^2 for the pump and probe pulses, respectively. A two-channel data acquisition card was used to collect (1) photoacoustic signals detected by the ultrasound transducer that were amplified with a 39-dB gain pulser-receiver and (2) a photodiode signal which was used to correct for pulse-to-pulse laser instability. A motorized stage was used to move the sample and acquire C-Scan images. A custom-designed user interface for data acquisition, motor control, and the pulse delay generator was used.

A 1 mM methylene blue sample and a phospholipid aqueous stock of 0.75 mg/mL 1-stearoyl-2-pyropheophorbide-sn-glycero-3-phosphocholine [272, 273] sample were prepared and deoxygenated by pumping nitrogen through the sample. A pO_2 electrode (DO_166MT-1 Micro Dissolved Oxygen Electrode, Lazar Research Laboratories, Inc., USA) was used to estimate the partial pressure of oxygen in the samples. The samples were then drawn from the mixing chamber with a syringe pump into polyethylene tubing and placed under the imaging prism using ultrasound gel as a coupling medium. For ESL absorption imaging, the pump and probe wavelengths were set to the peak absorption wavelength of 680 and 700 nm for methylene blue and Pyro-18 lipids (porphyrin-lipids kindly provided by Prof. Gang Zheng of the University of Toronto), respectively. For both samples, 810 nm was used as a probe wavelength (where transient absorption is significant but ground-state absorption is negligible). For ground-state recovery a pump and probe pulse of 680 nm was used. MATLAB was used to process the data.

9.4 Results and Discussion

Experiments were performed to measure the ESL and GSR lifetimes of methylene blue and porphyrin-lipids. Figure 9.2A plots the GSR lifetime-weighted photoacoustic signal as a function of pump-probe delay in a sample of methylene blue. Curve-fitting produces estimates of the GSR lifetime for a measured pO_2 level. Similar to the findings of Ashkenazi [44], we found that there was a linear dependence between the decay rate (lifetime) of methylene blue and the oxygenation of the sample (Figure 9.2B). Note that rates here are roughly an order of magnitude larger than the triplet excited state decay rates shown by Ashkenazi [44]. Ground-state recovery rates may be faster than transient absorption decay rates as there may be multiple relaxation pathways contributing to ground state recovery in addition to the relaxation from the long-lifetime triplet excited state. Furthermore, we verified the dependency between the transient

absorption decay rate of porphyrins and the oxygenation concentration in the sample (Figure 9.2C and D).

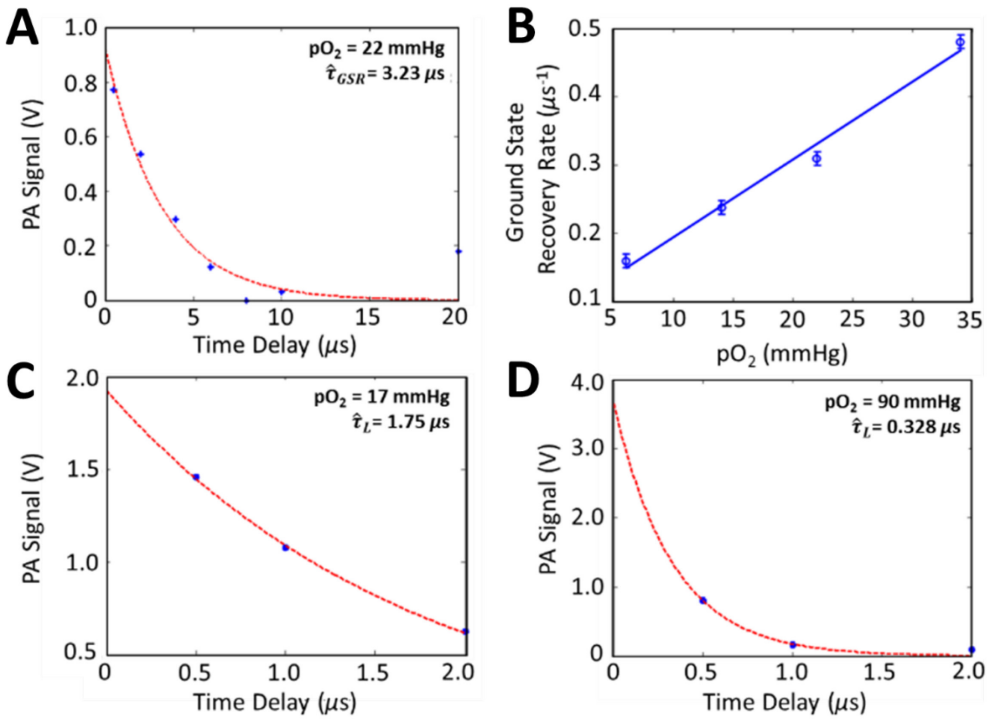

Figure 9.2 Photoacoustic signal lifetimes. (A) GSR lifetime imaging of methylene blue with pO_2 of 22 mmHg. (B) The relationship between the pO_2 of the methylene blue sample and the GSR lifetime. (C) and (D) ESL of Pyro-18 phorphyrins at pO_2 of 17 and 90 mmHg, respectively.

GSR lifetime-weighted photoacoustic imaging (GSR-LWI) was first performed on samples containing either deoxygenated methylene blue, heparinized rat blood, or a 50-50 mixture of the two samples. The pump and probe pulses were at a wavelength of 680 nm. Figure 9.3A shows the photoacoustic signal of the probe signal with pump-probe delay of ~5 µs. Although, the photoacoustic signal from blood is slightly lower than the photoacoustic signal from the methylene blue sample it is still quite difficult to differentiate these tubes. Figure 9.3B shows the lifetime-weighted photoacoustic signal and demonstrates that the signal from blood is substantially reduced compared to the signal from methylene blue. For the photoacoustic image, the signal-to-noise ratio is 37.5, 32.5, and 37.2 dB for the tube containing methylene blue, blood, and the 50-50 mixture of methylene blue and blood, respectively. For the lifetime-weighted image, the signal-to-noise ratio is 33.8, 21.2, and 27.9 dB for the tube containing methylene blue, blood, and the 50-50 mixture of methylene blue and blood, respectively. For *in vivo* imaging, this

would represent an enhanced contrast between the unwanted background signal (blood) and the methylene blue samples of approximately 2.5-fold.

A clear difference was seen between all three tubes. The deoxygenated methylene blue had the highest signal intensity of the three tubes, which is expected from previous work by Shao and Ashkenazi [274] since the lifetime is long. The signal from the blood tube was nullified in the lifetime-weighted imaging. This is due to the ps-scale excited-state lifetime of hemoglobin or ns-scale ground-state-recovery time. Finally, the 50-50 mixture of methylene blue and blood had a small signal intensity which implied that the lifetime was short. This is due to the blood being oxygenated and decreasing the lifetime-weighted methylene blue signal. These results were replicated using porphyrins.

Longitudinal images of the probe signal (at 810 nm) from tubes containing methylene blue and ICG (another short lifetime molecule) are presented in Figure 9.3C and E, respectively. The excited-state lifetime-weighted images of the methylene blue and ICG are also presented in Figure 9.3D and F, respectively. The subtraction of the probe signal without the pump pulse from the probe signal with the pump pulse clearly emphasises the signal from the methylene blue tube while greatly reducing the signal from the ICG tube.

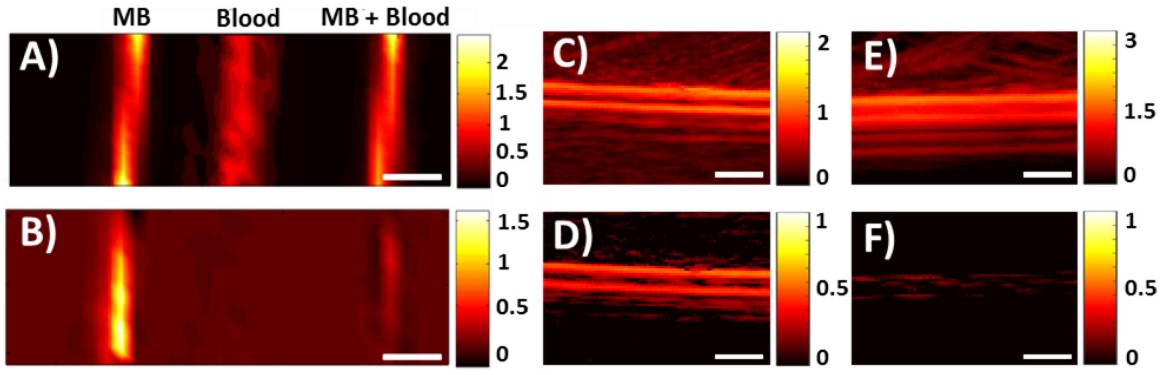

Figure 9.3 Lifetime-weighted imaging of tubes filled with methylene blue or blood. (A, B) Lifetime-weighted imaging of tubes filled with, from left to right, methylene blue (MB), blood, and a mixture of methylene blue and blood. (A) Probe signal ~5 µs after a pump pulse. (B) Ground-state lifetime-weighted image formed by taking the difference between two probe signals at different time delays. (C, E) Probe signal without any pump pulse for methylene blue (C) and ICG (E). (D, F) Excited-state lifetime-weighted image formed by taking the difference between a probe pulse with and without a pump pulse for methylene blue (D) and ICG (F). The white scale bar represents 1 mm. The colormap represents the photoacoustic signal (V).

Our results show that background signals, such as blood, can be significantly muted using the proposed lifetime-weighted imaging technique. There are a number of competing factors, however, to consider when evaluating the lifetime-weighted image of a sample with photoacoustic imaging. It has been reported that photoacoustic signal changes depending on the temperature of the samples [275]. Since two pulses of light in quick succession are required to generate the images, it is possible that the pump laser generates heating which modulates the Gruneisen parameter causing photoacoustic intensity changes in the probe laser. We believe that the low laser fluence and the μs-scale time separation mitigated this effect. Furthermore, evidence that we are not just detecting this heating effect is our ability to estimate lifetimes dependent on partial oxygen pressure as shown in Figure 9.2. It should be noted that the pulse-to-pulse stability of the pump laser may nonlinearly affect the probe photoacoustic signal. Finally, another important factor to consider is that there are many different decay pathways (photobleaching, vibrational or electronic relaxation, resonance energy transfer, etc.) acting simultaneously to restore the molecules to the ground state. Despite these other factors, we believe that the lifetime-weighted images presented here of methylene blue represent a mapping of the GSR lifetime and that further investigation is warranted for this imaging technique.

For *in vivo* imaging, the high concentration of methylene blue and porphyrins used in these phantom experiments may be difficult to achieve with intravenous injections. However, bolus subcutaneous injections can still prove useful and *in vivo* lifetime imaging have been demonstrated for subcutaneous injections with methylene blue concentrations as high as 5 mM [274]. Furthermore, Figure 9.3B demonstrates that there is a large change in photoacoustic signal amplitude when both the pump and probe are used compared to just the probe pulse. The average signal change is approximately 2-fold greater than the background signal in the lifetime-weighted image. By averaging over more pulses and sacrificing the signal-to-noise ratio, lower concentrations can be achieved.

We believe that the demonstrated lifetime-weighted imaging technique has many potential applications including the examination and guidance of photodynamic therapy oxygen depletion, the visualization of contrast agent distribution, the quantification of tumor partial pressure of oxygen, and other molecular imaging applications. Of course, it is also possible to use multiwavelength spectroscopic demixing to separate molecular species; however, such previous approaches provide no useful lifetime information, for example, for sensing partial oxygen

pressure. In the future, a combination of lifetime and spectral separation techniques may provide maximal information content. Finally, since the ground-state recovery and excited-state lifetime parameters are affected by multiple parameters including temperature, pH, and ion concentration, the proposed lifetime-weighted imaging technique could be used to analyse these environmental conditions while minimizing the effects of photobleaching. This work should be examined in future research.

9.5 Conclusion

In summary, we demonstrate a technique to visualize the excited-state or ground-state recovery of a long-lifetime agent with a triplet-excited state in lifetime-weighted photoacoustic images. While transient absorption photoacoustic imaging has been previously introduced, the concept of lifetime-weighted imaging using probe measurements with or without a pump pulse has not previously been demonstrated. Moreover, for the first time to our knowledge such measurements are performed on porphyrin lipids. These are key components of porphysomes and porphyrin nanodroplets recently introduced. Additionally, we demonstrate ground-state recovery photoacoustic imaging and show it is possible to obtain lifetime information even when pump and probe wavelengths are identical. The proposed ground-state recovery and transient absorption lifetime-weighted imaging techniques can be used to differentiate spectrally similar targets based on lifetime and can provide surrogate lifetime-related information such as pO_2 which is not possible with existing spectral demixing techniques. We believe that the lifetime-weighted photoacoustic imaging technique has many potential applications in biomedical imaging including studying photodynamic therapy dosimetry guidance and oxygen sensing, and that it will open up new areas of research in molecular imaging.

Chapter 10 Photoacoustic Imaging of Lymphatic Pumping

For the final years of my graduate studies, I was fortunate enough to be able to work for FUJIFILM VisualSonics Inc. where I could develop and use high-frequency ultrasound and photoacoustic imaging systems. During this period, I was able to work on the Vevo LAZR, a commercially available high-frequency photoacoustic imaging system, and design, develop, and enhance many aspects of the system resulting in the next generation Vevo LAZR-X photoacoustic imaging system. My work included: implementing measurements in software to reliably assess the photoacoustic signal in a sample, developing a spectral demixing algorithm and user interface for assessing the relative concentrations of molecules in a sample, evaluating a tomographic approach to collecting photoacoustic signals, working with laser manufacturers to design the next generation laser system, outlining procedures for reliable contrast agent characterization in phantom experiments and *in vivo*, optimizing software for image processing and faster hardware control of laser systems, helping customers collect and interpret data, and investigating new applications for photoacoustic imaging. Much of this work is specifically aimed at making photoacoustic molecular imaging commercially viable, reliable, and robust for customers.

With these developments, several new applications were possible using the Vevo LAZR and Vevo LAZR-X including pharmacokinetic analysis of molecular probes, characterization of untargeted and targeted nanoparticles, and imaging of the lymphatic structure and pumping with the aid of molecular probes. This chapter is dedicated to the work on lymphatic pumping that was investigated by A. Forbrich and A. Heinmiller using the improvements that I developed and implemented. This work has been accepted for publication in the *Journal of Biomedical Optics* as an article by A. Forbrich, A. Heinmiller, and R. Zemp entitled “Photoacoustic Imaging of Lymphatic Pumping” on August 15, 2017 and is presented below.

The lymphatic system is responsible for fluid homeostasis and immune cell trafficking and has been implicated in several diseases including obesity, diabetes, and cancer metastasis. Despite its importance, the lack of suitable *in vivo* imaging technique has hampered our understanding of the lymphatic system. This is, in part, due to the limited contrast of lymphatic fluids and

structures. Photoacoustic imaging, in combination with optically absorbing dyes or nanoparticles, has great potential for non-invasively visualizing the lymphatic vessels deep in tissues. Multispectral photoacoustic imaging is capable of separating the dyes and nanoparticles from background signals; however, the slow wavelength switching speed of most laser systems are inadequate for imaging lymphatic pumping without adding motion artifacts into the processed images. We investigated two approaches for visualizing lymphatic processes *in vivo*. First, single wavelength differential photoacoustic imaging is used to visualize lymphatic pumping in the hindlimb of a mouse in real-time. Second, a fast-switching multiwavelength photoacoustic imaging system was used to assess the propulsion profile of dyes through the lymphatics in real-time. These approaches may have profound impacts in non-invasively characterizing and investigating the lymphatic system. The improvements that I made to the switching speed of the laser and the implementation of a real-time demixing algorithm made these experiments easier and more reliable to perform.

10.1 Introduction

The lymphatic system, sometimes referred to as "the forgotten circulation" [46], plays a crucial role in fluid homeostasis, lipid absorption, and immune system regulation. Compared to the blood-circulatory system, the lymphatic system has a unique mechanism for pumping fluids. The peristaltic pumping actions from smooth-muscle lymphangions, as well as the blood pumping through the blood-circulatory system, help transport fluids through the lymphatic system. Many pathologies directly or indirectly involve the lymphatic system and its pumping mechanisms; often presenting as lymphatic contractile dysfunction, barrier dysfunction, and valve defects [47]. Common clinical procedures, including lymph node resection for cancer diagnostics, sometimes results in morbid complications to the lymphatic system [47, 276]. As many as 30-50% of breast cancer patients undergoing lymph node or sentinel lymph node dissection develop lymphedema [277, 278]. Despite its critical role, the lymphatic system and many of its mechanisms are poorly understood, partly due to the poor contrast of the lymphatic vessels and structures. Few imaging techniques are available to visualize the lymphatic system non-invasively *in vivo* which has significantly hampered our ability to study and understand the lymphatic system.

Lymphography, lymphoscintigraphy, magnetic resonance imaging, positron emission tomography, x-ray computed tomography, and contrast-enhanced ultrasound have all been explored for visualizing the lymphatic system [279]. These imaging techniques require exogenous

contrast agents and often are invasive, have poor spatial resolution, or have poor temporal resolution. Recently, near-infrared fluorescence imaging with indocyanine green (ICG) has been used for lymphography and visualize lymphatic propulsion and structure, non-invasively, *in vivo* [279, 280]. ICG lymphography has shown great promise for the early detection of lymphatic dysfunction [281], the assessment of lymphedema [282], and the detection of sentinel lymph nodes (the first lymph nodes that a cancer will most likely spread to from a primary tumor) [283–285]. Near-infrared fluorescence is, however, limited by light scattering and consequently poor spatial resolution at depths greater than one transport mean free path cannot resolve small lymphatic vessels.

Photoacoustic imaging is a nascent imaging technique that enables deep tissue imaging while maintaining optical absorption contrast and its utility for imaging the lymphatic system has been largely unexplored. By using an exogenous agent, such as methylene blue or ICG, photoacoustic imaging has been used to detect sentinel lymph nodes deep in tissues [49, 147, 160]. In 2014, Martel *et al.* [286] demonstrated an optical-resolution photoacoustic imaging system capable of high spatial-temporal resolution of the lymphatic system. The system was used to image the blood and lymphatic network with micron resolution and to assess the lymphatic flow. Although the optical-resolution photoacoustic imaging system shows enormous potential and presents impressive vascular and lymphatic structure, only superficial imaging was demonstrated.

To understand and study lymphatic function and mechanisms it is important to image non-invasively, deep in tissues. As acoustic-resolution photoacoustic imaging tolerates multiply scattered light, it holds significant promise for imaging lymphatic function in deep tissues with high spatial and temporal resolution. Here we report real-time single wavelength and multispectral photoacoustic imaging approaches for visualizing lymphatic pumping in murine models in the context of micro-ultrasound anatomical information co-registered with images of blood vessel networks and oxygenation maps. The system provided imaging depths of approximately 1 cm while maintaining a lateral resolution of 100 µm. Multispectral demixing is demonstrated to separate an ICG-based nanoparticle (PAtrace), Evans Blue, and oxyhemoglobin and deoxyhemoglobin at 5 frames per second, with capabilities up to 20 frames per second for a limited field of view. We believe that this system has great potential in improving our understanding of the lymphatic system, specifically lymphatic pumping. This may improve our understanding of the mechanisms that enable fluid homeostasis and immune trafficking.

10.2 Materials and Methods

Ultrasound and photoacoustic imaging was performed using either a Vevo LAZR or Vevo LAZR-X (FUJIFILM VisualSonics Inc.) imaging system. A CD-1 mouse was anaesthetized with isofluorane and setup on a platform that monitored the respiration rate and the heart rate of the mouse. The hair on the hindlimb of the anaesthetized mouse was removed. A 27G needle catheter was position in the footpad of the mouse for injection of the contrast agent. A 30 MHz, linear array ultrasound transducer with integrated fiber optic light delivery (LZ-400 and MX-400, FUJIFILM VisualSonics, Inc.) was positioned longitudinally overtop the hindlimb. Ultrasound imaging was used to make sure that the popliteal lymph node was in the field-of-view. Figure 10.1 shows the position of the needle catheter and the imaging plane. Initially to visualize lymphatic pumping, photoacoustic imaging was performed at 680 nm before, during, and after a 15 µL bolus injection of either 1.0 mg/mL methylene blue or 0.1 mg/mL ICG. Image subtraction using pre-injection reference images was used to highlight signal changes within the image. After the injection, the transducer was scanned laterally while performing multiwavelength imaging on the same animal to reconstruct a three-dimensional image of the methylene blue and ICG-stained lymph node.

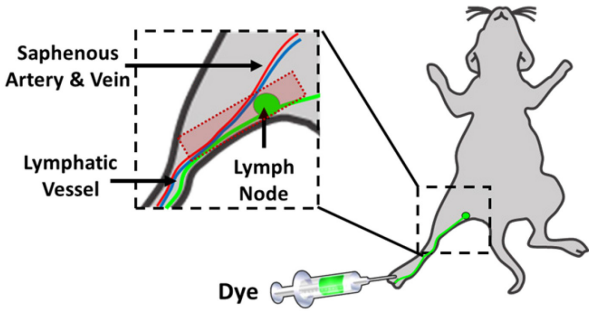

Figure 10.1 Injection site and imaging plane for visualizing lymphatic pumping. Dye was injected through a 27G needle catheter placed into the top of the footpad. Ultrasound and photoacoustic imaging was done longitudinally along the hindlimb (as shown in the red-shaded rectangle) such that the popliteal lymph node was visible.

Another set of experiments performed multiwavelength imaging at 680, 730, 760, 800, 830, 850, 900, 950, and 970 nm on a mouse while the mouse was injected with a 15 µL bolus of a mixture of Evans Blue (0.1 mg/mL) and PAtrace (NanoHybrids, Inc. Austin Texas, 0.1 mg/mL). PAtrace is a nanoparticle composed of J-aggregates of ICG encapsulated and stabilized by a proprietary biocompatible shell. The shell is PEGylated to enhance circulation time in biological fluids. PAtrace has a neutral, or near zero, zeta potential due to PEG; it is 90 ± 20 nm in diameter with an

absorbance maxima at 892 nm. Using the multiwavelength images, the relative concentration of PAtrace, Evans Blue, deoxyhemoglobin, and oxyhemoglobin were demixed using pseudo-inverse algorithms available on the Vevo LAZR-X system. The absorption spectra of these components are seen in Figure 10.2. All animal experiments were conducted in accordance to the protocols set out by the Animal Care and Use Committee at FUJIFILM VisualSonics Inc.

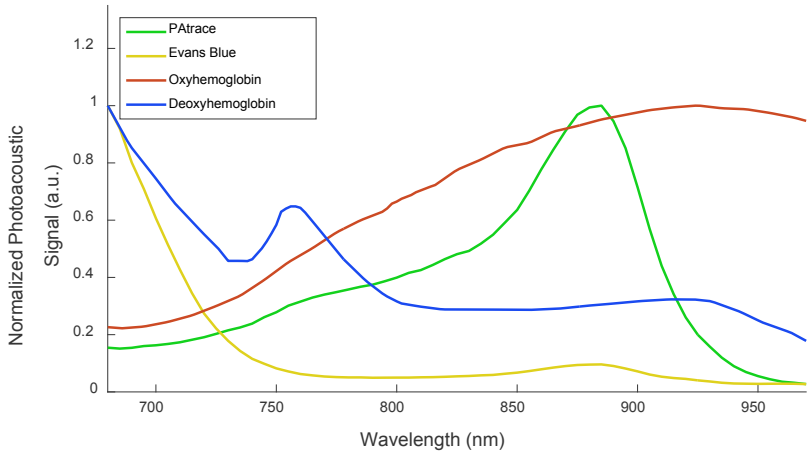

Figure 10.2 Normalized absorption spectra from PAtrace (green), Evans Blue (yellow), oxyhemoglobin (red), and deoxyhemoglobin (blue). The curves for oxyhemoglobin and deoxyhemoglobin are plotted from data compiled by S. Prahl [142].

10.3 Results and Discussion

Longitudinal photoacoustic imaging of the hindlimb during a 15 µL bolus injection of 1.0 mg/mL methylene blue into the footpad of the mouse was used to visualize the flow dynamics of the dye through the lymphatic system. Initially, single wavelength imaging was used to eliminate the temporal overhead of switching wavelengths and achieve the maximum frame rate of 5 Hz for full-width imaging using the Vevo LAZR imaging system (Figure 10.3). Although a significant increase in photoacoustic signal was clearly visible in the popliteal lymph node (Figure 10.3A), the location of the dye throughout the image was difficult to assess. Using a series of reference frames taken prior to injection, a difference image was formed that highlighted the change in signal (Figure 10.3B,C). The image sequence revealed that dye accumulation occurred in the lymph node indicating that the dye was indeed being transported through the lymphatic system. The change in photoacoustic signal within regions that represented the popliteal lymph node, efferent and afferent lymphatic vessels, as well as the perilymph node clearly demonstrated the pulsatile nature of the signal within these structure (Figure 10.3D,E). This periodicity of the pulse in the

afferent lymph node ranged from 1.5 to 7 pulses per minute and did not appear to be correlated to the ECG signals (360-380 beats per minute) or the respiration rate (35-45 breaths per minute) which further indicates that the dyes were being transported through the lymphatic system. The lymphatic pumping rate that we observed is similar to those report by Kwon and Sevick-Muraca who observed a rate of 0.72 to 11.1 pulses per minute [287]. Additionally, the measurements clearly demonstrated that the photoacoustic signal within the lymph node increased after each pulse through the afferent lymphatic vessel indicating the accumulation of methylene blue in the lymph node. As expected since methylene blue stains lymph nodes, after 10 minutes the signal in the lymph node was relatively constant.

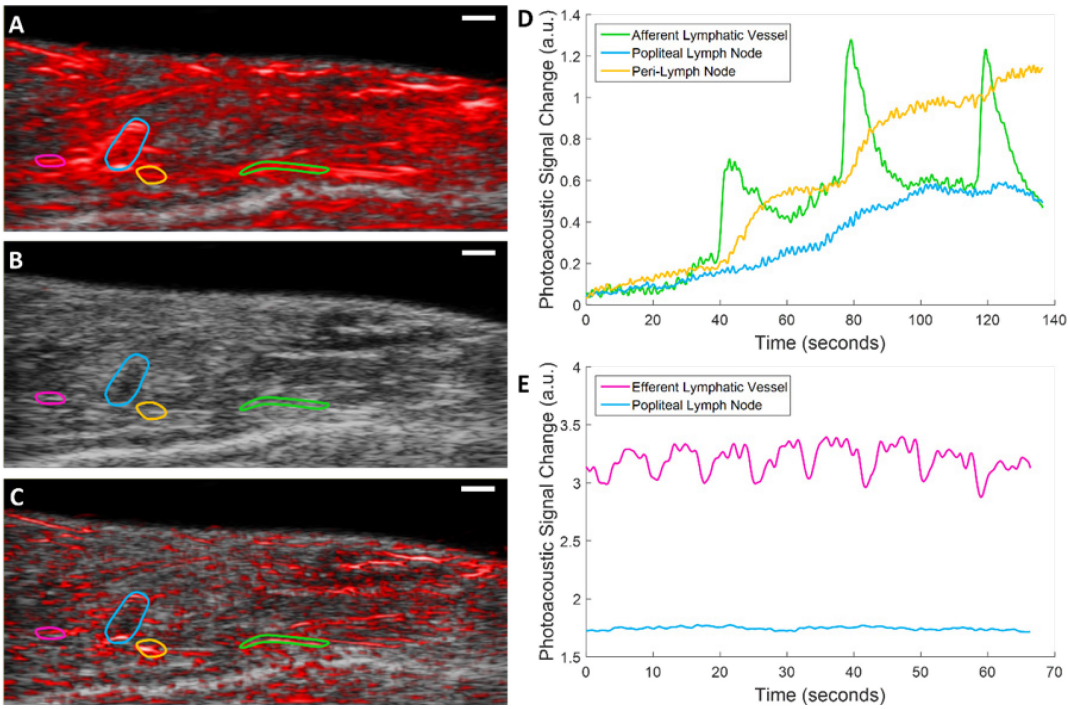

Figure 10.3 Photoacoustic imaging of the popliteal lymph node during an injection of 1.0 mg/mL methylene blue. Interlaced ultrasound (gray colormap) and photoacoustic (red colormap) imaging of the hindlimb: (A) reference frame for image subtraction, (B) prior to injection, and (C) after injection. The photoacoustic signal in (B) and (C) has the baseline photoacoustic signal removed by subtracting the reference frames. Regions of interest were created surrounding an afferent lymphatic vessel (green), the peri-popliteal lymph node (orange), the popliteal lymph node (blue), and an efferent lymphatic vessel (pink). White scalebar represents 1 mm. (D) Change in the photoacoustic signal during an injection of methylene blue. (E) Change in the photoacoustic signal in the efferent vessel 10 minutes after the injection.

To validate the demixing capabilities of the Vevo LAZR imaging system for lymphatic imaging, another mouse was used and injected with 15 µL of 0.1 mg/mL ICG into the footpad. A three-dimensional multiwavelength photoacoustic imaging was conducted by laterally moving the LZ-400 transducer at a step size of 0.2 mm over a distance of 5 mm. A constrained pseudo-inverse demixing algorithm was used to separate deoxyhemoglobin, oxyhemoglobin, and ICG. Figure 10.4 shows a three-dimensional rendering of the hindlimb with blood shown in red and ICG shown in green. The lymphatic vessel and popliteal lymph node are clearly visible.

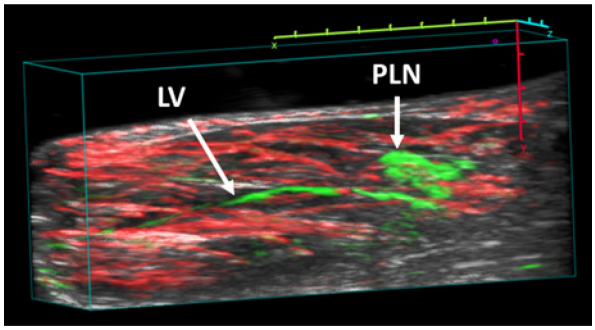

Figure 10.4 Three-dimensional multispectral photoacoustic image demixed for ICG. The gray, red, and green colormaps represent the ultrasound signal, blood, and relative ICG concentration, respectively. The ICG is isolated to the lymphatic vessel (LV) and the popliteal lymph node (PLN). Scalebar represents 1 mm per tick.

As demonstrated in Figure 10.4 multiwavelength studies are important to accurately separate the dyes from background signals such as blood. For longitudinal studies, it is important to image quickly at each wavelength to avoid the motion artifacts or, more importantly for these experiments, fluid flow. Using the Vevo LAZR software, the wavelength switching speed takes several hundreds of milliseconds which may affect these measurements. Since the Vevo LAZR-X has shot-to-shot wavelength-switching capabilities, a higher temporal resolution is achievable potentially increasing the accuracy of spectral demixing. Multiwavelength longitudinal photoacoustic imaging was performed during two separate injections of a mixture of Evans Blue and PAtrace. Figure 10.5 represents the results during the second injection. It is interesting to note, that longitudinal images showed a different propulsion profile for the two different types of dyes. In the afferent lymphatic vessel, the PAtrace showed a more discrete propulsion profile compared to Evans Blue. The estimated concentration of Evans Blue gradually increased over time, whereas the estimated concentration of PAtrace changed in bursts and seemed to move between different compartments along the lymphatic vessel which may be indicative of the

lymphangions in the vessel. Although the difference in pumping rates is not well understood, it may be due to the lipophilic nature of the PAtrace nanoparticle compared to the hydrophilic nature of Evans Blue and the high affinity of Evans blue to serum albumin. As this was the second injection of the contrast agents, it is noteworthy that the PAtrace nanoparticle seemed to remain in the lymph node while the Evans Blue did not significantly stain the lymph node. Further evidence that the Evans Blue did not significantly stain the lymph node is indicated by the decreasing concentration of Evans Blue over time.

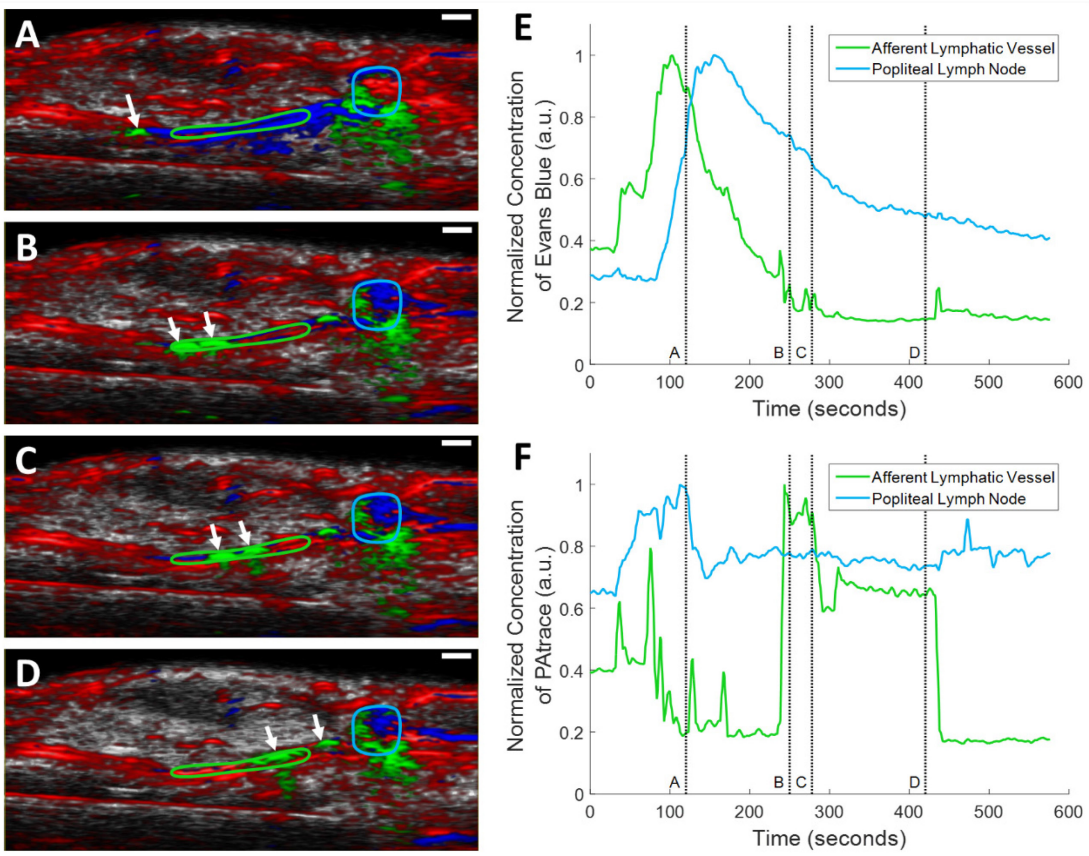

Figure 10.5 Demixed photoacoustic image of lymphatic pumping in the hindlimb of a mouse. Evans Blue and PAtrace were co-injected into the footpad of a mouse. (A-D) represent still frames during the injection at 120, 250, 280, 420 seconds, respectively. The relative concentration of PAtrace, Evans Blue, and blood is presented as the green, blue, and red colormaps, respectively. The white scalebar represents 1 mm. (E) Relative demixed concentrations estimates of Evans Blue in the afferent lymphatic vessel (green) and the popliteal lymph node (blue). (F) Relative concentration estimates of PAtrace in the afferent lymphatic vessel (green) and the popliteal lymph node (blue). The timepoints for the still frames are marked by vertical lines in (E) and (F).

This research represents one of the first reports using a commercial, high-resolution photoacoustic imaging system to visualize lymphatic pumping at depths 3-5 mm deep. With this system and the LZ-400 or MX-400 (18-38 MHz linear array transducer), we were able to image 150-250 μm diameter lymphatic vessels 3.5 mm deep in tissues. Although optical-resolution photoacoustic imaging has been used to visualize much smaller lymphatic vessels with higher resolution, the depth capabilities of such systems are substantially limited [286]. Planar fluorescent imaging is capable of deep imaging, however, the spatial resolution of the system presented here (110 μm) is significantly finer than fluorescent imaging at comparable depths. Finally, our field-of-view is more limited than intensified CCD camera-based near-infrared imaging; however, our approach provides volumetric depth resolution imaging capabilities.

Since these experiments used bolus injections of the dyes, there may have been higher pressures in the lymphatic system causing more rapid drainage initially. Additional studies should investigate lymphatic pumping and flow using a slow, continuous intradermal injection of the dye. More work is needed to understand the reason for the differing pumping rates of dyes.

Future work should consider combining the wide field-of-view of intensified near-infrared CCD imaging of lymphatic flow [279, 280] with the presented high-resolution depth-resolved system for a more detailed view of lymphatic regulation and dysfunction. Future work should also focus on improving depth of imaging for clinical applications, where lymph nodes can be deeper in tissues. This should be possible given recent demonstrations of photoacoustic imaging at multiple-centimeter depths using lower-frequency transducers. The present study using high-frequency ultrasound transducers is well-suited to pre-clinical applications.

Given so many unanswered questions about the lymphatic system, we believe this new approach may provide a novel toolset for investigating lymphatic function. This may lead to image-guided intervention to mitigate some morbid side-effects of lymph node resection. It may also contribute to new research capabilities for treating lymphedema and related diseases and may improve our understanding of lymphatic system pathogenesis.

10.4 Conclusion

We have demonstrated photoacoustic imaging of lymphatic pumping with 110 μm resolution at depths of up to 5 millimeters. The system is capable of shot-to-shot wavelength switching enabling multiwavelength, spectroscopic imaging of PAtrace, Evans Blue, and methylene blue at

frame rates suitable for imaging peristaltic flow in lymphatic vessels. These capabilities may enable new toolsets for researchers and clinicians in understanding and treating lymphatic disorders.

The advances that I contributed to the Vevo imaging system enabling this research may prove valuable for many researchers. Specifically, my advancements in the spectral demixing algorithms and wavelength control have allowed high frame rate multiwavelength imaging and have recently been incorporated into the next generation photoacoustic imaging system at FUJIFILM VisualSonics Inc. – the Vevo LAZR-X.

Chapter 11 Future and Conclusion

In summary, we demonstrated using ultrasound and photoacoustic imaging for a variety of molecular imaging application with several novel image contrast mechanisms. We wanted to address the problem statement:

> *How much new molecular information can be extracted using combined ultrasound and photoacoustic imaging systems?*

Key related questions that we investigated included:

1. Can ultrasound be used to release biomarkers from cells into body fluids for liquid biopsies?
2. Can we use exogenous contrast agents, dyes, or genetically-encoded reporters for multimodality molecular imaging with new contrast mechanisms?

We have made important contributions to address these questions. In particular, for the first time we demonstrated:

1. Ultrasound treatment releases nucleic acid biomarkers from cells.
2. Ultrasound-aided biomarker liberation is substantially enhanced by microbubbles and phase-change nanodroplets.
3. Visualization of the phase-change events such as nanodroplet vaporization and microbubble destruction.
4. Multi-modality phase-change nanodroplets that provide photoacoustic contrast in the liquid form and ultrasound and photoacoustic contrast in the microbubble form.
5. Novel photoacoustic-based directed evolution screening techniques for optimizing reporter proteins for photoacoustic imaging.
6. Novel image sequence for creating excited-stated lifetime-weighted photoacoustic images.
7. Estimation of ground-state recovery lifetimes using photoacoustic imaging.
8. New ultrasound and photoacoustic imaging system used for visualization of lymphatic pumping using exogenous contrast agents.

These contributions contribute to the vision proposed in Chapter 1 of using molecular imaging to molecularly profile target tissues then amplifying blood-biomarkers from these tissues.

Some of the work initiated in this dissertation has been continued by other team members. A noteworthy example is Paproski *et al. Cancer Research* 2016, which demonstrated two orders of magnitude enhancement of extracellular vesicles populations in blood using ultrasound and nanodroplet treatment [32]. Additionally, two-orders of magnitude more genetic information was identified post-ultrasound treatment compared to the pre-ultrasound baselines. Panels of tumor-specific mutations were identified, some of which are linked to aggressive phenotypes.

11.1 Future Work

11.1.1Liquid Biopsies and Biomarker Enhancement

Thus far, our *ex vivo* experiments have demonstrated the utility of microbubbles and nanodroplets for enhancing nucleic acid biomarker liberation. One of the main limitations of the work presented in Chapters 3-6 was that only one mRNA and one miRNA biomarker were investigated. Single biomarkers only have limited utility for accurately assessing disease characteristics. For example, PSA is not specific to aggressive tumors resulting in an over diagnosis of prostate cancer [8]. As this was a proof-of-concept investigation extending the work demonstrated by D'Souza [28], it was acceptable to examine one or two biomarkers for proof-of-principle; however, it will be necessary to analyse other biomarkers in future work. Ideally, whole panels of biomarkers can be used for diagnostics to increase specificity and reliability.

Currently, there have been worldwide efforts to search for new biomarkers to increase the specificity and reliability for liquid biopsies. It is possible that during this investigation many potential liquid biomarkers have been overlooked due to low concentration, non-specificity to tissue type, or low stability. It is our belief that ultrasound treatment with ultrasound contrast agents could overcome many of these challenges, increasing the usability of many liquid biomarkers that were previously not considered. Additional *ex vivo* and *in vivo* ultrasound-aided biomarker liberation experiments in conjunction with high-throughput proteomic and genomic techniques should be conducted to analyse biomarkers that were previously eliminated due to low concentration or non-specificity. Furthermore, the biomarkers found in the micro-vesicles released from cells when exposed to ultrasound contained more stable biomarkers [32]. These biomarkers should be analysed further and may increase the number of clinically-relevant

biomarkers available to clinicians for diagnostic and prognostic purposes. In a recent study, our group showed that a panel of 13 tumor-specific mutations were detectable in DNA fragments found following ultrasound treatment and that these were not detectable without the ultrasound treatment [32]. This study also demonstrated enhancement of DNA and RNA biomarkers by two to three orders of magnitude compared to no ultrasound treatment.

Our results showed that both microbubbles and nanodroplets were capable of enhancing the ultrasound-aided biomarker liberation. Microbubbles have been developed for the clinic; however, nanodroplets have only recently been developed and there needs to be concentrated effort to develop nanodroplets for the clinic and assess their pharmacokinetics and lifetime in animals and humans. The porphyrin-based nanodroplets used in some of our research [39] has potential for clinical use as it is composed of biologically compatible, organic molecules. Combining the multispectral photoacoustic imaging techniques described in this dissertation with the porphyrin-based nanodroplets will allow researchers and clinicians to verify when the nanodroplets are in close proximity to the tissue of interest. This would allow the scientists to (a) determine when to phase-change the nanodroplets and (b) evaluate the efficacy of biomarker liberation. Further development is required to understand how close the nanodroplets need to be to effectively release biomarkers when exposed to ultrasound.

Targeted microbubbles and nanodroplets may further enhance biomarker liberation. With targeting, the concentration of the contrast agents will increase and the contrast agents will be inherently closer to the cell wall. Future work should focus on developing targeted contrast agents and examine the impact on biomarker liberation. When using targeted contrast agents, there is a presupposition by the researcher that the tissue of interest will display the targeted receptor. Therefore, ultrasound-enhanced biomarker liberation with targeted receptors would benefit greatly from imaging with both ultrasound and photoacoustic imaging. The accumulation (or lack of accumulation) of the contrast agents would give additional insight into the characteristics of a disease.

As mentioned in the previous two paragraphs, there may be great benefit in integrating an ultrasound and photoacoustic imaging setup with the biomarker liberation procedures. This would help indicate when a contrast agent reaches the tissue of interest. The clinical limit for diagnostic ultrasound is 0.72 W/cm^2 and our results demonstrate that pulses below 0.72 W/cm^2 can release substantial amounts of biomarkers when certain ultrasound contrast agents are used.

However, the duty cycle of these biomarker liberation pulses is very high and most clinical systems cannot support this due to thermal limits. Future developments should also focus on developing clinical ultrasound systems capable of imaging and delivering the high duty cycle pulses.

There are several challenges when translating these techniques to humans. First, the volume of blood in a human is substantially more than that in our *in vitro* and some of our preliminary *in vivo* work. This would dilute any biomarkers liberated and make them harder to detect in liquid biopsies. Since the number of cells we investigated was fairly small, it may be possible that small tumors may release enough biomarkers to be detectable. Additionally, some biomarkers are in very high concentration in cells (for example, miR-21) that they may be still detectable in blood. Future work needs to address this and determine the size of tumors that could be analysed reliably and to determine suitable biomarkers for diagnostics and prognostics. Second, it is often very difficult and time consuming to introduce completely new systems into the clinic. Future work should address whether clinically approved microbubbles and clinical ultrasound systems could be used for biomarker liberation studies. This would greatly accelerate translation to the clinic as microbubbles and diagnostic ultrasound systems are both widely used and clinically approved. Third, there may be many different tissues nearby the tissue of interest, which will cause ambiguity in the biomarkers detected in liquid biopsies. Using MRI to guide ultrasound to the tissue of interest may be an important step to limiting the exposure of ultrasound to nearby tissues. Future direction needs to assess the viability of discriminating between tissues and the utility of MRI-guided ultrasound to localize biomarker liberation.

Finally, as previously mentioned, micro-vesicles containing many biomarkers are released from cells when exposed to ultrasound [32]. Future work should also investigate methods for enhancing extracellular vesicle populations using surface-markers. This is important as there may be vast numbers of vesicles in the body from other tissues. Additionally, the micro-vesicles have been shown to contain DNA and RNA. Previously, DNA and RNA were either too unstable in liquid biopsies or too low in concentration to detect. This new source of biomarkers opens up many avenues of research and many questions exist about how to use this new information for diagnostics and prognostics.

11.1.2 Flash-Difference Imaging

In Chapter 7, we briefly discussed how ultrasound and photoacoustic imaging could be used to visualize nanodroplets and various phase-change events. As previously discussed, imaging of

phase-change events such as microbubble destruction or nanodroplet vaporization may become an important component of the ultrasound-aided biomarker liberation procedure enabling the assessment of liberation efficacy and contrast agent-tissue proximity. This technique may also be important for assessing drug delivery from microbubbles and nanodroplet vesicles non-invasively. For drug delivery, it is important that the therapeutic is released only to the desired tissue. Future work should investigate using the phase-change imaging to validate and assess drug delivery from microbubble and nanodroplet vesicles non-invasively.

Although the work presented in this dissertation used acoustic energy to induce phase-change events in the microbubbles and nanodroplets, it has been shown that optical energy can be used to phase-change contrast agents that have optically-absorbing molecules integrated into the lipid shell. For photoacoustic imaging of liquid nanodroplets, it will be important to use an appropriate intensity of light to (a) have good SNR from the contrast agents and (b) prevent phase-change events from occurring prematurely. Future studies should also investigate the fluence required to phase-change these contrast agents. Additionally, pulse sequences should be developed to integrate a light pulse instead of an acoustic pulse as the inducer of phase-change events. This would enable the investigation of light-induced phase-change events.

When designing phase-change contrast agents, it is important to understand the acoustic parameters (or optical parameters) necessary to induce a phase-change while minimizing the damage to surrounding tissues. Additionally, loading contrast agents with therapeutics or adding targeting ligands to the lipid shell may also affect the response of the tissues to acoustic and optical energy. The flash-difference imaging pulse sequences may be useful in studying these effects and future studies should be developed to enable the characterisation of these acoustic (or optical) parameters.

The experimental setup used to demonstrate the flash-difference imaging required an external transducer and precise alignment to setup. Ideally, it would be preferable to have the excitation pulse originate from the imaging transducer. The Verasonics system has a high-power option that can be integrated into the flash-difference pulse sequence; however, thermal and safety concerns must be examined, especially for clinical use. Future studies should investigate using the Verasonics system for both phase-changing and imaging of the nanodroplets. Photoacoustic imaging could also be integrated into this setup.

For high resolution imaging, high frequency array transducers can be used; however, the mechanical index decreases with increasing frequency. Additionally, many ultrasound contrast agents have a low resonance frequency (1-4 MHz). Both the increase in imaging frequency and low resonance frequency mean that a more intense pulse is required to induce the phase-change events. Specialized dual-frequency transducers should be investigated for flash-difference imaging to (a) phase-change with low frequency and (b) image with high frequency ultrasound.

Since this technique is similar to many other plane-wave techniques that have been recently been developed, flash-difference imaging should be integrated with other functional high-frame rate techniques such as ultrafast Doppler, elastography, and shear wave imaging [288, 289]. Future studies should investigate how much additional functional information could be combined with flash-difference imaging.

11.1.3Directed Evolution of Photoacoustic Proteins

Chapter 8 demonstrated a screening technique to evolve reporter proteins for photoacoustic imaging. The screening technique optimized the photoacoustic signal by increasing the extinction coefficient and by decreasing the fluorescent quantum yield. One application of the Ultramarine and cjBlue variants that we evolved with our screening technique is for bacterial infection. Since these proteins express very well in bacterial cells, these proteins could be used to study bacterial infection and to monitor therapeutic response non-invasively deep in tissues. Monitoring bacterial infection and treatment is extremely important as infections are sometimes a complication of surgical procedures.

Aside from optimizing the extinction coefficient and fluorescent quantum yield, there are many other features of a protein that could be evolved to enhance photoacoustic imaging. Red-shifting the absorption peak of the protein would be beneficial for photoacoustic imaging as near-infrared light is scattered less in tissues and can result in deeper imaging. This would most likely involve imaging at two wavelengths and using a ratiometric measure between the higher and lower wavelengths to select the best red-shifted protein. Experiments should be designed to validate this concept. Other properties of a protein that may be important for photoacoustic imaging include increasing the maturation rate, decreasing the toxicity, and increasing the photostability of the proteins. Further studies are necessary to optimize each of these aspects.

Although the work developed in this dissertation only focused on optimizing two chromoproteins for photoacoustic imaging, this technique could be extended to many other chromoproteins such as near-infrared absorbing proteins and photo-switchable proteins. Near-infrared absorbing proteins are important for imaging deeper with optical and photoacoustic imaging as light can penetrate better at the near-infrared wavelength range. Photo-switchable proteins can change their absorption spectra when exposed to specific wavelengths of light. Improved photo-switchable chromoproteins may offer great promise for imaging with reduced endogenous background similar to Yao *et al.* [290]. Imaging and evolving photo-switchable proteins may benefit from a similar imaging pulse sequence as used for lifetime-weighted imaging. The pump pulse could be used to change the absorption spectra and the probe pulse could be used to image the new absorption spectrum of the protein. Differential imaging would be used to highlight the photo-switchable proteins while nullifying background signals. Future work should investigate evolving other types of proteins including near-infrared proteins and photo-switchable proteins.

FRET-based reporters were briefly discussed in Chapter 8. We used the enhanced variants that were evolved from Ultramarine in these constructs which showed the FRET effect; however, since FRET was not the initial goal the results were not optimal. The screening protocol could be altered to try to optimize a FRET-construct specifically for photoacoustic imaging. This should be investigated with near-infrared proteins to enable FRET-based reporters for near-infrared photoacoustic imaging deep in tissues. Some of this proposed research has been continued and presented at recent conferences [291].

Fluorescent calcium-sensitive biosensors have revolutionized our ability to visualize and investigate brain function. Similar photoacoustic calcium-sensitive biosensors should be investigated. Currently, our lab is developing systems to image calcium-based reporters for photoacoustic imaging of neuronal signaling. Protein development for this work is being performed by Dr. Campbell's lab at the University of Alberta. This work will enable deeper, non-invasive imaging of brain function and may help scientists further unravel the mysteries of the brain.

Much of the directed evolution used *E. coli* to ensure single plasmid transfection for clonal selection; however, mammalian cell expression can be vastly different. Future work should investigate methods for optimizing mammalian cell reporter gene expression. One extension of this work is to develop transgenic animal models that express the photoacoustic protein. One

application for transgenic animal models could be for immunotherapy, which has received great interest recently. Immunotherapy is a treatment that boosts the natural immune system to fight disease and has been demonstrated in animal models. Unfortunately, the response rate in animals is low and verification of treatment response can only be done through terminal procedures after a lengthy longitudinal study [292]. Developing transgenic animal models where the immune cells contain photoacoustic proteins may be one method to visualize the immune response non-invasively *in vivo*. Transgenic animals expressing evolved photoacoustic proteins need to be developed for studying immune response and other biological processes.

One of the challenges with photoacoustic imaging of calcium-sensitive proteins and protein expression in mammalian cells is the sensitivity of the photoacoustic imaging platform. The proteins that we have imaged are cytoplasmic and can have high concentrations in bacterial cells, which resulted in quite high SNR. Calcium-sensitive proteins are typically membrane-bound and present in low concentration. Similarly, mammalian cells tend to express these proteins in much lower concentrations. Additional work is also required to improve instrumentation with the goal of cellular resolutions in deep tissue.

11.1.4Lifetime-Weighted Imaging

In Chapter 9, we presented the theory behind lifetime-weighted imaging using simple 3+1 energy level diagrams and presented a few proof-of-principle experimental images. As an extension to existing work on lifetime-based photoacoustic imaging [44], we presented lifetime imaging and estimation of partial pressure of oxygen using a new photoacoustic contrast agent, porphyrins. Porphyrins have great utility for photoacoustic imaging and since they are an organic, biocompatible molecule, they may have some utility in a clinical environment. Additional experiments need to further validate porphyrins for estimating the partial pressure of oxygen in samples. Furthermore, the 3+1 energy state model for porphyrins needs to be validated or expanded.

The ground-state and excited-state lifetimes of molecules can be affected by more than just the partial pressure of oxygen. Other analytes such as calcium ions, as well as the pH of the surrounding environment can also affect the lifetime. Future studies should look at other lifetime-dependent molecules to examine other environmental factors. This may be beneficial in animal models in order to visualize multiple environmental factors simultaneously and non-invasively deep in tissues.

In vivo imaging is also necessary to validate the utility of this pulse sequence with porphyrins in tissues. One of the challenges for porphyrins is that porphyrins have a relatively short lifetime (1-5 μs). This may result in photoacoustic signals from the pump and probe beam overlapping. Alternative pulse sequences may be necessary and should be investigated to overcome this issue. Some groups have used a sequence of four pulses: a pump-probe pulse pair, a pump pulse, and a probe pulse [271]. With a very short time separation, this type of sequence can help with the overlapping signal issue by subtracting out the signal due to the pump and the signal to the probe resulting in only the signal due to the probe after a pump pulse. For *in vivo* experiments, combining the lifetime-weighted imaging techniques and the flash-difference imaging for porphyrin-based nanodroplets should be examined. This would enable high contrast imaging of the condensed liquid form of the nanodroplets and mapping of the phase-change events.

It would be interesting to also study multiple types of lifetime-dependent molecules. Targeted, spectrally distinct molecules such as methylene blue and porphyrins could be mixed and injected into animals. Multispectral imaging and the spectral demixing techniques described throughout this dissertation, as well as the lifetime-weighted imaging could give additional functional information deep in tissues. Experiments should be designed to validate this and determine the best methods to characterize tissues based on this information.

11.1.5Lymphatic Imaging

The work presented in Chapter 10 demonstrates the feasibility of imaging the lymphatic system and lymphatic pumping with high-resolution photoacoustic imaging in deep tissues. This is of great importance, as currently there are few imaging modalities capable of visualizing the lymphatic system non-invasively, with high-resolution, and deep in tissues. While the imaging was conducted in a healthy mouse, it would be valuable to test the utility of photoacoustic imaging on a mouse with a lymphatic disorder. Future studies should use animal models with lymphatic disorders such as lymphedema, obesity, or inflammatory bowel disease. Studies should also be developed to investigate the utility of photoacoustic imaging to visualize and understand the three main causes of lymphedema: contractile dysfunction, barrier dysfunction, and valve defects. It may be necessary to develop unique contrast agents to visualize each of these three main causes.

Transgenic animal models may also help increase our understanding of the lymphatic system. For example, the lymphatic system is responsible for immune cell trafficking. If the immune cells in

an animal could be designed to express a photoacoustic reporter protein, then photoacoustic imaging could visualize the movement of cells to tumors and diseases, and may give another method to further investigate the immune response in organisms. Additionally, we found that PAtrace moved in bursts through lymphatic vessels. Although we believe this is due to the lipophilic nature of the ICG-based nanoparticle, it may also be due to the endocytosis of the nanoparticles by macrophages and the traveling of macrophages through the lymph vessels. Future studies should investigate transgenic animals. Additionally, other functions of the lymphatic system such as lipid absorption could be investigated. The proteins developed from the directed evolution techniques described in this dissertation may increase the sensitivity of photoacoustic imaging for this application.

Lymphatic imaging may also be important for clinical applications. For example, lymph node resections often have morbid side-effects. Photoacoustic imaging of the lymphatic system may guide surgeons away from the lymphatic vessels or other structures reducing the risk of these morbid side-effects. One method that may reduce the number of lymph nodes resections would be to co-inject a targeted and a nontargeted nanoparticle into the lymphatic system. By using multispectral imaging, the two nanoparticles could be separated and with longitudinal imaging a clinician would be able to distinguish between nonspecific and targeted binding of these nanoparticles. With this technique, photoacoustic imaging may be able to distinguish lymph nodes with or without metastatic tumor cells. This would guide surgeons to only resect lymph nodes with diagnostically relevant information. Although this approach is far off, studies should be conducted to (a) develop nanoparticles for photoacoustic lymphatic imaging and (b) investigate visualizing and distinguishing tumor-cell positive and negative lymph nodes.

11.2 Outlook

We believe that ultrasound and photoacoustic imaging techniques have significant potential for elucidating molecular biology *in vivo*, for enhancing diagnostic and prognostic assessments, and for opening new avenues of genetic profiling to enable next generation personalized medicine approaches. The developments illustrated in this dissertation contribute to this long-term vision.

Bibliography

[1] A. Mordente, E. Meucci, G. Martorana, and A. Silvestrini. Cancer biomarkers discovery and validation: State of the art, problems and future perspectives. *Adv. Exp. Med. Biol.*, 867, pp. 9–26, 2015.

[2] S. Yotsukura and H. Mamitsuka. Evaluation of serum-based cancer biomarkers: A brief review from a clinical and computational viewpoint. *Crit. Rev. Oncol. Hematol.*, 93(2), pp. 103–115, 2015.

[3] M. Pavlou, E. Diamandis, and I. Blasutig. The long journey of cancer bBiomarkers from the bench to the clinic. *Clin. Chem.*, 59(1), pp. 147–157, 2013.

[4] S. Saini. PSA and beyond: alternative prostate cancer biomarkers. *Cell. Oncol.*, 39(2), pp. 97–106, 2016.

[5] B. Calhoun and L. Collins. Predictive markers in breast cancer: An update on ER and HER2 testing and reporting. *Semin. Diagn. Pathol.*, 32(5), pp. 362–369, 2015.

[6] C. Ma, R. Bose, and M. Ellis. Prognostic and predictive biomarkers of endocrine responsiveness for estrogen receptor positive breast cancer. *Adv. Exp. Med. Biol.*, 882, pp. 125–154, 2016.

[7] S. Chatterjee and B. Zetter. Cancer biomarkers: Knowing the present and predicting the future. *Futur. Oncol.*, 1(1), pp. 37–50, 2005.

[8] W. Tabayoyong and R. Abouassaly. Prostate cancer screening and the associated controversy. *Surg. Clin. North Am.*, 95(5), pp. 1023–1039, 2015.

[9] F. Shahneh. Current challenges in metastasis: Disseminated and circulating tumor cells detection. *Hum. Antibodies*, 22(3–4), pp. 77–85, 2013.

[10] M. James and S. Gambhir. A molecular imaging primer: Modalities, imaging agents, and applications. *Physiol. Rev.*, 92(2), pp. 897–965, 2012.

[11] L. Griffeth. Use of PET/CT scanning in cancer patients: Technical and practical considerations. *Proc. (Bayl. Univ. Med. Cent).*, 18(4), pp. 321–330, 2005.

[12] B. Forster *et al.* Functional magnetic resonance imaging: The basics of blood-oxygen-level dependent (BOLD) imaging. *Can. Assoc. Radiol. J.*, 49(5), pp. 320–329, 1998.

[13] G. Glover. Overview of functional magnetic resonance imaging. *Neurosurg. Clin. N. Am.*, 22(2), pp. 133–139, 2011.

[14] J. Willmann *et al.* US imaging of tumor angiogenesis with microbubbles targeted to vascular endothelial growth factor receptor type 2 in mice. *Radiology*, 246(2), pp. 508–518, 2008.

[15] R. Y. Tsien. The green fluorescent protein. *Annu. Rev. Biochem.*, 67, pp. 509–544, 1998.

[16] W. Becker. Fluorescence lifetime imaging - Techniques and applications. *J. Microsc.*, 247(2), pp. 119–136, 2012.

[17] J. R. Lakowicz. *Principles of Fluorescence Spectroscopy*. New York: Springer Science + Business Media, 2010.

[18] L. V. Wang and H. Wu. *Biomedical Optics: Principles and Imaging*. Wiley-Interscience, 2007.

[19] P. Beard. Biomedical photoacoustic imaging. *Interface Focus*, 1(4), pp. 602–631, 2011.

[20] S. Wilson and P. Burns. Microbubble-enhanced US in body imaging: What role? *Radiology*, 257(1), pp. 24–39, 2010.

[21] A. Klibanov *et al.* Detection of individual microbubbles of ultrasound contrast agents: Imaging of free-floating and targeted bubbles. *Invest. Radiol.*, 39(3), pp. 187–195, 2004.

[22] W. Pitt, G. Husseini, and B. Staples. Ultrasonic drug delivery - A general review. *Expert Opin. Drug Deliv.*, 1(1), pp. 37–56, 2004.

[23] A. Bell. On the production and reproduction of sound by light. *Am. J. Sci.*, s3-20(118), pp. 305–324, 1880.

[24] J. Weber, P. Beard, and S. Bohndiek. Contrast agents for molecular photoacoustic imaging. *Nat. Methods*, 13(8), pp. 639–650, 2016.

[25] X. Wang, X. Xie, G. Ku, L. Wang, and G. Stoica. Noninvasive imaging of hemoglobin concentration and oxygenation in the rat brain using high-resolution photoacoustic tomography. *J. Biomed. Opt.*, 11(2), p. 24015, 2006.

[26] J. Xia, J. Yao, and L. Wang. Photoacoustic tomography: Principles and advances. *Electromagn. waves (Cambridge, Mass.)*, 147, pp. 1–22, 2014.

[27] J. Laufer, A. Jathoul, M. Pule, and P. Beard. In vitro characterization of genetically expressed absorbing proteins using photoacoustic spectroscopy. *Biomed. Opt. Express*, 4(11), pp. 2477–2490, 2013.

[28] A. D'Souza *et al.* A strategy for blood biomarker amplification and localization using ultrasound. *Proc. Natl. Acad. Sci. U. S. A.*, 106(40), pp. 17152–17157, 2009.

[29] A. Forbrich, R. Paproski, M. Hitt, and R. Zemp. Microbubble-enhanced ultrasound liberation of mRNA biomarkers in vitro. *Ultrasound Med. Biol.*, 39(6), pp. 1087–1093, 2013.

[30] A. Forbrich, R. Paproski, M. Hitt, and R. Zemp. Comparing efficiency of micro-RNA and mRNA biomarker liberation with microbubble-enhanced ultrasound exposure. *Ultrasound Med. Biol.*, 40(9), pp. 2207–2216, 2014.

[31] R. Paproski, A. Forbrich, M. Hitt, and R. Zemp. RNA biomarker release with ultrasound and phase-change nanodroplets. *Ultrasound Med. Biol.*, 40(8), pp. 1847–1856, 2014.

[32] R. Paproski, J. Jovel, G. K.-S. Wong, J. Lewis, and R. Zemp. Enhanced detection of cancer biomarkers in blood-borne extracellular vesicles using nanodroplets and focused ultrasound. *Cancer Res.*, 2016.

[33] C. England *et al.* Re-assessing the enhanced permeability and retention effect in peripheral arterial disease using radiolabeled long circulating nanoparticles. *Biomaterials*, 100, pp. 101–109, 2016.

[34] P. Sheeran, S. Luois, P. A. Dayton, and T. Matsunaga. Formulation and acoustic studies of a new phase-shift agent for diagnostic and therapeutic ultrasound. *Langmuir*, 27(17), pp. 10412–10420, 2011.

[35] A. Forbrich, T. Harrison, R. Paproski, and R. Zemp. Realtime flash-difference ultrasound imaging of phase-change perfluorocarbon nanodroplet activation. *2012 IEEE Int. Ultrason. Symp.*, pp. 687–690, 2012.

[36] C. Puett, P. Sheeran, J. Rojas, and P. Dayton. Pulse sequences for uniform perfluorocarbon droplet vaporization and ultrasound imaging. *Ultrasonics*, 54(7), pp. 2024–2033, 2014.

[37] J. Bull. The application of microbubbles for targeted drug delivery. *Expert Opin. Drug Deliv.*, 4(5), pp. 475–493, 2007.

[38] B. O'Neill and N. Rapoport. Phase-shift, stimuli-responsive drug carriers for targeted delivery. *Ther. Deliv.*, 2(9), pp. 1165–1187, 2011.

[39] R. Paproski *et al.* Porphyrin nanodroplets: Sub-micrometer ultrasound and photoacoustic contrast imaging agents. *Small*, 12(3), pp. 371–380, 2016.

[40] Y. Li, A. Forbrich, J. Wu, P. Shao, R. Campbell, and R. Zemp. Engineering dark chromoprotein reporters for photoacoustic microscopy and FRET imaging. *Sci. Rep.*, 6, p. 22129, 2016.

[41] J. Yao *et al.* Multiscale photoacoustic tomography using reversibly switchable bacterial phytochrome as a near-infrared photochromic probe. *Nat. Methods*, 13(1), pp. 67–73, 2015.

[42] H. Dortay *et al.* Dual-wavelength photoacoustic imaging of a photoswitchable reporter protein. p. 970820, 2016.

[43] H. Ishikawa-Ankerhold, R. Ankerhold, and G. Drummen. Advanced fluorescence microscopy techniques - FRAP, FLIP, FLAP, FRET and FLIM. *Molecules*, 17(4), pp. 4047–4132, 2012.

[44] S. Ashkenazi. Photoacoustic lifetime imaging of dissolved oxygen using methylene blue. *J. Biomed. Opt.*, 15(4), p. 40501, 2010.

[45] A. Forbrich, P. Shao, W. Shi, and R. Zemp. Lifetime-weighted photoacoustic imaging. *J. Opt.*, 18(12), p. 124001, 2016.

[46] L. Adamczyk *et al.* Lymph vessels: the forgotten second circulation in health and disease. *Virchows Arch.*, 469(1), pp. 3–17, 2016.

[47] J. Scallan, S. Zawieja, J. Castorena-Gonzalez, and M. Davis. Lymphatic pumping: Mechanics, mechanisms and malfunction. *J. Physiol.*, 594(20), pp. 5749–5768, 2016.

[48] E. Sevick-Muraca, S. Kwon, and J. Rasmussen. Emerging lymphatic imaging technologies for mouse and man. *J. Clin. Invest.*, 124(3), pp. 905–914, 2014.

[49] K. H. Song, E. Stein, J. Margenthaler, and L. Wang. Noninvasive photoacoustic identification of sentinel lymph nodes containing methylene blue in vivo in a rat model. *J. Biomed. Opt.*, 13(5), p. 54033, 2008.

[50] Y. Li. Engineering a chromoprotein optimized for photoacoustic imaging and biosensing applications, University of Alberta, 2014.

[51] F. Hyafil *et al.* Noninvasive detection of macrophages using a nanoparticulate contrast agent for computed tomography. *Nat. Med.*, 13(5), pp. 636–641, 2007.

[52] R. Popovtzer *et al.* Targeted gold nanoparticles enable molecular CT imaging of cancer. *Nano Lett.*, 8(12), pp. 4593–4596, 2008.

[53] J. Vaquero and P. Kinahan. Positron emission tomography: Current challenges and opportunities for technological advances in clinical and preclinical imaging systems. *Annu. Rev. Biomed. Eng.*, 17(1), pp. 385–414, 2015.

[54] G. Mariani *et al.* A review on the clinical uses of SPECT/CT. *Eur. J. Nucl. Med. Mol. Imaging*, 37(10), pp. 1959–1985, 2010.

[55] D. Groheux, M. Espié, S. Giacchetti, and E. Hindié. Performance of FDG PET/CT in the clinical management of breast cancer. *Radiology*, 266(2), pp. 388–405, 2013.

[56] C. Gaeta, J. Vercher-Conejero, A. Sher, A. Kohan, C. Rubbert, and N. Avril. Recurrent and metastatic breast cancer PET, PET/CT, PET/MRI: FDG and new biomarkers. *Q. J. Nucl. Med. Mol. Imaging*, 57(4), pp. 352–366, 2013.

[57] A. Howseman and R. Bowtel. Functional magnetic resonance imaging: Imaging techniques and contrast mechanisms. *Philos. Trans. R. Soc. B Biol. Sci.*, 354(1387), pp. 1179–1194, 1999.

[58] G. Zaharchuk. Theoretical basis of hemodynamic MR imaging techniques to measure cerebral blood volume, cerebral blood flow, and permeability. *Am. J. Neuroradiol.*, 28(10), pp. 1850–1858, 2007.

[59] E. Muir, L. Watts, Y. Tiwari, A. Bresnen, Q. Shen, and T. Duong. Quantitative cerebral blood flow measurements using MRI. *Methods Mol. Biol.*, 1135, pp. 205–211, 2014.

[60] S. Caruthers, P. Winter, S. Wickline, and G. Lanza. Targeted magnetic resonance imaging contrast agents. *Methods Mol. Med.*, 124, pp. 387–400, 2006.

[61] A. Morawski, G. Lanza, and S. Wickline. Targeted contrast agents for magnetic resonance imaging and ultrasound. *Curr. Opin. Biotechnol.*, 16(1), pp. 89–92, 2005.

[62] P. R. Hoskins. A review of the measurement of blood velocity and related quantities using Doppler ultrasound. *Proc. Inst. Mech. Eng. H.*, 213(5), pp. 391–400, 1999.

[63] P. McClain, J. Lange, and D. Assimos. Optimizing shock wave lithotripsy: A comprehensive review. *Rev. Urol.*, 15(2), pp. 49–60, 2013.

[64] Y. Zhou. High intensity focused ultrasound in clinical tumor ablation. *World J. Clin. Oncol.*, 2(1), pp. 8–27, 2011.

[65] A. Copelan, J. Hartman, M. Chehab, and A. Venkatesan. High-intensity focused ultrasound:

Current status for image-guided therapy. *Semin. Intervent. Radiol.*, 32(4), pp. 398–415, 2015.

[66] I. Tardy, S. Pochon, M. Theraulaz, P. Nanjappan, and M. Schneider. In vivo ultrasound imaging of thrombi using a target-specific contrast agent. *Acad. Radiol.*, 9(2), pp. S294-6, 2002.

[67] S. Mehier-Humbert, T. Bettinger, F. Yan, and R. Guy. Plasma membrane poration induced by ultrasound exposure: Implication for drug delivery. *J. Control. Release*, 104(1), pp. 213–222, 2005.

[68] R. Sadikot and T. Blackwell. Bioluminescence imaging. *Proc. Am. Thorac. Soc.*, 2(6), pp. 537–540, 2005.

[69] K. Luker and G. Luker. Bioluminescence imaging of reporter mice for studies of infection and inflammation. *Antiviral Res.*, 86(1), pp. 93–100, 2010.

[70] M. Waidmann, F. Bleichrodt, T. Laslo, and C. Riedel. Bacterial luciferase reporters: The Swiss army knife of molecular biology. *Bioeng. Bugs*, 2(1), pp. 8–16, 2011.

[71] L. Frank and V. Krasitskaya. Application of enzyme bioluminescence for medical diagnostics. *Adv. Biochem. Eng. Biotechnol.*, 144, pp. 175–197, 2014.

[72] Y. Jiang, A. Forbrich, T. Harrison, and R. Zemp. Blood oxygen flux estimation with a combined photoacoustic and high-frequency ultrasound microscopy system: A phantom study. *J. Biomed. Opt.*, 17(3), p. 36012, 2012.

[73] D. Pan, B. Kim, L. Wang, and G. Lanza. A brief account of nanoparticle contrast agents for photoacoustic imaging. *Wiley Interdiscip. Rev. Nanomed. Nanobiotechnol.*, 5(6), pp. 517–43, 2013.

[74] L. Li, R. Zemp, G. Lungu, G. Stoica, and L. Wang. Photoacoustic imaging of lacZ gene expression in vivo. *J. Biomed. Opt.*, 12(2), p. 20504, 2007.

[75] R. Paproski, A. Heinmiller, K. Wachowicz, and R. Zemp. Multi-wavelength photoacoustic imaging of inducible tyrosinase reporter gene expression in xenograft tumors. *Sci. Rep.*, 4, p. 5329, 2014.

[76] K. Shyamala, H. Girish, and S. Murgod. Risk of tumor cell seeding through biopsy and aspiration cytology. *J. Int. Soc. Prev. Community Dent.*, 4(1), pp. 5–11, 2014.

[77] E. Mathenge *et al.* Core needle biopsy of breast cancer tumors increases distant metastases in a mouse model. *Neoplasia*, 16(11), pp. 950–960, 2014.

[78] D. Goldenberg *et al.* CEA (carcinoembryonic antigen): Its role as a marker in the management of cancer. *J. Cancer Res. Clin. Oncol.*, 101(3), pp. 239–242, 1981.

[79] M. A. Tainsky. Genomic and proteomic biomarkers for cancer: A multitude of opportunities. *Biochim. Biophys. Acta - Rev. Cancer*, 1796(2), pp. 176–193, 2009.

[80] G. A. Calin *et al.* A MicroRNA signature associated with prognosis and progression in chronic lymphocytic leukemia. *N. Engl. J. Med.*, 353(17), pp. 1793–801, 2005.

[81] S. S. Jeffrey. Cancer biomarker profiling with microRNAs. *Nat. Biotechnol.*, 26(4), pp. 400–

401, 2008.

[82] F. Pimentel *et al.* Technology in MicroRNA Profiling: Circulating MicroRNAs as Noninvasive Cancer Biomarkers in Breast Cancer. *J. Lab. Autom.*, 20(5), pp. 574–588, 2015.

[83] J. Wittmann and H.-M. Jäck. Serum microRNAs as powerful cancer biomarkers. *Biochim. Biophys. Acta - Rev. Cancer*, 1806(2), pp. 200–207, 2010.

[84] Y. Ma, P. Zhang, J. Yang, Z. Liu, Z. Yang, and H. Qin. Candidate microRNA biomarkers in human colorectal cancer: systematic review profiling studies and experimental validation. *Int. J. cancer*, 130(9), pp. 2077–87, 2012.

[85] R. Karshafian and P. Burns. Ultrasound and microbubble mediated generation of transient pores on cell membranes in vitro. *2009 IEEE Int. Ultrason. Symp.*, pp. 1805–1808, 2009.

[86] E. Unger, T. McCreery, and R. Sweitzer. Ultrasound enhances gene expression of liposomal transfection. *Invest. Radiol.*, 32(12), pp. 723–727, 1997.

[87] W. Greenleaf, M. Bolander, G. Sarkar, M. Goldring, and J. Greenleaf. Artificial cavitation nuclei significantly enhance acoustically induced cell transfection. *Ultrasound Med. Biol.*, 24(4), pp. 587–595, 1998.

[88] Y. Liu, H. Miyoshi, and M. Nakamura. Encapsulated ultrasound microbubbles: Therapeutic application in drug/gene delivery. *J. Control. Release*, 114(1), pp. 89–99, 2006.

[89] N. McDannold, N. Vykhodtseva, S. Raymond, F. Jolesz, and K. Hynynen. MRI-guided targeted blood-brain barrier disruption with focused ultrasound: Histological findings in rabbits. *Ultrasound Med. Biol.*, 31(11), pp. 1527–1537, 2005.

[90] S. Raymond, J. Skoch, K. Hynynen, and B. Bacskai. Multiphoton imaging of ultrasound/Optison mediated cerebrovascular effects in vivo. *J. Cereb. Blood Flow Metab.*, 27(2), pp. 393–403, 2007.

[91] D. Simpson, C. Chin, and P. Burns. Pulse inversion Doppler: A new method for detecting nonlinear echoes from microbubble contrast agents. *IEEE Trans. Ultrason. Ferroelectr. Freq. Control*, 46(2), pp. 372–382, 1999.

[92] Y. Hu, S. Qin, and Q. Jiang. Characteristics of acoustic scattering from a double-layered micro shell for encapsulated drug delivery. *IEEE Trans. Ultrason. Ferroelectr. Freq. Control*, 51(7), pp. 809–821, 2004.

[93] H. Zheng, P. Dayton, C. Caskey, S. Zhao, S. Qin, and K. Ferrara. Ultrasound-driven microbubble oscillation and translation within small phantom vessels. *Ultrasound Med. Biol.*, 33(12), pp. 1978–1987, 2007.

[94] A. Doinikov, P. Palanchon, K. Kaddur, and A. Bouakaz. Theoretical exploration of shear stress generated by oscillating microbubbles on the cell membrane in the context of sonoporation. *2009 IEEE Int. Ultrason. Symp.*, pp. 1215–1218, 2009.

[95] Y. Zhou, R. Kumon, J. Cui, and C. Deng. The size of sonoporation pores on the cell membrane. *Ultrasound Med. Biol.*, 35(10), pp. 1756–1760, 2009.

[96] A. Clark *et al.* CRLX101 nanoparticles localize in human tumors and not in adjacent, nonneoplastic tissue after intravenous dosing. *Proc. Natl. Acad. Sci.*, 113(14), pp. 3850–

3854, 2016.

[97] R. Saha, S. Vasanthakumar, G. Bende, and M. Snehalatha. Nanoparticulate drug delivery systems for cancer chemotherapy. *Mol. Membr. Biol.*, 27(7), pp. 215–231, 2010.

[98] M. Jeon *et al.* Methylene blue microbubbles as a model dual-modality contrast agent for ultrasound and activatable photoacoustic imaging. *J. Biomed. Opt.*, 19(1), p. 16005, 2014.

[99] E. Huynh *et al.* Porphyrin shell microbubbles with intrinsic ultrasound and photoacoustic properties. *J. Am. Chem. Soc.*, 134(40), pp. 16464–16467, 2012.

[100] E. Huynh, C. Jin, B. Wilson, and G. Zheng. Aggregate enhanced trimodal porphyrin shell microbubbles for ultrasound, photoacoustic, and fluorescence imaging. *Bioconjug. Chem.*, 25(4), pp. 796–801, 2014.

[101] C. Kim, R. Qin, J. S. Xu, L. Wang, and R. Xu. Multifunctional microbubbles and nanobubbles for photoacoustic and ultrasound imaging. *J. Biomed. Opt.*, 15(1), p. 10510, 2010.

[102] J. Lovell *et al.* Porphysome nanovesicles generated by porphyrin bilayers for use as multimodal biophotonic contrast agents. *Nat. Mater.*, 10(4), pp. 324–332, 2011.

[103] A. Hannah, G. Luke, K. Wilson, K. Homan, and S. Emelianov. Indocyanine green-loaded photoacoustic nanodroplets: dual contrast nanoconstructs for enhanced photoacoustic and ultrasound imaging. *ACS Nano*, 8(1), pp. 250–259, 2014.

[104] M. Xu and L. Wang. Photoacoustic imaging in biomedicine. *Rev. Sci. Instrum.*, 77(4), p. 41101, 2006.

[105] L. Wang, Ed. *Photoacoustic Imaging and Spectroscopy*, 1st ed. CRC Press, 2009.

[106] A. Oraevsky *et al.* Laser optoacoustic imaging of the breast: Detection of cancer angiogenesis. *Proc. SPIE 3597, Opt. Tomogr. Spectrosc. Tissue III*, pp. 352–363, 1999.

[107] G. Xu, J. Fowlkes, C. Tao, X. Liu, and X. Wang. Photoacoustic spectrum analysis for microstructure characterization in biological tissue: Analytical model. *Ultrasound Med. Biol.*, 41(5), pp. 1473–1480, 2015.

[108] M. Xu and L. Wang. Universal back-projection algorithm for photoacoustic computed tomography. *Phys. Rev. E*, 71(1), p. 16706, 2005.

[109] K. Wang, R. Su, A. Oraevsky, and M. Anastasio. Investigation of iterative image reconstruction in three-dimensional optoacoustic tomography. *Phys. Med. Biol.*, 57(17), pp. 5399–5423, 2012.

[110] K. Wang, S. Ermilov, R. Su, H.-P. Brecht, A. Oraevsky, and M. Anastasio. An imaging model incorporating ultrasonic transducer properties for three-dimensional optoacoustic tomography. *IEEE Trans. Med. Imaging*, 30(2), pp. 203–214, 2011.

[111] S. Hu and L. Wang. Photoacoustic imaging and characterization of the microvasculature. *J. Biomed. Opt.*, 15(1), p. 11101, 2010.

[112] J. Yao and L. V. Wang. Photoacoustic tomography: Fundamentals, advances and prospects. *Contrast Media Mol. Imaging*, 6(5), pp. 332–345, 2011.

[113] K. Maslov, G. Stoica, and L. Wang. In vivo dark-field reflection-mode photoacoustic

microscopy. *Opt. Lett.*, 30(6), pp. 625–627, 2005.

[114] K. Maslov, H. Zhang, S. Hu, and L. Wang. Optical-resolution photoacoustic microscopy for in vivo imaging of single capillaries. *Opt. Lett.*, 33(9), pp. 929–931, 2008.

[115] S. Mallidi, G. Luke, and S. Emelianov. Photoacoustic imaging in cancer detection, diagnosis, and treatment guidance. *Trends Biotechnol.*, 29(5), pp. 213–221, 2011.

[116] K. Valluru, K. Wilson, and J. Willmann. Photoacoustic imaging in oncology: Translational preclinical and early clinical experience. *Radiology*, 280(2), pp. 332–349, 2016.

[117] J. Staley, P. Grogan, A. Samadi, H. Cui, M. Cohen, and X. Yang. Growth of melanoma brain tumors monitored by photoacoustic microscopy. *J. Biomed. Opt.*, 15(4), p. 40510, 2010.

[118] L. Li, H. Zhang, R. Zemp, K. Maslov, and L. Wang. Simultaneous imaging of a lacZ-marked tumor and microvasculature morphology in vivo by dual-wavelength photoacoustic microscopy. *J. Innov. Opt. Health Sci.*, 1(2), pp. 207–215, 2008.

[119] B. Wang, J. Su, A. Karpiouk, K. Sokolov, R. Smalling, and S. Emelianov. Intravascular photoacoustic imaging. *IEEE J. Quantum Electron.*, 16(3), pp. 588–599, 2010.

[120] A. Taruttis, E. Herzog, D. Razansky, and V. Ntziachristos. Real-time imaging of cardiovascular dynamics and circulating gold nanorods with multispectral optoacoustic tomography. *Opt. Express*, 18(19), pp. 19592–19602, 2010.

[121] R. Zemp, L. Song, R. Bitton, K. Shung, and L. Wang. Realtime photoacoustic microscopy of murine cardiovascular dynamics. *Opt. Express*, 16(22), pp. 18551–18556, 2008.

[122] K. Jansen, G. van Soest, and A. van der Steen. Intravascular photoacoustic imaging: A new tool for vulnerable plaque identification. *Ultrasound Med. Biol.*, 40(6), pp. 1037–1048, 2014.

[123] J. Park *et al.* High frequency photoacoustic imaging for in vivo visualizing blood flow of zebrafish heart. *Opt. Express*, 21(12), pp. 14636–14642, 2013.

[124] S. Hu and L. Wang. Neurovascular photoacoustic tomography. *Front. Neuroenergetics*, 2, p. 10, 2010.

[125] X. Wang, Y. Pang, G. Ku, X. Xie, G. Stoica, and L. Wang. Noninvasive laser-induced photoacoustic tomography for structural and functional in vivo imaging of the brain. *Nat. Biotechnol.*, 21(7), pp. 803–806, 2003.

[126] M. Nasiriavanaki, J. Xia, H. Wan, A. Bauer, J. Culver, and L. Wang. High-resolution photoacoustic tomography of resting-state functional connectivity in the mouse brain. *Proc. Natl. Acad. Sci. U. S. A.*, 111(1), pp. 21–26, 2014.

[127] X. Deán-Ben *et al.* Functional optoacoustic neuro-tomography for scalable whole-brain monitoring of calcium indicators. *Light Sci. Appl.*, 5(12), p. e16201, 2016.

[128] R. Silverman *et al.* High-resolution photoacoustic imaging of ocular tissues. *Ultrasound Med. Biol.*, 36(5), pp. 733–742, 2010.

[129] H. Zhang, C. Puliafito, and S. Jiao. Photoacoustic ophthalmoscopy for in vivo retinal imaging: Current status and prospects. *Ophthalmic Surg. Lasers Imaging*, 42 Suppl, pp.

S106–S115, 2011.

[130] C. Favazza, O. Jassim, L. Cornelius, and L. Wang. In vivo photoacoustic microscopy of human cutaneous microvasculature and a nevus. *J. Biomed. Opt.*, 16(1), p. 16015, 2011.

[131] L. Song, K. Maslov, K. Shung, and L. Wang. Ultrasound-array-based real-time photoacoustic microscopy of human pulsatile dynamics in vivo. *J. Biomed. Opt.*, 15(2), p. 21303, 2010.

[132] Y. Zhou, W. Xing, K. Maslov, L. Cornelius, and L. Wang. Handheld photoacoustic microscopy to detect melanoma depth in vivo. *Opt. Lett.*, 39(16), pp. 4731–4734, 2014.

[133] J. Yang *et al.* Three-dimensional photoacoustic endoscopic imaging of the rabbit esophagus. *PLoS One*, 10(4), p. e0120269, 2015.

[134] H. Zhang, K. Maslov, M. Sivaramakrishnan, G. Stoica, and L. Wang. Imaging of hemoglobin oxygen saturation variations in single vessels in vivo using photoacoustic microscopy. *Appl. Phys. Lett.*, 90(5), p. 53901, 2007.

[135] Y. Lao, D. Xing, S. Yang, and L. Xiang. Noninvasive photoacoustic imaging of the developing vasculature during early tumor growth. *Phys. Med. Biol.*, 53(15), pp. 4203–4212, 2008.

[136] C. Bayer, P. Joshi, and S. Emelianov. Photoacoustic imaging: A potential tool to detect early indicators of metastasis. *Expert Rev. Med. Devices*, 10(1), pp. 125–134, 2013.

[137] J. Guggenheim *et al.* Photoacoustic imaging of human lymph nodes with endogenous lipid and hemoglobin contrast. *J. Biomed. Opt.*, 20(5), p. 50504, 2015.

[138] R. Siphanto *et al.* Serial noninvasive photoacoustic imaging of neovascularization in tumor angiogenesis. *Opt. Express*, 13(1), pp. 89–95, 2005.

[139] A. El-Kenawi and A. El-Remessy. Angiogenesis inhibitors in cancer therapy: Mechanistic perspective on classification and treatment rationales. *Br. J. Pharmacol.*, 170(4), pp. 712–729, 2013.

[140] B. Al-Husein, M. Abdalla, M. Trepte, D. Deremer, and P. Somanath. Antiangiogenic therapy for cancer: An update. *Pharmacotherapy*, 32(12), pp. 1095–1111, 2012.

[141] S. Bohndiek, L. Sasportas, S. Machtaler, J. Jokerst, S. Hori, and S. Gambhir. Photoacoustic tomography detects early vessel regression and normalization during ovarian tumor response to the antiangiogenic therapy trebananib. *J. Nucl. Med.*, 56(12), pp. 1942–1947, 2015.

[142] S. Prahl. Optical Absorption of Hemoglobin. [Online]. Available: http://omlc.org/spectra/hemoglobin/. [Accessed: 16-Dec-2016].

[143] W. Zijlstra, A. Buursma, and W. Meeuwsen-van der Roest. Absorption spectra of human fetal and adult oxyhemoglobin, de-oxyhemoglobin, carboxyhemoglobin, and methemoglobin. *Clin. Chem.*, 37(9), pp. 1633–1638, 1991.

[144] J. Laufer, E. Zhang, and P. Beard. Quantitative in vivo measurements of blood oxygen saturation using multiwavelength photoacoustic imaging. *Proc. SPIE*, p. 64371Z, 2007.

[145] A. Hussain, W. Petersen, J. Staley, E. Hondebrink, and W. Steenbergen. Quantitative blood oxygen saturation imaging using combined photoacoustics and acousto-optics. *Opt. Lett.*,

41(8), pp. 1720–1723, 2016.

[146] J. Oh, M. Li, H. Zhang, K. Maslov, G. Stoica, and L. Wang. Three-dimensional imaging of skin melanoma in vivo by dual-wavelength photoacoustic microscopy. *J. Biomed. Opt.*, 11(3), p. 34032, 2006.

[147] D. Grootendorst *et al.* First experiences of photoacoustic imaging for detection of melanoma metastases in resected human lymph nodes. *Lasers Surg. Med.*, 44(7), pp. 541–549, 2012.

[148] R. Weight, J. Viator, P. Dale, C. Caldwell, and A. Lisle. Photoacoustic detection of metastatic melanoma cells in the human circulatory system. *Opt. Lett.*, 31(20), pp. 2998–3000, 2006.

[149] Y. Wang *et al.* Fiber-laser-based photoacoustic microscopy and melanoma cell detection. *J. Biomed. Opt.*, 16(1), p. 11014, 2011.

[150] P. Wang *et al.* High-speed intravascular photoacoustic imaging of lipid-laden atherosclerotic plaque enabled by a 2-kHz barium nitrite raman laser. *Sci. Rep.*, 4, p. 6889, 2014.

[151] J. Pauli *et al.* An in vitro characterization study of new near infrared dyes for molecular imaging. *Eur. J. Med. Chem.*, 44(9), pp. 3496–3503, 2009.

[152] C. Kim, K. Song, F. Gao, and L. Wang. Sentinel lymph nodes and lymphatic vessels: Noninvasive dual-modality in vivo mapping by using indocyanine green in rat -Volumetric spectroscopic photoacoustic imaging and planar fluorescence imaging. *Radiology*, 255(2), pp. 442–450, 2010.

[153] H. Wang *et al.* In vivo photoacoustic molecular imaging of breast carcinoma with folate receptor-targeted indocyanine green nanoprobes. *Nanoscale*, 6(23), pp. 14270–14279, 2014.

[154] K. Sano *et al.* In vivo photoacoustic imaging of cancer using indocyanine green-labeled monoclonal antibody targeting the epidermal growth factor receptor. *Biochem. Biophys. Res. Commun.*, 464(3), pp. 820–825, 2015.

[155] V. Nguyen, Y. Oh, K. Ha, J. Oh, and H. W. Kang. Enhancement of high-resolution photoacoustic imaging with indocyanine green-conjugated carbon nanotubes. *Jpn. J. Appl. Phys.*, 54(7S1), p. 07HF04, 2015.

[156] W. Li and X. Chen. Gold nanoparticles for photoacoustic imaging. *Nanomedicine (Lond).*, 10(2), pp. 299–320, 2015.

[157] P. Li *et al.* In vivo photoacoustic molecular imaging with simultaneous multiple selective targeting using antibody-conjugated gold nanorods. *Opt. Express*, 16(23), p. 18605, 2008.

[158] A. De La Zerda *et al.* Carbon nanotubes as photoacoustic molecular imaging agents in living mice. *Nat. Nanotechnol.*, 3(9), pp. 557–562, 2008.

[159] S. Maji *et al.* Upconversion nanoparticles as a contrast agent for photoacoustic imaging in live mice. *Adv. Mater.*, 26(32), pp. 5633–5638, 2014.

[160] A. Garcia-Uribe *et al.* Dual-modality photoacoustic and ultrasound imaging system for noninvasive sentinel lymph node detection in patients with breast cancer. *Sci. Rep.*, 5, p.

15748, 2015.

[161] L. Li, H. Zhang, R. Zemp, K. Maslov, and L. Wang. Simultaneous imaging of a lacZ-marked tumor and microvasculature morphology in vivo by dual-wavelength photoacoustic microscopy. *J. Innov. Opt. Health Sci.*, 1(2), pp. 207–215, 2008.

[162] A. Jathoul *et al.* Deep in vivo photoacoustic imaging of mammalian tissues using a tyrosinase-based genetic reporter. *Nat. Photonics*, 9(4), pp. 239–246, 2015.

[163] A. Krumholz, S. Vanvickle-Chavez, J. Yao, T. Fleming, W. Gillanders, and L. Wang. Photoacoustic microscopy of tyrosinase reporter gene in vivo. *J. Biomed. Opt.*, 16(8), p. 80503, 2011.

[164] R. Paproski, A. Forbrich, K. Wachowicz, M. Hitt, and R. Zemp. Tyrosinase as a dual reporter gene for both photoacoustic and magnetic resonance imaging. *Biomed. Opt. Express*, 2(4), pp. 771–780, 2011.

[165] K. Urabe *et al.* The inherent cytotoxicity of melanin precursors: A revision. *Biochim. Biophys. Acta*, 1221(3), pp. 272–278, 1994.

[166] D. Razansky *et al.* Multispectral opto-acoustic tomography of deep-seated fluorescent proteins in vivo. *Nat. Photonics*, 3(7), pp. 412–417, 2009.

[167] A. Krumholz, D. Shcherbakova, J. Xia, L. Wang, and V. Verkhusha. Multicontrast photoacoustic in vivo imaging using near-infrared fluorescent proteins. *Sci. Rep.*, 4, p. 3939, 2014.

[168] M. Ahrens, M. Orger, D. Robson, J. Li, and P. Keller. Whole-brain functional imaging at cellular resolution using light-sheet microscopy. *Nat. Methods*, 10(5), pp. 413–420, 2013.

[169] A. Pettikiriarachchi, L. Gong, M. Perugini, R. Devenish, and M. Prescott. Ultramarine, a chromoprotein acceptor for Förster resonance energy transfer. *PLoS One*, 7(7), p. e41028, 2012.

[170] M. Chan *et al.* Structural characterization of a blue chromoprotein and its yellow mutant from the sea anemone Cnidopus japonicus. *J. Biol. Chem.*, 281(49), pp. 37813–37819, 2006.

[171] L. Caplan *et al.* Stroke-related translational research. *Arch. Neurol.*, 68(9), pp. 1110–1123, 2011.

[172] H. Schmidt, R. Shelton, and R. Duman. Functional biomarkers of depression: Diagnosis, treatment, and pathophysiology. *Neuropsychopharmacology*, 36(12), pp. 2375–2394, 2011.

[173] A. Bhatt, R. Mathur, A. Farooque, A. Verma, and B. Dwarakanath. Cancer biomarkers - Current perspectives. *Indian J. Med. Res.*, 132, pp. 129–49, 2010.

[174] C. Madu and Y. Lu. Novel diagnostic biomarkers for prostate cancer. *J. Cancer*, 1, pp. 150–177, 2010.

[175] J. Ross *et al.* Breast cancer biomarkers and molecular medicine. *Expert Rev. Mol. Diagn.*, 3(5), pp. 573–585, 2003.

[176] H. Sung and J. Cho. Biomarkers for the lung cancer diagnosis and their advances in proteomics. *BMB Rep.*, 41(9), pp. 615–625, 2008.

[177] S. Hanash, C. Baik, and O. Kallioniemi. Emerging molecular biomarkers - Blood-based strategies to detect and monitor cancer. *Nat. Rev. Clin. Oncol.*, 8(3), pp. 142–150, 2011.

[178] S. Beachy and E. Repasky. Using extracellular biomarkers for monitoring efficacy of therapeutics in cancer patients: An update. *Cancer Immunol. Immunother.*, 57(6), pp. 759–775, 2008.

[179] M. Tainsky. Genomic and proteomic biomarkers for cancer: A multitude of opportunities. *Biochim. Biophys. Acta - Rev. Cancer*, 1796(2), pp. 176–193, 2009.

[180] S. Chen *et al.* Efficient gene delivery to pancreatic islets with ultrasonic microbubble destruction technology. *Proc. Natl. Acad. Sci.*, 103(22), pp. 8469–8474, 2006.

[181] A. Delalande, M. Postema, N. Mignet, P. Midoux, and C. Pichon. Ultrasound and microbubble-assisted gene delivery: Recent advances and ongoing challenges. *Ther. Deliv.*, 3(10), pp. 1199–1215, 2012.

[182] N. Nomikou and A. McHale. Exploiting ultrasound-mediated effects in delivering targeted, site-specific cancer therapy. *Cancer Lett.*, 296(2), pp. 133–143, 2010.

[183] Y. Luo, Y. Zhao, C. Lu, J. Tang, and X. Li. Application of ultrasonic gas-filled liposomes in enhancing transfer for breast cancer–related antisense oligonucleotides: An experimental study. *J. Liposome Res.*, 18(4), pp. 341–351, 2008.

[184] K. Kaddur, L. Lebegue, F. Tranquart, P. Midoux, C. Pichon, and A. Bouakaz. Transient transmembrane release of green fluorescent proteins with sonoporation. *IEEE Trans. Ultrason. Ferroelectr. Freq. Control*, 57(7), pp. 1558–1567, 2010.

[185] Z. Fan, H. Liu, M. Mayer, and C. Deng. Spatiotemporally controlled single cell sonoporation. *Proc. Natl. Acad. Sci.*, 109(41), pp. 16486–16491, 2012.

[186] P. Holland, R. Abramson, R. Watson, and D. Gelfand. Detection of specific polymerase chain reaction product by utilizing the 5’-3’ exonuclease activity of Thermus aquaticus DNA polymerase. *Proc. Natl. Acad. Sci. U. S. A.*, 88(16), pp. 7276–7280, 1991.

[187] S. Bustin. Absolute quantification of mRNA using real-time reverse transcription polymerase chain reaction assays. *J. Mol. Endocrinol.*, 25(2), pp. 169–193, 2000.

[188] Y. Kim *et al.* Targeted proteomics identifies liquid-biopsy signatures for extracapsular prostate cancer. *Nat. Commun.*, 7, p. 11906, 2016.

[189] K. Spalding, R. Board, T. Dawson, M. Jenkinson, and M. Baker. A review of novel analytical diagnostics for liquid biopsies: Spectroscopic and spectrometric serum profiling of primary and secondary brain tumors. *Brain Behav.*, 6(9), p. e00502, 2016.

[190] A. Giessing and F. Kirpekar. Mass spectrometry in the biology of RNA and its modifications. *J. Proteomics*, 75(12), pp. 3434–3449, 2012.

[191] G. Bianchini, J. Balko, I. Mayer, M. Sanders, and L. Gianni. Triple-negative breast cancer: Challenges and opportunities of a heterogeneous disease. *Nat. Rev. Clin. Oncol.*, 13(11), pp. 674–690, 2016.

[192] M. Weigel and M. Dowsett. Current and emerging biomarkers in breast cancer: Prognosis and prediction. *Endocr. Relat. Cancer*, 17(4), pp. R245–R262, 2010.

[193] J. Shaw and J. Stebbing. Circulating free DNA in the management of breast cancer. *Ann. Transl. Med.*, 2(1), p. 3, 2014.

[194] C. Reyes, C. Gomez-Fernández, and M. Nadji. Metaplastic and medullary mammary carcinomas do not express mammaglobin. *Am. J. Clin. Pathol.*, 137(5), pp. 747–752, 2012.

[195] J. Han *et al.* Mammaglobin expression in lymph nodes is an important marker of metastatic breast carcinoma. *Arch. Pathol. Lab. Med.*, 127(10), pp. 1330–1334, 2003.

[196] C. Newman and T. Bettinger. Gene therapy progress and prospects: Ultrasound for gene transfer. *Gene Ther.*, 14(6), pp. 465–475, 2007.

[197] H. Liang, J. Tang, and M. Halliwell. Sonoporation, drug delivery, and gene therapy. *Proc. Inst. Mech. Eng. H.*, 224(2), pp. 343–361, 2010.

[198] B. Polat, D. Blankschtein, and R. Langer. Low-frequency sonophoresis: application to the transdermal delivery of macromolecules and hydrophilic drugs. *Expert Opin. Drug Deliv.*, 7(12), pp. 1415–1432, 2010.

[199] J. Hwang, A. Brayman, M. Reidy, T. Matula, M. Kimmey, and L. Crum. Vascular effects induced by combined 1-MHz ultrasound and microbubble contrast agent treatments in vivo. *Ultrasound Med. Biol.*, 31(4), pp. 553–564, 2005.

[200] N. Vykhodtseva, N. McDannold, and K. Hynynen. Progress and problems in the application of focused ultrasound for blood-brain barrier disruption. *Ultrasonics*, 48(4), pp. 279–296, 2008.

[201] S. Jeffrey. Cancer biomarker profiling with microRNAs. *Nat. Biotechnol.*, 26(4), pp. 400–401, 2008.

[202] H. Heneghan, N. Miller, A. Lowery, K. Sweeney, J. Newell, and M. Kerin. Circulating microRNAs as novel minimally invasive biomarkers for breast cancer. *Ann. Surg.*, 251(3), pp. 499–505, 2010.

[203] J. Wittmann and H. Jäck. Serum microRNAs as powerful cancer biomarkers. *Biochim. Biophys. Acta - Rev. Cancer*, 1806(2), pp. 200–207, 2010.

[204] S. Sassen, E. Miska, and C. Caldas. MicroRNA - Implications for cancer. *Virchows Arch.*, 452(1), pp. 1–10, 2008.

[205] S. Fu, L. Chen, and Y. Man. miRNA biomarkers in breast cancer detection and management. *J. Cancer*, 2, pp. 116–122, 2011.

[206] Y. Ma, P. Zhang, J. Yang, Z. Liu, Z. Yang, and H. Qin. Candidate microRNA biomarkers in human colorectal cancer: Systematic review profiling studies and experimental validation. *Int. J. Cancer*, 130(9), pp. 2077–2087, 2012.

[207] N. Kosaka, H. Iguchi, and T. Ochiya. Circulating microRNA in body fluid: A new potential biomarker for cancer diagnosis and prognosis. *Cancer Sci.*, 101(10), pp. 2087–2092, 2010.

[208] A. Lujambio and S. Lowe. The microcosmos of cancer. *Nature*, 482(7385), pp. 347–355,

2012.

[209] J. Lu *et al.* MicroRNA expression profiles classify human cancers. *Nature*, 435(7043), pp. 834–838, 2005.

[210] G. Calin *et al.* A microRNA signature associated with prognosis and progression in chronic lymphocytic leukemia. *N. Engl. J. Med.*, 353(17), pp. 1793–1801, 2005.

[211] M. Mattie *et al.* Optimized high-throughput microRNA expression profiling provides novel biomarker assessment of clinical prostate and breast cancer biopsies. *Mol. Cancer*, 5, p. 24, 2006.

[212] M. Iorio *et al.* MicroRNA gene expression deregulation in human breast cancer. *Cancer Res.*, 65(16), pp. 7065–7070, 2005.

[213] P. Mitchell *et al.* Circulating microRNAs as stable blood-based markers for cancer detection. *Proc. Natl. Acad. Sci. U. S. A.*, 105(30), pp. 10513–10518, 2008.

[214] S. Volinia *et al.* A microRNA expression signature of human solid tumors defines cancer gene targets. *Proc. Natl. Acad. Sci.*, 103(7), pp. 2257–2261, 2006.

[215] F. Yang *et al.* Experimental study on cell self-sealing during sonoporation. *J. Control. Release*, 131(3), pp. 205–210, 2008.

[216] C. Deng, F. Sieling, H. Pan, and J. Cui. Ultrasound-induced cell membrane porosity. *Ultrasound Med. Biol.*, 30(4), pp. 519–526, 2004.

[217] Y. Zhao *et al.* Phospholipids-based microbubbles sonoporation pore size and reseal of cell membrane cultured in vitro. *J. Drug Target.*, 16(1), pp. 18–25, 2008.

[218] M. Kinoshita and K. Hynynen. Key factors that affect sonoporation efficiency in in vitro settings: The importance of standing wave in sonoporation. *Biochem. Biophys. Res. Commun.*, 359(4), pp. 860–865, 2007.

[219] K. Hensel, M. Mienkina, and G. Schmitz. Analysis of ultrasound fields in cell culture wells for in vitro ultrasound therapy experiments. *Ultrasound Med. Biol.*, 37(12), pp. 2105–2115, 2011.

[220] Y. Chuang *et al.* Gene expression after treatment with hydrogen peroxide, menadione, or t-butyl hydroperoxide in breast cancer cells. *Cancer Res.*, 62(21), pp. 6246–6254, 2002.

[221] E. Linley, S. Denyer, G. McDonnell, C. Simons, and J. Maillard. Use of hydrogen peroxide as a biocide: new consideration of its mechanisms of biocidal action. *J. Antimicrob. Chemother.*, 67(7), pp. 1589–1596, 2012.

[222] P. Marmottant and S. Hilgenfeldt. Controlled vesicle deformation and lysis by single oscillating bubbles. *Nature*, 423(6936), pp. 153–156, 2003.

[223] J. Wu. Theoretical study on shear stress generated by microstreaming surrounding contrast agents attached to living cells. *Ultrasound Med. Biol.*, 28(1), pp. 125–129, 2002.

[224] M. Lokhandwalla and B. Sturtevant. Mechanical haemolysis in shock wave lithotripsy (SWL): I Analysis of cell deformation due to SWL flow-fields. *Phys. Med. Biol.*, 46(2), pp. 413–437, 2001.

[225] C. Ohl *et al.* Sonoporation from jetting cavitation bubbles. *Biophys. J.*, 91(11), pp. 4285–4295, 2006.

[226] P. Prentice, A. Cuschieri, K. Dholakia, M. Prausnitz, and P. Campbell. Membrane disruption by optically controlled microbubble cavitation. *Nat. Phys.*, 1(2), pp. 107–110, 2005.

[227] R. Zheng *et al.* Nanobubbles for enhanced ultrasound imaging of tumors. *Int. J. Nanomedicine*, 7, pp. 895–904, 2012.

[228] K. Wilson, K. Homan, and S. Emelianov. Biomedical photoacoustics beyond thermal expansion using triggered nanodroplet vaporization for contrast-enhanced imaging. *Nat. Commun.*, 3, p. 618, 2012.

[229] J. Arroyo *et al.* Argonaute2 complexes carry a population of circulating microRNAs independent of vesicles in human plasma. *Proc. Natl. Acad. Sci.*, 108(12), pp. 5003–5008, 2011.

[230] E. Zandberga, V. Kozirovskis, A. Ābols, D. Andrējeva, G. Purkalne, and A. Linē. Cell-free microRNAs as diagnostic, prognostic, and predictive biomarkers for lung cancer. *Genes, Chromosom. Cancer*, 52(4), pp. 356–369, 2013.

[231] N. Rapoport. Drug-loaded perfluorocarbon nanodroplets for ultrasound-mediated drug delivery. *Adv. Exp. Med. Biol.*, 880, pp. 221–241, 2016.

[232] S. Hernot and A. Klibanov. Microbubbles in ultrasound-triggered drug and gene delivery. *Adv. Drug Deliv. Rev.*, 60(10), pp. 1153–1166, 2008.

[233] K. Ferrara, M. Borden, and H. Zhang. Lipid-shelled vehicles: Engineering for ultrasound molecular imaging and drug delivery. *Acc. Chem. Res.*, 42(7), pp. 881–892, 2009.

[234] A. L. Klibanov. Preparation of targeted microbubbles: Ultrasound contrast agents for molecular imaging. *Med. Biol. Eng. Comput.*, 47(8), pp. 875–882, 2009.

[235] A. Elzoghby, W. Samy, and N. Elgindy. Albumin-based nanoparticles as potential controlled release drug delivery systems. *J. Control. Release*, 157(2), pp. 168–182, 2012.

[236] S. Dove, O. Hoegh-Guldberg, and S. Ranganathan. Major colour patterns of reef-building corals are due to a family of GFP-like proteins. *Coral Reefs*, 19(3), pp. 197–204, 2001.

[237] F. Oswald *et al.* Contributions of host and symbiont pigments to the coloration of reef corals. *FEBS J.*, 274(4), pp. 1102–1122, 2007.

[238] Y. Labas *et al.* Diversity and evolution of the green fluorescent protein family. *Proc. Natl. Acad. Sci.*, 99(7), pp. 4256–4261, 2002.

[239] T. Craggs. Green fluorescent protein: Structure, folding and chromophore maturation. *Chem. Soc. Rev.*, 38(10), pp. 2865–2875, 2009.

[240] R. Campbell and M. Davidson. Fluorescent Reporter Proteins, in *Molecular Imaging with Reporter Genes*, S. S. Gambhir, Sanjiv S.; Yaghoubi, Ed. New York: Cambridge University Press, 2010, pp. 3–40.

[241] D. Chudakov, M. Matz, S. Lukyanov, and K. Lukyanov. Fluorescent proteins and their applications in imaging living cells and tissues. *Physiol. Rev.*, 90(3), pp. 1103–1163, 2010.

[242] G. Filonov, A. Krumholz, J. Xia, J. Yao, L. Wang, and V. Verkhusha. Deep-tissue photoacoustic tomography of a genetically encoded near-infrared fluorescent probe. *Angew. Chem. Int. Ed. Engl.*, 51(6), pp. 1448–1451, 2012.

[243] S. Dove, M. Takabayashi, and O. Hoegh-Guldberg. Isolation and partial characterization of the pink and blue pigments of Pocilloporid and Acroporid corals. *Biol. Bull.*, 189(3), pp. 288–297, 1995.

[244] K. Lukyanov *et al.* Natural animal coloration can be determined by a nonfluorescent green fluorescent protein homolog. *J. Biol. Chem.*, 275(34), pp. 25879–25882, 2000.

[245] N. Gurskaya *et al.* GFP-like chromoproteins as a source of far-red fluorescent proteins. *FEBS Lett.*, 507(1), pp. 16–20, 2001.

[246] S. Ganesan, S. Ameer-Beg, T. Ng, B. Vojnovic, and F. Wouters. A dark yellow fluorescent protein (YFP)-based Resonance Energy-Accepting Chromoprotein (REACh) for Förster resonance energy transfer with GFP. *Proc. Natl. Acad. Sci. U. S. A.*, 103(11), pp. 4089–4094, 2006.

[247] C. Don Paul *et al.* Phanta: A non-fluorescent photochromic acceptor for pcFRET. *PLoS One*, 8(9), p. e75835, 2013.

[248] M. Cordes, A. Davidson, and R. Sauer. Sequence space, folding and protein design. *Curr. Opin. Struct. Biol.*, 6(1), pp. 3–10, 1996.

[249] R. Chica, M. Moore, B. Allen, and S. Mayo. Generation of longer emission wavelength red fluorescent proteins using computationally designed libraries. *Proc. Natl. Acad. Sci. U. S. A.*, 107(47), pp. 20257–20262, 2010.

[250] L. Yuan, I. Kurek, J. English, and R. Keenan. Laboratory-directed protein evolution. *Microbiol. Mol. Biol. Rev.*, 69(3), pp. 373–392, 2005.

[251] P. Cirino, K. Mayer, and D. Umeno. Generating mutant libraries using error-prone PCR, in *Directed Evolution Library Creation*, 231, New Jersey: Humana Press, 2003, pp. 3–10.

[252] S. Sen, V. Venkata Dasu, and B. Mandal. Developments in directed evolution for improving enzyme functions. *Appl. Biochem. Biotechnol.*, 143(3), pp. 212–223, 2007.

[253] A. Aharoni, A. Griffiths, and D. Tawfik. High-throughput screens and selections of enzyme-encoding genes. *Curr. Opin. Chem. Biol.*, 9(2), pp. 210–216, 2005.

[254] R. Clegg. *Chapter 1 Forster resonance energy transfer — FRET what is it, why do it, and how it's done*, 33rd ed., 33. North-Holland Pub. Co., 2009.

[255] Y. Sun, H. Wallrabe, S. Seo, and A. Periasamy. FRET microscopy in 2010: The legacy of Theodor Förster on the 100th anniversary of his birth. *ChemPhysChem*, 12(3), pp. 462–474, 2011.

[256] Y. Ding, H. Ai, H. Hoi, and R. Campbell. Förster resonance energy transfer-based biosensors for multiparameter ratiometric imaging of Ca2+ dynamics and caspase-3 activity in single cells. *Anal. Chem.*, 83(24), pp. 9687–9693, 2011.

[257] H. Ai, K. Hazelwood, M. Davidson, and R. Campbell. Fluorescent protein FRET pairs for ratiometric imaging of dual biosensors. *Nat. Methods*, 5(5), pp. 401–403, 2008.

[258] R. Tsien *et al.* Fluorescent indicators for Ca2+ based on green fluorescent proteins and calmodulin. *Nature*, 388(6645), pp. 882–887, 1997.

[259] K. Aoki and M. Matsuda. Visualization of small GTPase activity with fluorescence resonance energy transfer-based biosensors. *Nat. Protoc.*, 4(11), pp. 1623–1631, 2009.

[260] Y. Wang and L. Wang. Förster resonance energy transfer photoacoustic microscopy. *J. Biomed. Opt.*, 17(8), p. 86007, 2012.

[261] Y. Wang, J. Xia, and L. Wang. Deep-tissue photoacoustic tomography of Förster resonance energy transfer. *J. Biomed. Opt.*, 18(10), p. 101316, 2013.

[262] N. Shaner, R. Campbell, P. Steinbach, B. Giepmans, A. Palmer, and R. Tsien. Improved monomeric red, orange and yellow fluorescent proteins derived from Discosoma sp red fluorescent protein. *Nat. Biotechnol.*, 22(12), pp. 1567–1572, 2004.

[263] X. Shu, N. Shaner, C. Yarbrough, R. Tsien, and S. Remington. Novel chromophores and buried charges control color in mFruits. *Biochemistry*, 45(32), pp. 9639–9647, 2006.

[264] R. Siegel *et al.* Measurement of molecular interactions in living cells by fluorescence resonance energy transfer between variants of the green fluorescent protein. *Sci. STKE*, 2000(38), p. pl1, 2000.

[265] D. Razansky *et al.* Multispectral opto-acoustic tomography of deep-seated fluorescent proteins in vivo. *Nat. Photonics*, 3(7), pp. 412–417, 2009.

[266] M. Fromant, S. Blanquet, and P. Plateau. Direct random mutagenesis of gene-sized DNA fragments using polymerase chain reaction. *Anal. Biochem.*, 224(1), pp. 347–353, 1995.

[267] T. Harrison, J. Ranasinghesagara, H. Lu, K. Mathewson, A. Walsh, and R. Zemp. Combined photoacoustic and ultrasound biomicroscopy. *Opt. Express*, 17(24), pp. 22041–22046, 2009.

[268] S. Hu, K. Maslov, and L. Wang. Second-generation optical-resolution photoacoustic microscopy with improved sensitivity and speed. *Opt. Lett.*, 36(7), pp. 1134–1136, 2011.

[269] P. Shao, W. Shi, R. Chee, and R. Zemp. Mosaic acquisition and processing for optical-resolution photoacoustic microscopy. *J. Biomed. Opt.*, 17(8), pp. 80503–1, 2012.

[270] Q. Shao, E. Morgounova, C. Jiang, J. Choi, J. Bischof, and S. Ashkenazi. In vivo photoacoustic lifetime imaging of tumor hypoxia in small animals. *J. Biomed. Opt.*, 18(7), p. 76019, 2013.

[271] S. Huang, J. Eary, C. Jia, L. Huang, S. Ashkenazi, and M. O'Donnell. Differential-absorption photoacoustic imaging. *Opt. Lett.*, 34(16), pp. 2393–2395, 2009.

[272] E. Morgounova, Q. Shao, B. Hackel, D. Thomas, and S. Ashkenazi. Photoacoustic lifetime contrast between methylene blue monomers and self-quenched dimers as a model for dual-labeled activatable probes. *J. Biomed. Opt.*, 18(5), p. 56004, 2013.

[273] A. Forbrich, P. Shao, W. Shi, and R. Zemp. Lifetime-weighted photoacoustic imaging. *SPIE 9323, Photons Plus Ultrasound Imaging Sens. 2015*, p. 93231H, 2015.

[274] Q. Shao and S. Ashkenazi. Photoacoustic lifetime imaging for direct in vivo tissue oxygen monitoring. *J. Biomed. Opt.*, 20(3), p. 36004, 2015.

[275] W. Shi, P. Shao, and R. Zemp. Investigation of photoacoustic signal strength as a function of scan-speed and laser-repetition-rate. *2013 IEEE Int. Ultrason. Symp.*, pp. 1534–1536, 2013.

[276] R. Ahmed, K. Schmitz, A. Prizment, and A. Folsom. Risk factors for lymphedema in breast cancer survivors, the Iowa Women's Health Study. *Breast Cancer Res. Treat.*, 130(3), pp. 981–991, 2011.

[277] Y. Cemal, A. Pusic, and B. Mehrara. Preventative measures for lymphedema: Separating fact from fiction. *J. Am. Coll. Surg.*, 213(4), pp. 543–551, 2011.

[278] J. Armer. The problem of post-breast cancer lymphedema: impact and measurement issues. *Cancer Invest.*, 23(1), pp. 76–83, 2005.

[279] L. Munn and T. Padera. Imaging the lymphatic system. *Microvasc. Res.*, 96, pp. 55–63, 2014.

[280] M. Marshall *et al.* Near-infrared fluorescence imaging in humans with indocyanine green: A review and update. *Open Surg. Oncol. J.*, 2(2), pp. 12–25, 2010.

[281] N. Stout Gergich, L. Pfalzer, C. McGarvey, B. Springer, L. Gerber, and P. Soballe. Preoperative assessment enables the early diagnosis and successful treatment of lymphedema. *Cancer*, 112(12), pp. 2809–2819, 2008.

[282] M. Aldrich *et al.* Lymphatic abnormalities in the normal contralateral arms of subjects with breast cancer-related lymphedema as assessed by near-infrared fluorescent imaging. *Biomed. Opt. Express*, 3(6), pp. 1256–1265, 2012.

[283] Y. Ogasawara, H. Ikeda, M. Takahashi, K. Kawasaki, and H. Doihara. Evaluation of breast lymphatic pathways with indocyanine green fluorescence imaging in patients with breast cancer. *World J. Surg.*, 32(9), pp. 1924–1929, 2008.

[284] E. Sevick-Muraca *et al.* Imaging of lymph flow in breast cancer patients after microdose administration of a near-infrared fluorophore: Feasibility study. *Radiology*, 246(3), pp. 734–741, 2008.

[285] J. van der Vorst *et al.* Dose optimization for near-infrared fluorescence sentinel lymph node mapping in patients with melanoma. *Br. J. Dermatol.*, 168(1), pp. 93–98, 2013.

[286] C. Martel, J. Yao, C. Huang, J. Zou, G. Randolph, and L. Wang. Photoacoustic lymphatic imaging with high spatial-temporal resolution. *J. Biomed. Opt.*, 19(11), p. 116009, 2014.

[287] S. Kwon and E. Sevick-Muraca. Noninvasive Quantitative Imaging of Lymph Function in Mice. *Lymphat. Res. Biol.*, 5(4), pp. 219–232, 2007.

[288] M. Tanter and M. Fink. Ultrafast imaging in biomedical ultrasound. *IEEE Trans. Ultrason. Ferroelectr. Freq. Control*, 61(1), pp. 102–119, 2014.

[289] C. Demené *et al.* Ultrafast Doppler reveals the mapping of cerebral vascular resistivity in neonates. *J. Cereb. Blood Flow Metab.*, 34(6), pp. 1009–17, 2014.

[290] J. Yao *et al.* Multiscale photoacoustic tomography using reversibly switchable bacterial phytochrome as a near-infrared photochromic probe. *Nat. Methods*, 13(1), p. 67, 2015.

[291] Y. Li *et al.* Engineering a near-infrared dark chromoprotein optimized for photoacoustic imaging. *SPIE 9708, Photons Plus Ultrasound Imaging Sens. 2016*, p. 97081Z, 2016.

[292] S. Farkona *et al.* Cancer immunotherapy: the beginning of the end of cancer? *BMC Med.*, 14(1), p. 73, 2016.